ALBA

2016

ACTIVITY REPORT

ALBA

2016

ACTIVITY REPORT

Generalitat de Catalunya
Departament d'Empresa
i Coneixement

GOBIERNO DE ESPAÑA
MINISTERIO DE ECONOMÍA, INDUSTRIA Y COMPETITIVIDAD

ALBA Synchrotron
Carrer de la Llum 2-26
08290 Cerdanyola del Vallès (Barcelona)
Spain
Tel. +34 93 592 4300

Editors: Salvador Ferrer and Ana Belén Martínez

We'd like to thank the contributors who participate in this publication:
Lia Addadi, J. Ávila, M. Ávila, C. Bran, M. Broseta, C. Colldelram, L. Croguennec, G. Cuní, T.A. Ezquerra, J. García-Martínez, J. Gazquez, J.B. González, Aitor Hierro, U.Iriso, A. Lopez-Rubio, Alberto Marina, O. Matilla, J.E. Ortega, E. Pereiro, Ana Joaquina Pérez-Berná, F. Pérez, M. Pont, Adriana L. Rojas, M. Rodríguez, A. Ruz, N.L. Saini, J. Salabert, A. Sánchez, J.A. Sans, X. Serra, E. Solana-Madruga, L. Torino, Neta Varsano, N. Valls and A. Verdaguer.

Graphic design: Lucas Wainer

Printing: JM Gràfic

CONTENTS

FOREWORD

Dear reader,

An important milestone has been marked at ALBA during 2016: the beginning of the development beyond the day-one investments. MIRAS, the infrared spectroscopy beamline, started delivering photons to official users in October as the 8th beamline. The facility growth is being pursued starting a beamline project per year. Details of the beamlines in construction at the end of the year are part of this report, namely LOREA, dedicated to low-energy ultra-high resolution angular photoemission for complex materials, and XAIRA, a microfocus beamline for macromolecular crystallography.

The facility operation is mature, with high reliability of all its system, as you can find out in the final pages of the report. More than 1300 user visits were recorded during the year; the number of publications and their high scientific quality (~20 % with an impact factor larger than 7), witness the instrumentation cutting-edge capacities. Industrial users keep summing-up to our community, attracted also by the intense outreach industrial program.

We highlight few of the many scientific results on Biosciences, Catalysis, Magnetism, Material Science and Energy Related materials, ranging from drug development and cell imaging to the most advanced magnetic material characterization.

This year we have moved towards a major advance in the inclusion of other institutions in our daily activity. Towards the end of the year the Iranian Light Source, ILSF, has become our first Associated Partner, at the level of 1% in terms of photon usage and funding, starting from 2017. ILSF is the 4th generation light source project to be built in Qazvin, 140 km North-West from Teheran, presently in the design stage. The Iranian user community is young and preparing to take full benefit from the future national synchrotron. A special program of training and access to ALBA beamlines is therefore an important part of the agreement. Mutual benefit for technological developments and industrial qualification is expected from this collaboration.

Intense international collaboration with sister facilities provides the basis for common projects, taking advantage of European funds and beyond. One of

the consequences is the assignment of several conference and workshop organizations, with the opportunity of showing results and capacities of our instruments to a broad specialized public. Let me mention just two of them, MEDSI16 and IBIC16, which took to Barcelona more than 500 people from all over the world on the same week in September.

Safety for workers and visitors is our priority, what materializes in strengthening controls, revising protocols, performing evacuation drills, etc., but especially in continuous training and awareness-raising actions.

We have started during this year the process of defining the 2017-2020 Strategy Plan, which will be completed next year. We will use it to focus on selected scientific priorities, aiming at targeting the national and international communities, design the next future and provide an outlook to what the facility will be in one decade from now. We are in coordination with the European initiative of LEAPS (League of European Accelerator-based Photon Sources), which aims at harmonizing efforts among European facilities for a better service to the academic world and to the industrial environment which reverts to benefits for the civil society.

Wishing you a pleasant reading.

Caterina Biscari
Director

THE ALBA SYNCHROTRON

ALBA is the Spanish 3rd generation synchrotron light source, located in Cerdanyola del Vallès, near Barcelona, and constitutes the largest scientific infrastructure in the country. The facility consists of the accelerator systems providing 3 GeV electron beam and several experimental beamlines, with photon energies currently ranging from infrared up to hard X-rays of tens of KeV. Different synchrotron radiation techniques are available including diffraction, spectroscopies and imaging.

The ALBA project was approved in 2003 and funded in equal parts by the Spanish and Catalan governments. It is managed by CELLS (Consortium for the Construction, Equipping and Exploitation of the Synchrotron Light Source).

ALBA was built on a green field next to the Universitat Autònoma de Barcelona and several research centres in the Bellaterra campus. The construction began in 2006, after few years dedicated to the design and to the training of a new team of experts, coming from Spain and abroad. The building and the services were ready by 2009, when the accelerator installation started. The whole accelerator was ready and commissioned by 2011, and the seven first beamlines were installed and commissioned in 2011-12. First official users were hosted in 2012, and in 2013 all the Phase I beamlines were operational. In October 2016 the first Phase II beamline, MIRAS, hosted official users for the first time.

The accelerators

The accelerator system consists of a linear accelerator (Linac) - where electrons reach 100 MeV-, a low-emittance, full-energy Booster - where electrons are accelerated to 3GeV-, and the Storage Ring - where electrons are injected in top-up operation mode-. The Booster (250 m of circumference) and the Storage Ring (269 m) are both hosted in the same tunnel. The lattice is optimized for high photon flux density, with a nominal current of 250 mA. There is a large number of straight sections (24) available, despite the relatively short circumference, thanks to the very compact lattice design, which incorporates quadrupolar field component in the dipoles.

The vacuum chamber has up to 34 windows for the light extraction. Thirteen of them are presently used (2 for accelerator diagnostics, 8 for operational beamlines and 3 for beamlines under construction), and the others witness the large potentiality of ALBA for the future.

The beamlines

ALBA has currently eight beamlines dedicated to different scientific fields, mainly physics, chemistry, life sciences, materials science, cultural heritage, biology, nanotechnology. Three beamlines are under construction, expected to be ready for users by 2020.

Below, the list of beamlines describing the number of endstations, the experimental techniques and their scientific applications.

PORT	BEAMLINE	ENDSTATIONS	EXPERIMENTAL TECHNIQUES	SCIENTIFIC APPLICATIONS
1	MIRAS	1	Infrared microspectroscopy	Life sciences, Food sciences, Materials science
4	MSPD	2	High resolution powder diffraction Microdiffraction including high pressure	Structure of materials Time resolved diffraction Quantitative phase analysis
9	MISTRAL	1	Soft X-ray full field transmission X-ray microscope. Optimized on the 'water window'	Cryogenic tomography of biological objects Spatially resolved spectroscopy
11	NCD	1	High resolution small and high angle X-ray scattering/diffraction	Structure and phase transformations of biological fibres, polymers, solutions Time resolved X-ray studies
13	XALOC	1	X-ray diffraction from crystals of biological macromolecules	Macromolecular crystallography, with particular emphasis on large unit cell crystals
22	CLÆSS	1	EXAFS, XANES, Quick-EXAFS, XES	Material Science, chemistry, time resolved studies
24	CIRCE	2	Photoemission microscopy (PEEM) Near atmospheric pressure photo-emission (NAPP)	Nano-science and magnetic domain imaging (PEEM) Surface chemistry (NAPP)
29	BOREAS	2	Circular Magnetic Dichroism Resonant Magnetic Diffraction	Magnetism, surface magnetism and magnetic structures
20	LOREA	1	Angle-resolved photoemission spectroscopy	Polarized electron spectroscopies, band structure determination
6	XAIRA	1	Microfocus beamline for macromolecular crystallography	Macromolecular crystallography, with particular emphasis on small crystals
16	NOTOS	2	X-ray absorption, powder diffraction and metrology	Materials science Chemistry Instrumentation

Grey background corresponds to beamlines in construction.

2016 GOVERNING BODIES

The Rector Council of the ALBA Synchrotron is the main decision-making body and usually meets twice a year. Its responsibilities are to ensure and supervise the performance of the ALBA Synchrotron. The Rector Council delegates powers on the Executive Commission for managing the human and financial resources of the facility.

RECTOR COUNCIL	
Chairperson	**CARMEN VELA OLMO** Secretaria de Estado de Investigación, Desarrollo e Innovación. MINECO
Vice Chairperson	**JORDI BAIGET I CANTONS** Conseller d'Empresa i Coneixement. Generalitat de Catalunya
Members	**JUAN MARÍA VÁZQUEZ ROJAS** Secretario General de Ciencia e Innovación. MINECO **JOSÉ IGNACIO DONCEL MORALES** Subdirector General de Grandes Instalaciones Científico-Técnicas. MINECO **ARCADI NAVARRO I CUARTIELLAS** Secretari d'Universitats i Recerca. Generalitat de Catalunya **FRANCESC RAMON SUBIRADA CURCÓ** Director General de Recerca. Generalitat de Catalunya **MARGARITA ARBOIX ARZO** Rectora de la Universitat Autònoma de Barcelona (UAB)
Secretary	**MARTA JÁUREGUI GÓMEZ** Abogada del Estado
Vice Secretary	**XAVIER URIÓS I APARISI** Advocat de la Generalitat de Catalunya

EXECUTIVE COMMISSION	
Chairperson	**ARCADI NAVARRO I CUARTIELLAS** Secretari d'Universitats i Recerca. Generalitat de Catalunya
Members	**JOSÉ IGNACIO DONCEL MORALES** Subdirector General de Grandes Instalaciones Científico-Técnicas. MINECO **FRANCESC RAMON SUBIRADA CURCÓ** Director General de Recerca. Generalitat de Catalunya
Secretary	**MARTA JÁUREGUI GÓMEZ** Abogada del Estado
Vice Secretary	**XAVIER URIÓS I APARISI** Advocat de la Generalitat de Catalunya

2016 SCIENTIFIC ADVISORY COMMITTEE

The ALBA Scientific Advisory Committee (SAC) is a board of internationally renowned experts in the field of synchrotron radiation, which participates in the strategic scientific management of the ALBA Synchrotron with the aim of ensuring the quality and relevance of the research developed in ALBA. The 22nd meeting of the SAC was held the 6th of June 2016. The 23rd meeting of the SAC was held the 17th and 18th of November 2016. These were its members in the last meeting:

IAN ROBINSON, CHAIR

Full professor at the London Centre for Nanotechnology

WIM BRAS

Project leader of DUBBLE CRG-BL at the European Synchrotron Radiation Facility (ESRF)

ANDREAS JANKOWIAK

Director of the Institute Accelerator Physics at the Helmholtz Zentrum Berlin

VALERIE BRIOIS

ROCK beamline responsible at Soleil Synchrotron

MARTÍN MARTÍNEZ RIPOLL

Research Professor at the Institute of Physical-Chemistry "Rocasolano", Department of Crystallography

AMOR NADJI

Director of Sources and Accelerators Division at Soleil Synchrotron

ENRIQUE ORTEGA

Full professor at the Universidad del País Vasco, Department of Applied Physics I

MARCO STAMPANONI

Paul Scherrer Institut & Swiss Federal Institute of Technology Zürich

OLIVER SEECK

Group leader of the "PETRA III experiments" group at DESY in Hamburg

TRINITAT PRADELL

Full professor at the Universitat Politècnica de Catalunya, Department of Physics and Nuclear Engineering

NEW BEAMLINES IN CONSTRUCTION

Once BL01-MIRAS, devoted to infrared microspectroscopy (and the first phase 2 beamline), has successfully entered user operation, which is reported in a dedicated section of this document, the two beamlines which continue their design and construction process at ALBA are BL20-LOREA and BL06-XAIRA.

LOREA is the second (and last) phase 2 beamline. Devoted to angle-resolved photoemission spectroscopy (ARPES) LOREA will add to the ALBA portfolio an essential tool to deal with the electronic structure of advanced materials such as topological insulators, graphene-based systems, high Tc superconductors, among others. The capabilities offered by this beamline are strongly synergic to some phase 1 beamlines, such as BL24-CIRCE and BL29-Boreas.

During 2016 the LOREA project has advanced substantially. The photon source, an Apple type permanent magnet undulator and the front end providing the interface between beamline and storage ring, had their corresponding contracts placed and manufacturing started during the year. The target is to have them installed in the tunnel in the second half of 2017. The optical design was completed and approved, giving rise to the first call for tenders and to the initiation of an in-house development for the monochromator, to be continued during 2017. Also the end station went through a design effort, leading to a complete conceptual setup, elaborated internally and then critically revised by an international panel of external experts and key users. The station is configured around a central transfer chamber, surrounded by a number of satellite facilities which provide different means of preparing or characterizing a variety of sample types. The chamber where the sample is illuminated with photons coming from the ALBA storage ring is one of such satellites. The design was approved at the very end of the year and will allow proceeding with the contracting phase during 2017. The final milestone of the project is to have official users at LOREA after summer 2019.

At the very beginning of 2016 the approval of the first ALBA phase 3 beamline was announced. Phase 3 was conceived as an ambitious program of extension of ALBA capabilities which should channel the strategic investments during the period 2015-20. A total of 6 new beamlines were defined and selected as the result of a collaborative process involving ALBA and the user community and analyzed and critically revised by the ALBA SAC. BL06-XAIRA will be a beamline devoted to macromolecular crystallography with a photon beam size close to 1 µm at the sample position. This will allow to target very small crystals, necessary to deal with molecules difficult to crystalize, such as membrane proteins. In addition it will open up the possibility of implementing novel techniques which limit radiation damage on samples, such as helical scans. Altogether XAIRA will be an excellent complement to the very successful existing beamline at ALBA, BL13-XALOC, with emphasis on the most challenging experiments. The design and construction project started during 2016 with the appointment of a project manager, Dr. Jordi Juanhuix, and the elaboration of the so-called project initiation document (PID), which includes a detailed description of the main beamline elements, conveniently grouped in suitable work packages, a cost study and a global project schedule proposal. The complete PID was submitted for approval by the very end of the year and approved shortly after. The next steps are the elaboration of detailed designs for optics and end station, plus the launching of call for tenders for the photon source (insertion device) and beamline-accelerator interface (front end). The schedule elaborated as part of the PID aims at having the first official users at XAIRA during late 2020.

Looking back, once the onset of phase 3 has caught up with the delayed phase 2, an exciting period lies ahead of ALBA, with the 8th beamline already in operation and two more beamlines in construction, started with a difference of one year. It is to be expected that additional phase 3 beamlines will be approved, hopefully at a rate of one per year, so that the excellent capabilities of the ALBA accelerator complex are fruitfully converted into exciting scientific results for a wider user community than today.

GOBIERNO DE ESPAÑA MINISTERIO DE ECONOMÍA, INDUSTRIA Y COMPETITIVIDAD
UNIÓN EUROPEA Fondo Europeo de Desarrollo Regional "Una manera de hacer Europa"
BL06-XAIRA is co-funded by the European Regional Development Fund (ERDF) within the Framework of the Smart Growth Operative Programme 2014-2020.

BIOSCIENCES

Structural insights into dUTPase signalling mechanisms

Another look at the mechanism involving trimeric dUTPases in Staphylococcus aureus pathogenicity island induction involves novel players in the party. *Nucleic Acids Research* 44 (11):5457-5469 (2016) doi: 10.1093/nar/gkw317

Elisa Maiques[1], Nuria Quiles-Puchalt[2,3], Jorge Donderis[1], J Rafael Ciges[1], Christian Alite[1], Janine Z. Bowring[3], Suzanne Humphrey[3], José R Penadés[3*], Alberto Marina[1*]

The dUTPase (Dut) enzymes, encoded by almost all free-living organisms and some viruses, catalyses the hydrolysis of deoxyuridine triphosphate (dUTP) to deoxyuridine monophosphate (dUMP) and pyrophosphate. Most cellular DNA polymerases cannot distinguish between dUTP and dTTP, thus Duts are assumed to be essential enzymes for DNA integrity and viability by reducing the dUTP pool, preventing incorporation of dUTP into the chromosome. However, several different works have questioned this general assumption, since DNA uracilation can be beneficial in some cases. In fact, the previous work demonstrated that trimeric Duts from *Staphylococcus aureus* phages act as de-repressor proteins for a subset of Staphylococcal pathogenicity islands (SaPIs). Working with the Dut from *S. aureus* phage 80α, it has been showed that this moonlighting activity is mediated by the interaction of Dut with the SaPI-encoded repressor Stl. To perform this regulatory process, the Duts require the participation of the strongly conserved Dut P-loop (motif V) as well as a characteristic extra motif VI only present in the staphylococcal phage coded Duts. By similarity, it was proposed that Duts are signalling molecules that act analogously to eukaryotic G-proteins, using dUTP as a second messenger. Recently, however, analysing the Dut from *S. aureus* phage ϕ11 an alternative model involving Duts in the transfer of the SaPIs was proposed, questioning the implication of motifs V and VI and the signalling capacity of Duts.

This striking discrepancy in the mechanism of SaPI mobilization by two extremely similar Duts took authors attention. Was it possible that these two Duts used different mechanisms to interact with the same Stl or was the proposed signalling model wrong? To answer this question advantage has been taken of the power of X-ray crystallography and other biophysical techniques such as biolayer interferometry (BLI), as well as *in vivo* biological assays, and it has been revisited the previous data in order to generate a model that could reconcile all the *in vitro* and *in vivo* observations.

Authors designed and analysed a battery of Dut 80α and ϕ11mutants on the motifs predicted by the model to be involved in the interaction with Stl. The capacity to these mutants for mobilize SaPIs was evaluated *in vivo* and the affinity for Stl was measured *in vitro* by BLI. In parallel, it was evaluated the role of the substrate dUTP, and the product dUMP, in the Dut-Stl interaction. Finally, authors solved the three-dimensional structure of Dut from phage 80α in complex with the product dUMP and the structure of a mutant in the motif V of this Dut in complex with the substrate dUTP. X-diffraction data used to solve these structures were collected at XALOC beamline of the ALBA Synchrotron and ID23_1 beamline of the European Synchrotron Radiation Facility. Both crystals were isomorphous and belonged to space group $P2_13$. The structures were solved by molecular replacement using as a model the wilt-type structure of Dut 80α previously

solved by the group. The final models were refined at 2.3 Å and 2.4 Å resolution for the complex with dUMP and the mutant, respectively. These structures allowed the authors to see for first time the conformation of the motif V covering the active site in the presence of the product dUMP, and the structural effect on this motif of a mutation that dismissed the interaction with Stl. These structures showed that the motif V adopt alternative conformations in the presence of the substrate and the product (Fig. 1), and that, surprisingly, the mutant presents a motif V with identical conformation to that observed in the wild-type protein.

Altogether, the structural, *in vitro* and *in vivo* analyses of wild-type and mutants of Duts from 80α and ϕ11 phages confirmed the previously proposed implication of motifs V and VI in Stl recognition and binding, but revealed differences among Duts in the contribution of each motif in this process. In addition, this parallel analysis revealed that new catalytic conserved motif in Duts (motif IV) is also involved in Stl binding. The X-ray structures showed that this new uncovered interacting region maps in close vicinity of motifs V and VI, the previous regions involved in Stl recognition. Indeed, the residues from motif IV revealed in this analysis map in close vicinity of the region of motif V that experiences major changes depending on whether it is the dUMP or the dUTP that is bound to the enzyme.

These results confirm the signalling capacity of the Duts and allowed the authors to propose a revised model (Fig. 2) for Dut-Stl interaction where the Stl recognizes *apo* Duts by interacting with residues from motifs IV and VI in the vicinity of the active center. Once Stl is bound, the highly flexible motif V would interact with Stl, stabilising the complex. On the contrary, the dUTP binding to the *apo* Dut will induce the folding and stabilization of motif V over the active center, hampering the access of Stl to the anchor area and preventing the binding.

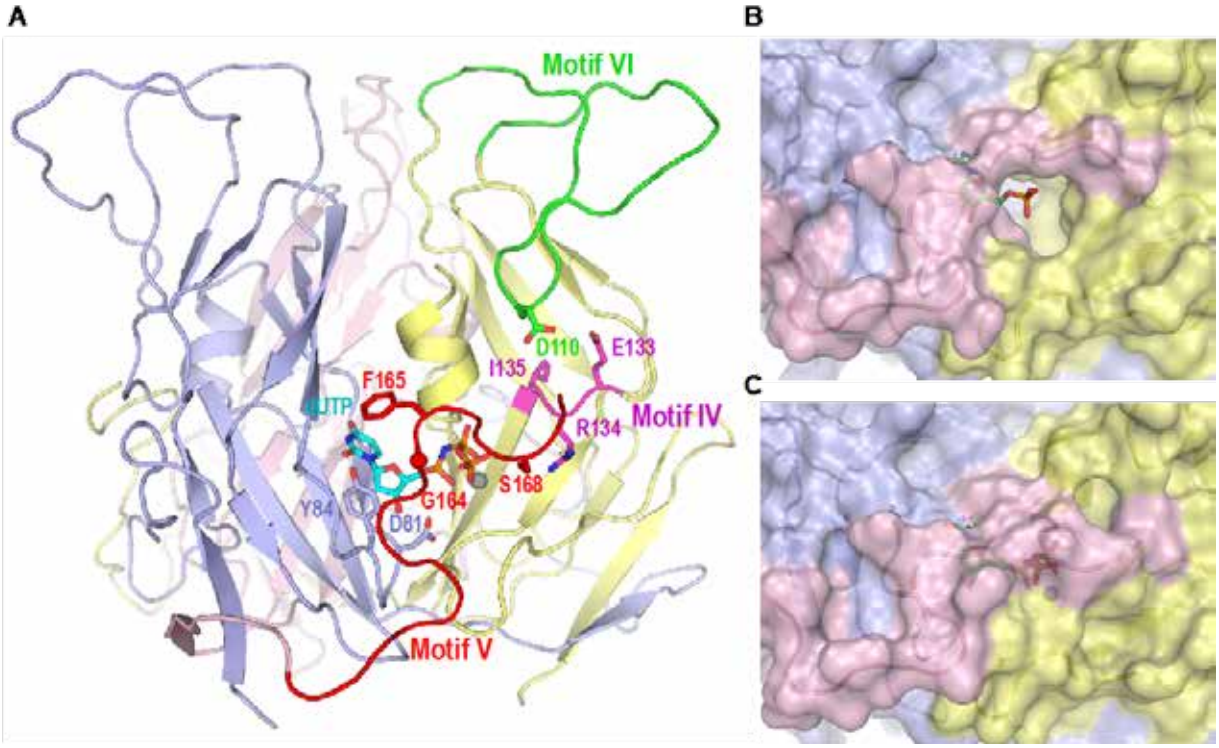

Figure 1: (A) Structure of homotrimeric (monomers in blue, yellow, and pink) Dut from phage 80α bound to dUTP-Mg (in sticks with carbon atoms in cyan and gray sphere, respectively; PDB 3ZEZ) highlighting in one monomer the phage Dut specific motif VI (green) and the the Dut conserved motifs IV (magenta) and V (red). Residues in which mutations were analyzed in the study are shown in sticks and labelled. (A) Close view of the active center of Dut 80α bound to (B) dUMP and (C) dUTP (PDB 3ZEZ) showed that the produc dUMP opens the active center. The structures are rendered in semi-transparent surface to show the bound nucleotide (in sticks with carbon atoms colored in green). Each subunit is shown in cartoon and colored in yellow, blue and pink respectively. Motif V corresponds to the subunit colored in pink. In the dUMP bound structure (B) the αP is solvent exposed by a channel that could be used to release the product pyrophosphate, while in the dUTP bound structure (C) the nucleotide is completely sealed by the motif V (pink).

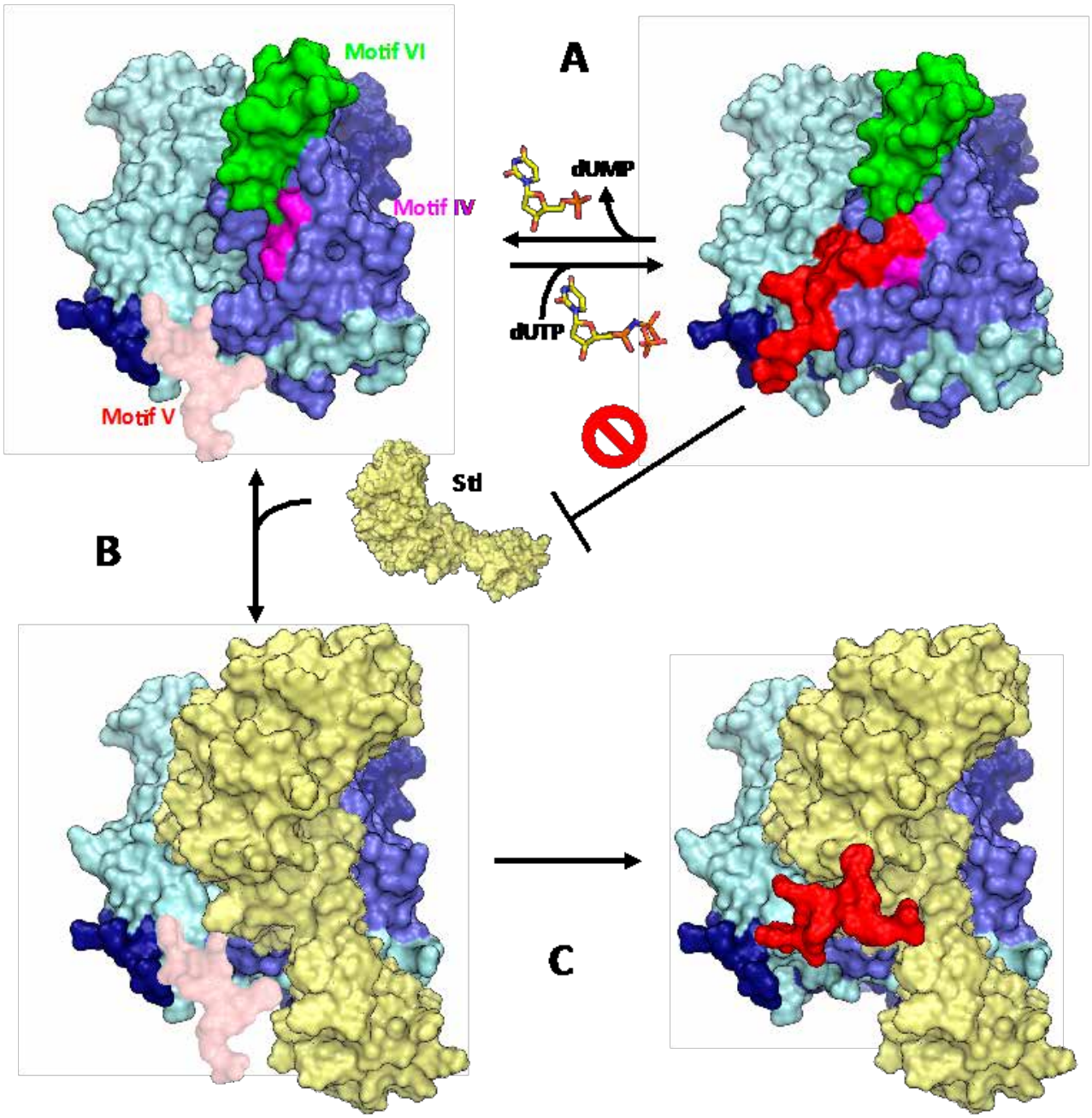

Figure 2: Model of S. *aureus* phage Dut interaction with SaPIs Stl. (A) Binding and hydrolysis of dUTP by Dut implicates the folding and stabilization of the high flexible conserved motif V (pink-red) over the active center. This disposition of motif V limited the access of Stl to their anchor place formed by motif IV (magenta) and motif VI (green) preventing the binding. (B) Contrary, in the Dut *apo* form, Stl anchor region is accessible due to the motif V flexibility, allowing Stl to interact with residues from motifs IV and VI in the vicinity of the active center. (C) Once Stl is bound, motif V would interact with Stl, stabilising the complex.

ACKNOWLEDGEMENTS

This study involves the use of X-ray crystallography at two synchrotron facilities, ALBA Synchrotron in Barcelona and ESRF in Grenoble, and is the result of an interdisciplinary collaboration between the Institute of Biomedicine of Valencia (IBV-CSIC), CIBERER and the Institute of Infection, Immunity and Inflammation from University of Glasgow.

AFFILIATION:

1.Instituto de Biomedicina de Valencia (IBV-CSIC) and CIBER de Enfermedades Raras (CIBERER), 46010 Valencia, Spain

2.Departamento de Ciencias Biomédicas, Facultad de Ciencias de la Salud, Universidad CEU Cardenal Herrera, 46113 Moncada, Valencia, Spain

3.Institute of Infection, Immunity and Inflammation, College of Medical, Veterinary and Life Sciences, University of Glasgow, Glasgow G12 8TA, UK

A multi-component recognition mechanism for protein recycling

Structural Mechanism for Cargo Recognition by the Retromer Complex.
***Cell* 167**(6):1623-1635 (2016) doi:10.1016/j.cell.2016.10.056

María Lucas[1], David C. Gershlick[2], Ander Vidaurrazaga[1], Adriana L. Rojas[1], Juan S. Bonifacino[2] and Aitor Hierro[1,3*]

Packaging labels and recycling symbols help us to identify how different items can be recycled by placing them into distinct recycling bins and carrier collection points. Like glass, paper, plastic and aluminium, many cellular proteins are recycled and reused inside our cells for the same reasons, to reduce the consumption of resources, save energy and minimize waste. In this sense, protein recycling has a direct impact on metabolic balance and cellular homeostasis. Retromer is a multi-protein complex responsible for recycling protein channels and receptors involved in a wide range of physiological processes such as nutrient intake, cell signalling, polarized transport, cell differentiation, immune response and nerve transmission. The physiological relevance of retromer and its involvement in neurodegenerative processes such as Alzheimer and Parkinson's disease has grown exponentially since its discovery over 15 years ago. However, the mechanism for selecting which proteins are to be recycled and their inclusion in vesicles for transportation has remained elusive [1].

Retromer is a complex composed of a highly conserved core of the Vacuolar Protein Sorting (VPS) proteins VPS26, VPS29 and VPS35, and a membrane-targeting subcomplex of mono or hetero dimeric sorting nexins (SNXs) that binds to phosphoinositide lipids. To understand how cargo is recognized by retromer authors have used a combination of X-ray crystallography, small-angle X-ray scattering (SAXS), biochemistry and cellular analyses.

Initial experiments focused on the N-terminal portion of VPS35 (VPS35N). The structure of VPS35N (residues 14-470) was solved by single-wavelength anomalous diffraction (SAD) using selenomethionine-derived crystals and refined at 3.0 Å resolution. Subsequent experiments focused on the VPS26-VPS35N subcomplex bound to SNX3 and a canonical recycling signal from the divalent metal transporter 1 isoform II (DMT1-II). The crystal structure of the four-subunit complex was solved by molecular replacement using the crystal structures of the previously solved VPS35N fragment, and the subunits VPS26A (PDB: 2FAU) and SNX3 (PDB: 2YPS) as search models.

The complex has a T-shape architecture, with VPS26 and VPS35N corresponding to both sides of the horizontal bar and SNX3 to the vertical bar (Fig. 3A). The PtdIns3P-binding pocket on SNX3 occurs on the opposite side of the VPS26-VPS35-interaction surface, consistent with the role of SNX3 in retromer recruitment to endosomal membranes. The crystal structure shows how recognition of canonical recycling signals involves an extensive network of hydrogen bonds and hydrophobic interactions engaging both SNX3 and VPS26 (Fig. 3B). In addition, the current structure of VPS26-VPS35N bound to SNX3 together with a previously solved structure of VPS29-VPS35C [2] suggests a general mechanism for assembly of retromer coats on membrane tubules [3].

Isothermal titration calorimetry experiments confirmed that DMT1-II recognition involves binding to both retromer and SNX3. The DMT1-II recycling signal did not exhibit any detectable binding to isolated retromer or SNX3 but bound retromer in the presence of SNX3. The shared and cooperative nature of these interactions explains why previous attempts to characterize interactions of recycling signals with single subunits or partial complexes had limited success.

To evaluate the functional relevance of the VPS26-VPS35N-SNX3 structure, a SNX3 CRISPR knock-out (KO) HeLa cell line was generated. These cells exhibited decreased association of retromer with membranes relative to control HeLa cells. This phenotype could be rescued by stable expression of GFP-SNX3 but not a GFP-SNX3ΔN construct lacking the SNX3 N-terminal tail. These findings demonstrate that the interaction of the N-terminal of SNX3 with VPS26 and VPS35 is required for recruitment of retromer to membranes. Then, to test if the SNX3-mediated recruitment of retromer to the membrane is essential for cargo sorting, we evaluated the localization of DMT1-II in the absence or presence of SNX3. As expected, DMT1-II displayed increased colocalization with the early endosomal marker EEA1 in SNX3-KO cells relative to control HeLa cells. This phenotype could also be corrected by stable expression of GFP-SNX3 but not GFP-SNX3ΔN, demonstrating that the interaction of SNX3 with VPS26 and VPS35 is required for sorting of DMT1-II out of early endosomes. Together, these results show how the recruitment of retromer by SNX3 to PtdIns3P-enriched endosomes is concomitant with cargo selection.

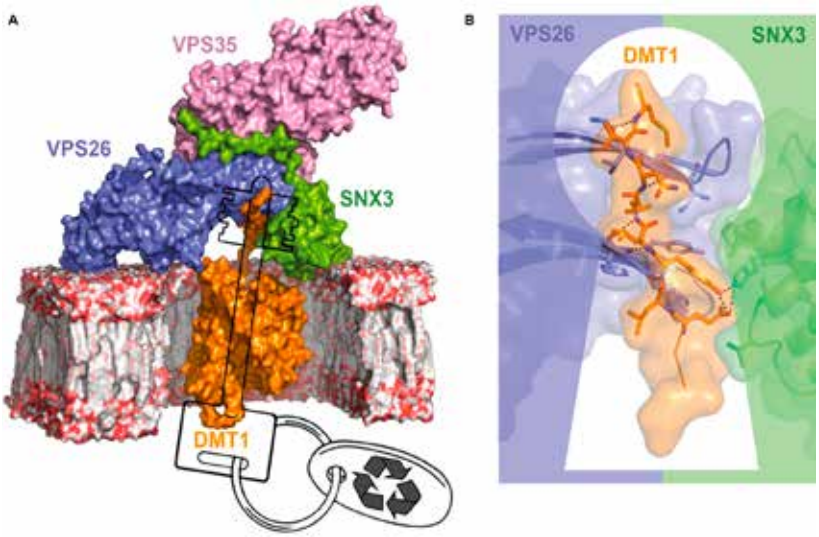

Figure 3: (A) Model of the retromer-SNX3 assembly for the recognition of the Φ-x-L/M recycling signal from the divalent cation transporter DMT1-II. (B) Close-up view showing the contribution of VPS26 and SNX3 subunits for the recognition of the recycling signal. The analogy is that of a lock-and-key mechanism where the lock is composed of two subunits to recognize the recycling signal (key).

In summary, this study describes the recognition mechanism for recycling and reusing the divalent metal transporter protein (DMT1) involved in cellular absorption of iron, an essential element for life. The mechanism can be compared to that of a key being inserted in a lock. In this case, the key would be the recycling signal and the keyhole would be made up of the combination of two proteins, retromer and SNX3 (Fig. 3). The interesting aspect of this discovery is the possible existence of a combination code between retromer and other SNX proteins, thereby generating different keyholes for the process of selecting proteins for recycling. The challenge resides now in the structural analysis of other SNXs-retromer combinations with different cargos.

OTHER REFERENCES

[1] Hierro A, Gershlick DC, Rojas AL, Bonifacino JS. Formation of Tubulovesicular Carriers from Endosomes and Their Fusion to the trans-Golgi Network. *Int Rev Cell Mol Biol.* **318**:159-202 (2015).

[2] Hierro A, Rojas AL, Rojas R, Murthy N, Effantin G, Kajava AV, Steven AC, Bonifacino JS, Hurley JH. Functional architecture of the retromer cargo-recognition complex. *Nature.* **25**;449(7165):1063-7(2007).

[3] Lucas M, Gershlick DC, Vidaurrazaga A, Rojas AL, Bonifacino JS, Hierro A. Structural Mechanism for Cargo Recognition by the Retromer Complex. *Cell.* 2016 Dec 1;**167(6)**:1623-1635.e14.

ACKNOWLEDGEMENTS

This work was supported by the Carlos III Health Institute grant PI11/00121, the Basque Government grant PI2011-26 and the Spanish Ministry of Economy and Competitiveness grant BFU2014-59759-R.

AFFILIATION:

1. Structural Biology Unit, CIC bioGUNE, Bizkaia Technology Park, 48160 Derio, Spain
2. Cell Biology and Neurobiology Branch, Eunice Kennedy Shriver National Institute of Child Health and Human Development, National Institutes of Health, Bethesda, MD 20892, USA
3. IKERBASQUE, Basque Foundation for Science, 48011 Bilbao, Spain

Soft X-Ray Cryo-Tomography reveals ultrastructural alterations of the host cell during Hepatitis C infection

Structural Changes in Cells Imaged by Soft X-ray Cryo-Tomography During Hepatitis C Virus Infection. *ACS Nano* 10(7): 6597-6611 (2016) doi: 10.1021/acsnano.6b01374

Ana Joaquina Pérez-Berná[1*], Maria José Rodríguez[2], Francisco Javier Chichón[2], Martina Friederike Friesland[3], Andrea Sorrentino[1], Jose L. Carrascosa[2], Eva Pereiro[1] and Pablo Gastaminza[2]

Chronic hepatitis C virus (HCV) infection causes severe liver disease in millions of humans worldwide. Cryo soft X-ray tomography (cryo-SXT) was performed to investigate the ultrastructural alterations induced by the interference of HCV replication with cellular homeostasis. Native, whole cell, three-dimensional (3D) maps were obtained in HCV replicon-harboring cells and in a surrogate model of HCV infection. Tomograms from HCV-replicating cells show blind-ended endoplasmic reticulum tubules with pseudospherical extrusions and marked alterations of mitochondrial morphology that correlated spatially with the presence of endoplasmic reticulum alterations, suggesting a short-range influence of the viral machinery on mitochondrial homeostasis. Both mitochondrial and endoplasmic reticulum alterations could be reverted by a combination of sofosbuvir/daclatasvir, which are clinically approved direct-acting antivirals for the treatment of chronic HCV infection. In addition to providing structural insight into cellular aspects of HCV pathogenesis, the study illustrates how cryo-SXT is a powerful 3D wide-field imaging tool for the assessment and understanding of complex cellular processes in a setting of near-native whole hydrated cells. The results also constitute a proof of concept for the use of cryo-SXT as a platform that enables determining the potential impact of candidate compounds on the ultrastructure of the cell that may assist drug development at a preclinical level.

One of the current goals in biology is to obtain the complete 3D structure of the whole cell in its native state, and soft X-ray cryo tomography (cryo-SXT) is the only imaging modality that allows elaborating 3D maps of vitrified whole-cell samples at nanometer-resolution, thus avoiding chemical treatment or sectioning. Cryo-SXT is based on the natural contrast of frozen-hydrated, unstained cells in the water window energy range (between the K absorption edges of C and O) with an achievable half pitch resolution down to 50 nm. In this study, native, wide-field, 3D maps of cells harboring HCV replicons have been generated using cryo-SXT at the MISTRAL beamline (ALBA Synchrotron). Authors were able to identify the salient alterations induced by HCV replication as well as the sequence of events occurring in a surrogate model of HCV infection. In these experiments, the profound alteration of the whole endoplasmic reticulum network in 3D is entirely observed in vitrified samples (Fig. 4). Moreover, authors have observed a gradual alteration of the mitochondrial structure to the point where no recognizable mitochondria are observed in areas of profound virus-induced endoplasmic reticulum alteration. Remarkably, localization of abnormal mitochondria is spatially correlated with the appearance of a modified endoplasmic reticulum network, reinforcing the notion that a local alteration of the endoplasmic reticulum may directly alter mitochondrial homeostasis by interorganelle communication through mitochondria-associated endoplasmic reticulum membranes (Fig. 5). These findings provide structural evidence for a local, direct impact of an altered endoplasmic reticulum network on neighboring

mitochondria during HCV infection, a notion that is supported by previous functional data. Finally, authors have studied the regression of the pathological membranous web proliferation caused by HCV replication in culture by the use of clinically relevant direct-acting antivirals such as telaprevir, daclatasvir, or sofosbuvir using cryo-SXT, demonstrating that the observed alterations are indeed induced by HCV replication (Fig. 6).

Native, whole cell, 3D maps were obtained in HCV replicon-harboring human hepatoma cells and in a surrogate model of HCV infection using cryo-SXT.

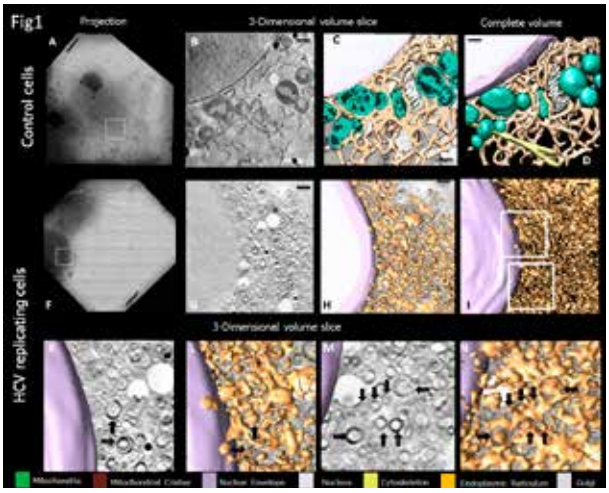

Figure 4: Three-dimensional reconstruction of whole-cell volumes of HCV replicon-bearing cell lines by cryo-SXT. Control (A–D) and HCV replicon-bearing cell lines (F–N) were vitrified and subjected to cryo-SXT. Tile-scanned projections showing the area selected for SXT (square; panels A, F) as well as volume slices of the tomograms from the boxed areas (B, G, K, M) are shown. Color-coded manual segmentation of the surface boundaries identifying different organelles is presented in control (C,D) and HCV-replicating cells (threshold-based isosurface segmentation) (H,I, L,N). Scale bars: 0.5 µm, except panels A and E (10 µm).

These data complement previous high-resolution tomograms obtained by electron microscopy, providing a cellular context in which these alterations occur. The data provide evidence for a structural and topological basis for HCV-induced mitochondrial dysfunction and infected-cell survival, which may be key in HCV pathogenesis. Overall, the data not only provide a model that contributes to understanding HCV-host cell interactions from a structural point of view but also show that cryo-SXT is a powerful imaging tool for the assessment of complex cellular processes in whole hydrated cells that could be exploited for the study of other pathologies.

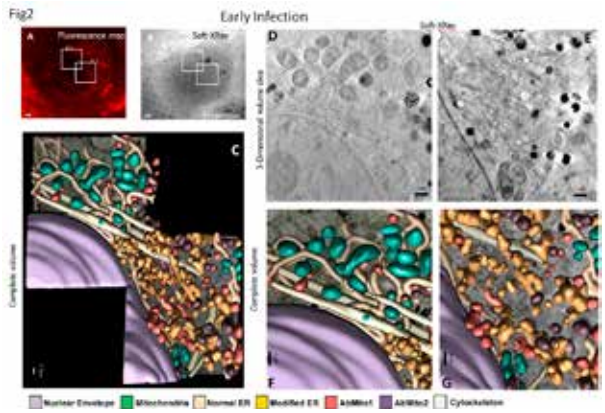

Figure 5: Modifications of the HCVtcp-infected cell cytoplasm at different stages of HCV-infection. Areas of interest in a cell at early stages of the infection displaying partial nuclearization of the fluorescent infection reporter (A). Volume slices (D,E) and manually segmented surface representation of the selected areas (F,G) are shown. (C) Two merged tomograms of adjacent areas (squares in A). Scale bars 5 µm (A, B); 2 µm (C); and 1 µm (D-G).

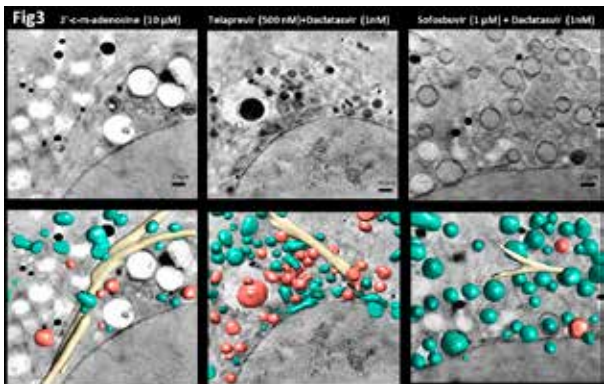

Figure 6: Reversion of HCV-induced ultrastructural alterations by antiviral treatment with direct-acting antiviral assessed by cryo-SXT. HCV replicon-bearing cell lines were treated with the indicated antiviral compounds for 7 days, vitrified, and subjected to cryo-SXT. Volume slices and color-coded manually segmented surface representations are shown. Yellow are used to mark cytoskeleton, in green the normal mitochondria and red the abnormal mitochondria.

ACKNOWLEDGEMENTS

This work was supported by the ALBA Synchrotron standard proposals 2013110712, 2014070974, 2014060907 and 2015091484.

AFFILIATION:

1. ALBA Synchrotron, MISTRAL Beamline, Cerdanyola del Vallès (Barcelona), Spain
2. Centro Nacional de Biotecnología-Consejo Superior de Investigaciones Científicas (CNB-CSIC), Madrid, Spain

A Study of Cholesterol Crystal Early Formation in Cells with cryo-SXT and STORM

Development of Correlative Cryo-soft X-ray Tomography and Stochastic Reconstruction Microscopy. A Study of Cholesterol Crystal Early Formation in Cells. *Journal of the American Chemical Society* 138:14931-14940 (2016) doi: 10.1021/jacs.6b07584

Neta Varsano[1], Tali Dadosh[2], Sergey Kapishnikov[4], Eva Pereiro[5], Eyal Shimoni[1], Xueting Jin[6], Howard S. Kruth[6], Leslie Leiserowitz[3] and Lia Addadi[1*]

Accumulation of cholesterol in the blood vessel walls is a prominent feature of atherosclerosis [1], a major precursor of many cardiovascular diseases. Precipitation of cholesterol crystals can increase the inflammatory response and cause expansion of the lesion core [2]. What initiates cholesterol crystal formation is, however, still not well-understood [3]. Studies in cell culture showed that when a cell is loaded with cholesterol, small cholesterol particles are formed [4]. In parallel, it was demonstrated *in vitro* that at high cholesterol concentration, 2D ordered cholesterol domains form in lipid thin layers, and these can serve as nucleation sites for the formation of 3D cholesterol crystals [5, 6]. Based on this evidence, it was hypothesized that cholesterol segregation in cell membranes may be an initial step in atherosclerosis development [4, 5]. This study shows that very-small (200nm) cholesterol crystals, presumably nascent crystals nucleated from the cell membrane, can be detected associated with macrophage cells after enrichment with cholesterol. The data were collected using a newly developed correlative method that combines cryo soft X-ray tomography (cryo-SXT) with stochastic optical reconstruction microscopy (STORM). The correlative approach provides unequivocal identification of the 3D cholesterol crystals by STORM, imaging and localization by SXT.

The growth of crystals was examined in RAW264.7 cells, under accumulation of cholesterol carrier particles called low-density lipoproteins (LDL). To image the same sample positions with the two techniques, the cells were grown on gold finder-grids. The cells were cultured, enriched with cholesterol, fixed, and labeled on the grids (Fig. 7, Steps 1 and 2, A and B). The position of individual cells was recorded before imaging with STORM, using a fluorescently labeled antibody (MAB 58B1) specific to cholesterol crystals and ordered arrays (7). STORM imaging was performed in the upper part of each cell over a volume of 18 × 18 × 1 μm3 in x, y, and z, respectively (Step 2C). Following analysis with STORM, the grids were vitrified and imaged using the soft X-ray beam (Steps 3 and 4). Tomograms were taken from the same cells that were analyzed by STORM and were aligned to yield a reconstructed volume of 18 × 18 × 18 μm3 (Step 4).

The xy location and the cell orientation were tracked first using the fiducial markers provided by the finder grid, including the labels, the metal grating, the holes in the holey grid coating, and the cell morphology imaged in both techniques (Step 5A). To reliably overlay the data in z, a script was developed that shifts each of the data sets in steps of 80 nm. After each z shift, the software calculates the percentage of the STORM signal coming from the area in each plane delimited by the cell

plasma membrane, seen at high contrast in cryo-SXT (Step 5B). The coverage area of the super-resolution data is calculated relative to the X-ray cell area. The optimal z position is located where the maximum of the super-resolution signals are located within the cell area and are distributed over most of the area (excluding in the cell nucleus).

Segmentation of the reconstructed X-ray data (Step 5C) allows observation of the cell volume together with the overlaid super resolution 3D localization map. Well defined clusters of STORM signals associated with the plasma membrane of the cell (Step 6A, D1 and D2) correspond to high contrast SXT features. Introducing the relevant perpendicular planes (Step 6B) show objects with a rectangular shape (Step 6C1, C2, E1, E2) with lengths and widths in the range of 200-400 nm. The combination of the information contained in the two sets of data converges to identify these objects as cholesterol crystals.

In conclusion, a correlative technique has been developed by authors using STORM and cryo-SXT, which provides visualization of cholesterol crystals as small as 200 × 200 nm, on the cell plasma membrane and in intracellular locations. Cryo-SXT provides a picture in three dimensions of large cellular volumes,

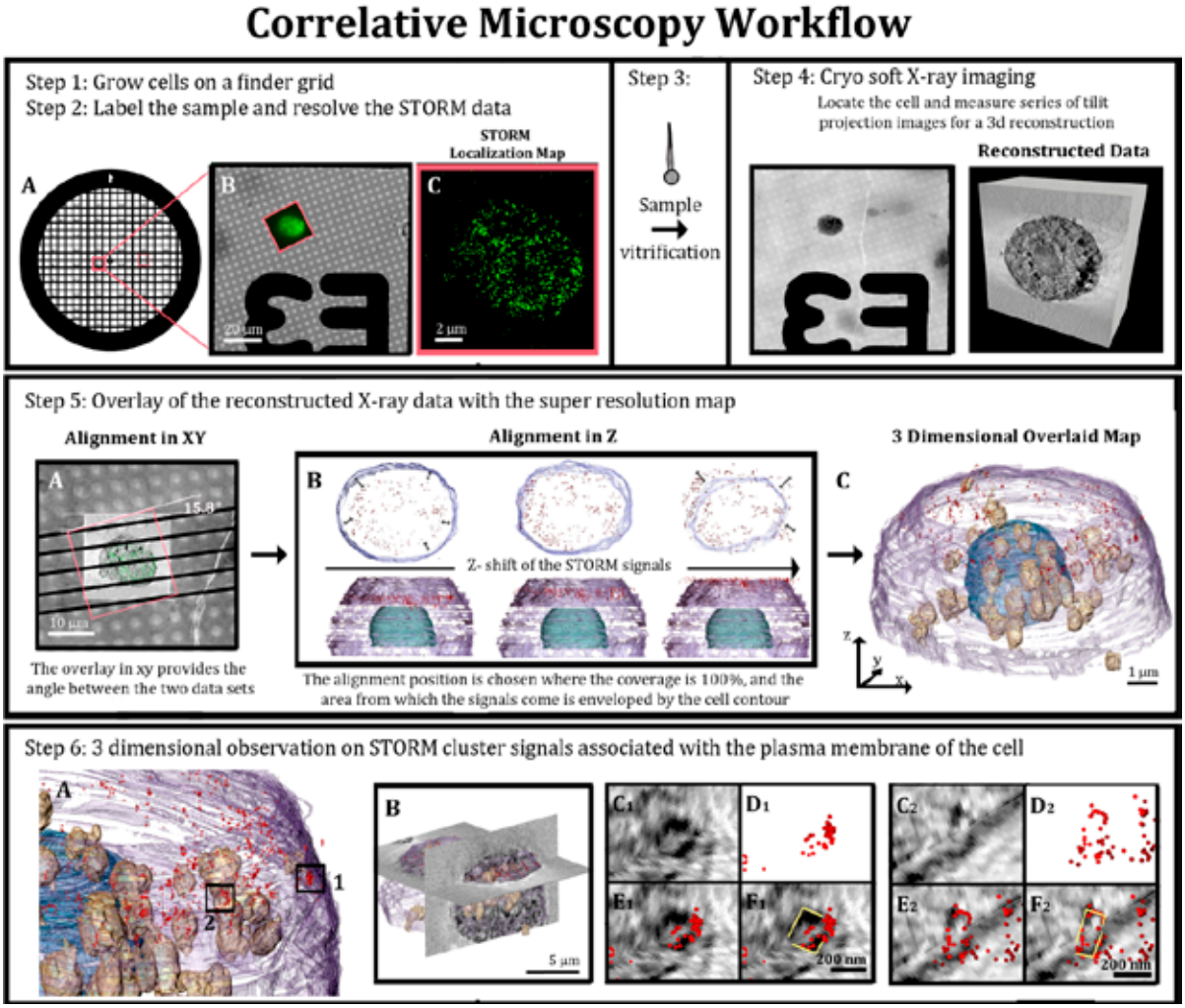

Figure 7: Step1, Cells were grown on gold finder grids with fiducial markers that allow navigation to desired locations on the grid. The cells were incubated for 48 h with acLDL. Step2, Cells were fixed and incubated with primary and secondary antibodies. The super-resolution fluorescence signal was resolved by STORM. Step3, Grids were vitrified. Step4, X-ray tomograms were taken of the same cells that were analyzed by STORM. Data were reconstructed (field of view 18 µm3). Step 5, Overlay of the data in xy and z. Step 6, (A): 3D reconstruction of the same cell from a side view. The localization map of the corresponding resolved super-resolution image (red spots) is 1 µm in thickness and is located on the upper part of the cell, above the nucleus. Black rectangles indicate clusters of STORM signals. (B): Side orientation of the superimposed data combined with a perpendicular slice. (C1-F1) and (C2-F2) show magnifications of the crystals indicated by 1 and 2 in A, viewed in SXT, in STORM and superimposed, respectively.

identifying any aggregation of carbon rich materials on the background of the X-ray transparent cytoplasm rich in water (within the energy range of the water window). The introduction of a specific marker that identifies desired epitopes by STORM enables colocalization between the identified objects and the local environment morphologically characterized by the cryo-SXT, at 70 nm resolution.

It is conceivable that the identified crystals nucleated at the location where they were observed or very close to it. This would support the hypothesis that the crystals may have nucleated from cholesterol domains segregated from lipid mixtures in cell membranes.

To the best of the authors knowledge, this is the first example of a technique providing 3D-imaging and target identification within large volumes of hydrated cellular systems at resolution of tens of nanometers, and in principle can be of use in any other cellular or tissue systems, within the limits of the technical requirements.

ACKNOWLEDGEMENTS

Authors thank Prof. Benjamin Geiger and Michal Shemesh for their support in the cell culture growth and maintenance, and Dr. Sharon G. Wolf for her help in sample preparation. Authors thank Moshe Varsano for his great help with programming. Super-resolution microscopy was performed at the Irving and Cherna Moskowitz Center for Nano and Bio-Nano Imaging at the Weizmann Institute of Science.

Cryo-SXT experiments were performed at MISTRAL beamline at ALBA Synchrotron with the collaboration of ALBA staff. The research leading to these results has received funding from the European Community's Seventh Framework Programme (FP7/2007-2013) under grant agreement no. 283570, and by the Binational Science Foundation (grant 2013045 to L.A. and H.S.K.). L.A. is the incumbent of the Dorothy and Patrick Gorman Professorial Chair of Biological Ultrastructure at the Weizmann Institute of Science.

OTHER REFERENCES

[1] (a) Insull, W., Jr.; Bartsch, G. *J. Clin. Invest.* **45**, 513 (1966). (b) Kruth, H. S. *Curr. Mol. Med.* **1**, 633 (2001). (c) Katz, S.; Shipley, G. G.; Small, D. *J. Clin. Invest.* **58**, 200 (1976).

[2] Small, D. Arterioscler., Thromb., *Vasc. Biol.* **8**, 103 (1988). (b) Abela, G.S.. *J Clin Lipidol.*, **4**, 156 (2010)

[3] Kellner-Weibel, G.; Yancey, P.; Jerome, W.; Walser, T.; Mason, R.; Phillips, M.; Rothblat, G. Arterioscler., Thromb., *Vasc. Biol.* **19**,1891 (1999).

[4] Ong, D. S.; Anzinger, J. J.; Leyva, F. J.; Rubin, N.; Addadi, L.;Kruth, H. S. *J. Lipid Res.* **51**, 2303 (2010).

[5] (a) Solomonov, I., Weygand, M.J., Kjaer, K., Rapaport, H. and Leiserowitz, L., *Biophys. J.* **88**, 1809 (2005); (b) Ziblat, R.; Fargion, I.; Leiserowitz, L.; Addadi, L. *Biophys. J,* **103**, 255 (.2012). (c) Ziblat, R.; Leiserowitz, L.; Addadi, L. *J. Am. Chem. Soc.* **132**, 9920 (2010). (d) Ziblat, R.; Kjaer, K.; Leiserowitz, L.; Addadi, L. *Angew. Chem.*,Int. Ed. **48**, 8958 (2009).

[6] Varsano, N.; Fargion, I.; Wolf, S. G.; Leiserowitz, L.; Addadi, L. *J. Am. Chem. Soc.* **137**, 1601 (2015).

[7] (a) Perl-Treves, D.; Kessler, N.; Izhaky, D.; Addadi, L. *Chem. Biol.* **3**, 567 (1996). (b) Izhaky, D.; Addadi, L. *Adv. Mater.* **10**, 1009 (1998).

AFFILIATION:

1. Department of Structural Biology, 2. Department of Chemical Research Support, and 3. Department of Materials and Interfaces, Weizmann Institute of Science, Rehovot, 76100, Israel

4. Soft Matter and Functional Materials, Helmholtz-Zentrum Berlin, Albert-Einstein-Strasse 15, D-12489 Berlin, Germany

5. ALBA Synchrotron, MISTRAL Beamline–Experiments Division, 08290 Cerdanyola del Valles, Barcelona, Spain

6. Experimental Atherosclerosis Section, National Heart, Lung, and Blood Institute, National Institutes of Health, Bethesda, Maryland 20892-1422, United States

Imaging intracellular calcium accumulation in calcifying marine algae using cryo-X-ray tomography

A vacuole-like compartment concentrates a disordered calcium phase in a key coccolithophorid alga. *Nature Communications* 7: 11228 (2016) doi: 10.1038/ncomms11228

S. Sviben[1,*], A. Gal[1,2,*], M.H. Hood[1,2,*], L. Bertinetti[2], Y. Politi[2], M. Bennet[2], P. Krishnamoorthy[1], A. Schertel[3], R. Wirth[4], A. Sorrentino[5], E. Pereiro[5], D. Faivre[2] & A. Scheffel[1]

Coccolithophores are widespread marine algae that produce biogenic calcite in the form of minute calcitic scales, known as coccoliths. The coccolith is formed intracellularly, inside a membrane-bound compartment, and upon maturation it is extruded to the cell exterior where many coccoliths are covering the cell surface. This biomineralization process draws considerable attention since coccolithophores may play an important role in the response of the oceanic ecosystem to predicted global climate change, and since similar changes in the past were recorded in the chemical composition of coccoliths that accumulated in ocean-floor sediments. Following dynamic cellular processes *in vivo*, such as coccolith synthesis, is extremely challenging. This is because of the experimental difficulties involved in following inorganic small molecules at the spatial and temporal resolution needed to trace intermediate and short-lived phases in the crystallization pathway. Therefore, the intracellular pathways responsible for the transport of the constituent ions from seawater to the growing coccolith are mostly unknown.

The authors used synchrotron soft-X-ray tomography at cryogenic conditions (Mistral beamline, ALBA Synchrotron) in order to map the intracellular calcium in coccolith producing cells of the model coccolithophore species *Emiliania huxleyi.* The cells were rapidly frozen and maintained at cryogenic conditions to preserve their intracellular organization. Single cells were imaged with the X-ray microscope at a resolution of 50 nm. Two types of data sets were acquired. The first is a tilt-series at the 'water window' energy range. At this X-ray energy the best contrast between carbon-rich intracellular membranes and the water-rich cytoplasm is achieved so the data can be used for 3D reconstruction of cells. The second data set was an energy scan around the Ca L-edge. From these data a complete X-ray Absorption Near-Edge Spectroscopy (XANES) spectrum can be extracted for each pixel in the image, providing information on the concentration of calcium inside intracellular organelles and spectroscopic information on the crystallinity of this Ca-rich phase. In the tomograms of cells all major organelles were visible, as well as intracellular membrane-bound coccoliths in *status nascendi.* To authors surprise, the cells contained distinct intracellular compartments packed with highly absorbing material, which the spectroscopic data showed to be rich in calcium. The XANES spectra collected from multiple Ca-rich compartments were clearly different from the spectra of coccolith calcite and exhibited characteristics of disordered local environment around the calcium atoms (Fig. 8).

The here presented data provides the first insights on the spatial distribution of calcium in coccolithophorid cells. The authors discovered high amounts of calcium to be concentrated in membrane-bound compartments that are separate from the coccolith producing compartment and they propose that this calcium pool is used for coccolith calcite formation. Inside the compartment calcium is stored as a disordered phase. This

finding makes it tempting to speculate that a major fraction of the coccolith calcium is transported as intermediate calcium phase to the site of calcite formation. What is the exact chemical composition of these intermediate phases, and how material is allocated in and out of the compartments is still elusive.

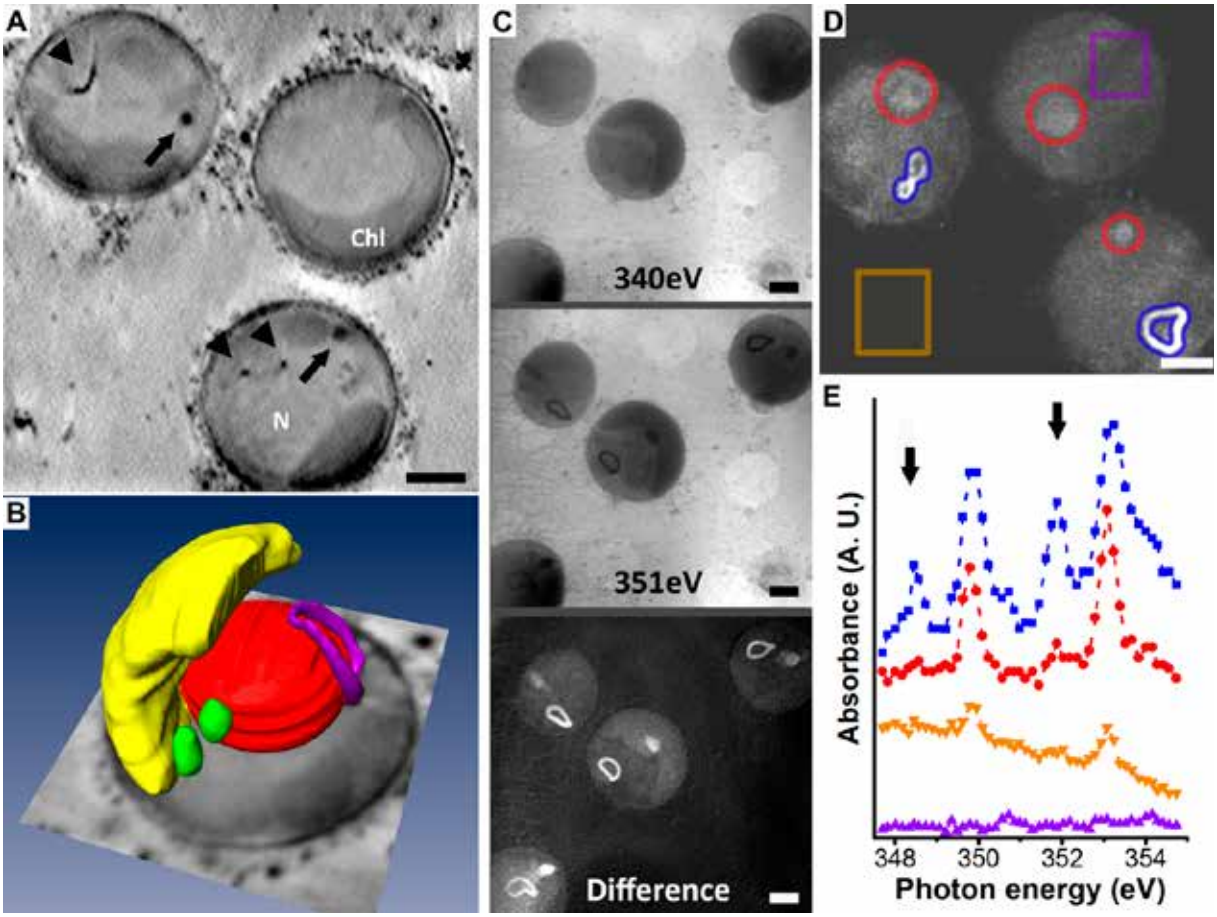

Figure 8: A) Virtual slice of the reconstructed tomogram showing 3 *E. huxleyi* cells. Immature coccoliths and calcium-rich bodies are marked by arrowheads and arrows, respectively. B) Segmented volume of a tomogram with the nucleus in red, the chloroplast in yellow, the intracellular coccolith in violet and the calcium-rich bodies in green. C) Soft X-ray projections recorded below the Ca L_3 edge (top), at the edge (middle) and the absorption difference (bottom). D & E) XANES spectra at the Ca $L_{3,2}$ edge of the different features shown in D. Scale bars: 1 µm.

AFFILIATION:

1. Max-Planck Institute of Molecular Plant Physiology, Potsdam-Golm 14476, Germany.
2. Department of Biomaterials, Max-Planck Institute of Colloids and Interfaces, Potsdam-Golm 14476, Germany.
3. Carl Zeiss Microscopy GmbH, Global Applications Support, Oberkochen 73447, Germany.
4. Department of Geomaterials, GeoForschungsZentrum Potsdam, Potsdam 14473, Germany.
5. ALBA Synchrotron, Cerdanyola del Vallès,Barcelona 08290, Spain.

SCIENTIFIC RESULTS

CATALYSIS

Water affinity and surface charging at the Z-cut and Y-cut $LiNbO_3$ surfaces: An Ambient Pressure XPS Study

The Journal of Physical Chemistry C, **120** (4): 24048-24055 (2016) doi: 10.1021/acs.jpcc.6b05465

Kumara Cordero[1], Laura Rodríguez[1], Annalisa Calò[1], Ma Jose Esplandiu[1], Virginia Pérez-Dieste[2], Carlos Escudero[2], Neus Domingo[1], Albert Verdaguer[1*]

Ferroelectric materials are polar materials with a permanent electric dipole below a certain transition temperature. Ferroelectric polarization can be controlled and switched by externally applied electric fields. The stability of ferroelectric phases is strongly determined by the ability of the system to screen huge stray electric fields at the surface. The main extrinsic screening mechanism is mediated by molecules adsorbed from the environment (adsorbates), with water molecules playing an important role due to its polar nature. Understanding the interplay between ferroelectric phase stability, screening and surface adsorbates is key to control ferroelectricity at the nanometer level. X-ray photoelectron spectroscopy (XPS) is a perfect tool to obtain information about the chemical composition of a surface, but environmental conditions are essential. In this sense, the Near-Ambient Pressure XPS (NAPP) endstation of the CIRCE beamline at the ALBA Synchrotron offers excellent opportunities to study FE surface adsorbates by XPS working in different gases and pressures, including water vapor atmosphere. The present study has allowed determining the interplay of water molecules and their reactivity on FE surfaces as a function of polarization direction, and detecting the dominant screening absorbates such as water electrolysis byproducts.

$LiNbO_3$ (LN) is a ferroelectric oxide widely used in nonlinear optics and its (0001) ferroelectric surface has shown promising applications as a chemical sensor. Most of the studies to understand the LN interface have been mainly restricted to vacuum while the interfaces in ambient conditions are still poorly understood. In this work, the positive and negative polar surfaces of (0001) LN (with polarization pointing up and down respectively), also referred as z-cut LN, were studied at different temperature and water pressure conditions using Ambient Pressure XPS (AP-XPS). In addition, other measurements were also carried out on the (1-100) LN surface, commonly referred as nominally non-polar y-cut. By direct comparison of the three interfaces at different conditions it was possible to study the effect of the polar nature of the surface on the adsorbates. From XPS spectra taken at the O1s region it was monitored the evolution of water molecules and negative OH groups at the surface as the water vapor pressure or the temperature were changed. Assuming a multilayer system formed by the $LiNbO_3$ surface, hydroxyl groups and molecular water, thickness of the adsorbate layer can be calculated in nm or monolayers (ML). Figure 9b shows the thickness of the adsorbates film (water and OH groups) as a function of water vapor pressure. In all three surfaces, there is an increase of the amount of adsorbates as the pressure increases from an initial state of 0.5 nm, with a clear step between 1 mbar and 3 mbar. However the amount of adsorbates is not equivalent for all surfaces: being thicker at the LN y-cut and the

positive LN z-cut crystal surface. The amount of water and OH groups is plotted separately in the Figure 9c and 9d. It is important to remark the difference in OH content for positive and negative LN z-cut surfaces as the pressure increases, related to the formation of the second water ML: this layer activates the diffusion of ionic groups on the surface that allows negative OH groups to migrate from the negative LN z-cut surface due to electrostatic repulsion and their useless role in surface screening. Global discharge of all surfaces associated with the formation of the second water monolayer was also proven by the displacement of the position of the Nb 3d5/2 peak as the water vapor pressure was increased. Desorption of adsorbates with increasing temperature (not shown here) demonstrated that water molecules remain on the negative LN z-cut surface up to 200ºC and for temperatures as high as 300ºC for the positive LN z-cut surface, due to the strong adsorption mediated by OH groups and screening activity.

The measurements univocally indicate the presence of OH groups at the surface when exposed to water vapor, giving evidence of partial dissociation of water molecules at the surfaces. When water adsorption is compared directly between positive and negative LN z-cut surfaces a preferential adsorption on positive surface is observed, with a general transition from coverage of 1ML to a 2ML of H_2O in the range of 1 to 3 mbar of pressures. The adsorption of water molecules at the surface can be directly correlated with the presence of OH groups on the surface, which seem to play a predominant role for water molecules adsorption beyond the dipolar electric interactions due to polarization states of the surface. On the other hand, surface ionic mobility is strongly correlated with the presence of the second water ML, which seems to trigger both, general surface discharge and adsorbates screening effects. The stronger affinity of water for the polar LN z-cut positive surface persists as a function of temperature.

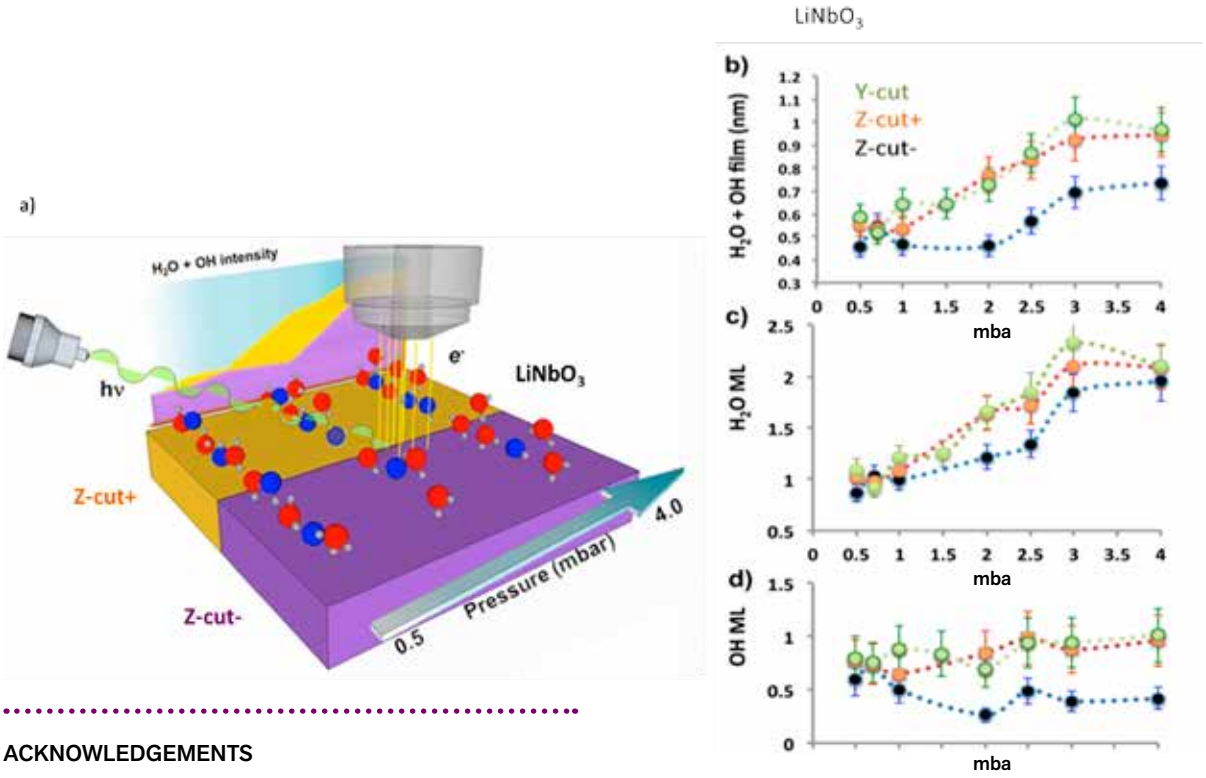

Figure 9: a) Schematics of the XPS experiments: water molecules in red, OH groups in blue. b), c), d) Thickness of water and OH groups as a function of water vapor pressure.

ACKNOWLEDGEMENTS

This work has been partially funded by the 2014 SGR 1216 project from the Generalitat de Catalunya, the MAT2012-38319-C02-01 and the FIS2013-48668-C2-1-P from the Spanish Ministerio de Economía y Competitividad (MINECO). Dr. Neus Domingo is also grateful to MINECO for the "Ramon y Cajal" contract RYC-2010-06365. ICN2 acknowledges support from the Severo Ochoa Program (MINECO, Grant SEV-2013-0295).

AFFILIATION:

1. Catalan Institute of Nanoscience and Nanotechnology (ICN2), CSIC and The Barcelona Institute of Science and Technology, Campus UAB, Bellaterra, 08193 Barcelona, Spain

2. ALBA Synchrotron, Barcelona 08290, Spain

Strong Impact of the Oxygen Content in $Na_3V_2(PO_4)_2F_{3-y}O_y$ ($0 \leq y \leq 0.5$) on their Structural and Electrochemical Properties

Chemistry of Materials, **28** 7683-7692 (2016) doi: 10.1021/acs.chemmater.6b02659

Thibault Broux[1,2,5], Tahya Bamine[1,5], François Fauth[3], Laura Simonelli[3], Wojciech Olszewski[3,4], Carlo Marini[3], Michel Ménétrier[1,5], Dany Carlier[1,5], Christian Masquelier[2,5,6] and Laurence Croguennec[1,5,6]

Up to now, lithium-ion batteries have been shown to be the most efficient technology for the electrochemical energy storage developed for both portable and large scale applications. In order to overcome drawbacks associated to the availability and prize of lithium resources, the sodium-ion technology appears to be a short term reasonable option given that it is similar in terms of materials used and industrial processing. Despite several advantages including lower price and very large earth-abundance of sodium important drawbacks must be overcome to ensure a possible future for the Na-ion technology: a less negative standard reduction potential and a higher molecular mass both contributing to reduce the energy density compared to lithium-ion technology.

Several studies have been recently performed on the promising sodium-ion positive electrode material $Na_3V_2(PO_4)_2F_3$ ($NVPF_3$) which revealed significant discrepancies in structural description and electrochemical properties of $NVPF_3$ [1-5]. From these observations, it clearly stands out that some subtle differences in as-prepared compositions have to be clarified considering especially the effect of a possible presence of oxygen defects induced by synthesis conditions. To elucidate these discrepancies a series of six partially oxidized $Na_3V_2(PO_4)_2F_{3-y}O_y$ compositions with *y* varying from 0 ($NVPF_3$) to 0.5 ($NVPF_{2.5}O_{0.5}$) has been prepared controlling the amount of oxygen defects that governs the initial vanadium oxidation state and studied by synchrotron X-ray diffraction and X-ray absorption spectroscopy at ALBA.

$Na_3V_2(PO_4)_2F_{3-y}O_y$ ($0 \leq y \leq 0.5$) powders were prepared by a two-step solid-state reaction using stoichiometric amounts of $V^{V}OPO_4$, $V^{III}PO_4$, NaF and Na_2CO_3 as precursors annealed in argon at 750 °C according to the following reaction:

$$(3-y)NaF + y/2Na_2CO_3 + (2-y)V^{III}PO_4 + yV^{V}OPO_4 \rightarrow Na_3V^{III}_{2-y}(V^{IV}O)_y(PO_4)_2F_{3-y} + y/2CO_2 + y/4O_2$$

$V^{V}OPO_4$ and $V^{III}PO_4$ were prepared using stoichiometric amounts of V_2O_5 and $NH_4H_2PO_4$ according to one-step (in reducing atmosphere) and two-step (oxidation of $V^{III}PO_4$) solid-state reactions respectively.

High resolution synchrotron powder X-ray diffraction (SXRD) data were collected on the powder diffraction station of the MSPD beamline at ALBA. The powders were placed in a 0.5 mm diameter capillary and data recorded in Debye-Scherrer geometry using the position sensitive detector MYTHEN with a wavelength of 0.9540 Å in the 2θ angular range of 1 – 70 ° with a 0.005 ° step and an accumulation time of 6 minutes. As

already reported for the structural determination of $Na_3V^{III}_2(PO_4)_2F_3$ (y = 0), the use of very high angular resolution techniques is essential as a very small orthorhombic distortion exists[4]. This detection is important to reveal significant changes in the distribution of sodium ions within the 3D framework and thus in the interpretation of electrochemical processes. The SXRD collected are displayed in Figure 10.

Vanadium K-edge X-ray absorption spectra shown in Figure 11 were collected at room temperature in transmission mode using three ionization chambers mounted in series for simultaneous measurements of the sample and reference at the CLÆSS beamline at ALBA. The synchrotron radiation emitted by the CLÆSS multipole wiggler was first vertically collimated and then monochromatised by a Si(111) double-crystal monochromator. The monochromatised beam was then focused down to 100 x 200 μm² at the sample position by a toroidal focusing mirror. Higher harmonic contributions to the selected energy were suppressed by setting the coating and the rejecting angle of the two mirrors. Powder samples were mixed uniformly in boron nitride matrix and pressed into pellets of 13 mm diameter, for obtaining the vanadium K-edge step close to 1. Several X-ray absorption scans were collected to ensure the reproducibility of the spectra and to obtain high signal to noise ratio.

Rietveld refinements of the crystal structure of the whole series of compositions $Na_3V_2(PO_4)_2F_{3-y}O_y$ ($0 \leq y$ 0.5) have been carried out in the *Amam* space group. Partial oxygen substitution for fluorine is compensated by a partial oxidation of V^{III} to V^{IV} and thus by the formation of covalent vanadyl-type bonds $(V^{IV}O)^{2+}$ at the apex of the bi-octahedra, shorter than the ionic bonds V^{III}-F: this evolution explains the decrease of the *c* parameter.

X-ray absorption spectra show a continuous shift towards higher energy for the rising edge which is in good agreement with the continuous oxidation of vanadium, significant changes are also observed in the pre-edge. From the insets given in Figure 11, one can observe that at y = 0 the pre-peak is composed by three features located at 5466, 5468, and 5469.5 eV characteristic of the V^{III} state. The increase of y also leads to an increase of the contribution at 5469.5 eV which is characteristic of a V^{IV} state. Moreover, a constant growth of the global intensity of the pre-edge is observed as a function of y.

Concerning the electrochemical properties, as y increases the average potential of the cell continuously decreases, as highlighted by the shift of the derivative peaks to lower voltages on Figure 12. The average voltage of the cell varies from 3.89 V for y = 0 to 3.83 V for y = 0.5. It is ascribed to the formation of highly covalent vanadyl-type bonds $(V=O)^{2+}$ at the apex of the bi-octahedra $V_2O_8F_{3-y}O_y$ that "continuously" replace the more ionic V-F bonds as y increases.

The electrochemical voltage-composition data differ significantly in their shape depending on the composition in oxygen: the more oxidized the compound, the "smoother" their cycling profiles. In the low voltage domain, for y = 0 and 0.1 two

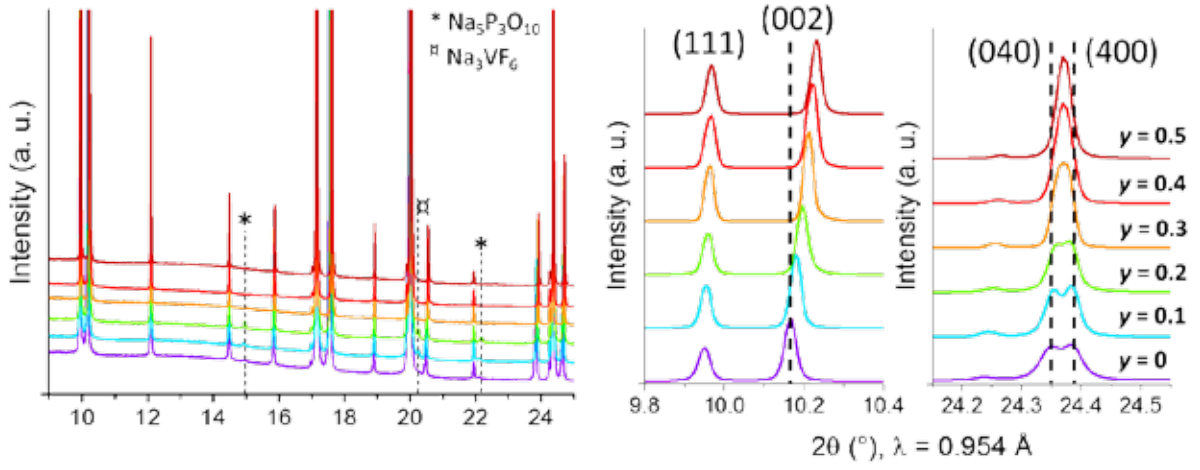

Figure 10: Left: comparison of the experimental synchrotron XRD patterns recorded for the six samples $Na_3V_2(PO_4)_2F_{3-y}O_y$ ($0 \leq y \leq 0.5$). The patterns are cut at the quarter of the total intensity to highlight impurities - Right angular ranges [9.8 - 10.4°] and [24.15 - 24.55°] are given for easier comparison. The indexation of the diffraction lines is given in the Amam space group.

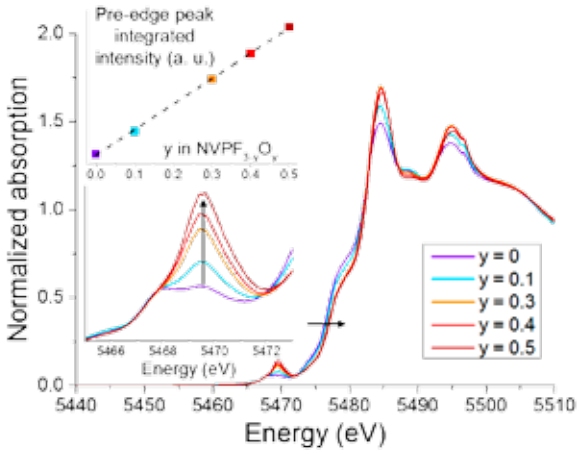

Figure 11: Vanadium K-edge XANES spectra of the samples $Na_3V_2(PO_4)_2F_{3-y}O_y$ ($0 \leq y \leq 0.5$). The insets show an enlarged graph of the pre-edge region and the associated integrated intensity.

sharp peaks are clearly observed around 3.7 V in the derivative data whereas for the more oxidized compounds only one broader and asymmetric peak is observed. In the high voltage domain, a similar behavior is observed with an evolution from sharp peaks around 4.2 V for $y = 0$ to broader peaks for more oxidized compositions. This emphasizes that a small change in their initial compositions and thus in their vanadium average oxidation states has a major impact on the phase diagram stabilized upon cycling. It evolves from a complex series of biphasic domains and solid solutions for $y = 0$, as already determined for $NVPF_3$[5] to an extended solid solution for $y > 0.2$.

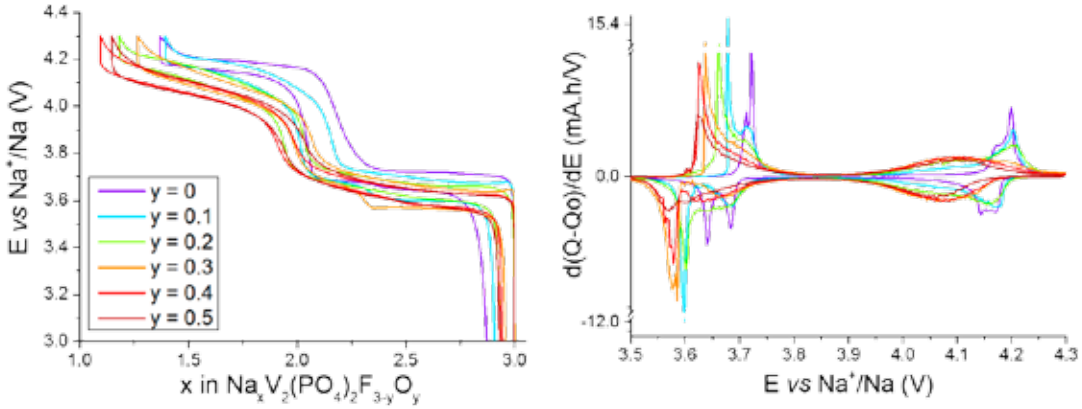

Figure 12: Left: second voltage-composition curve of $Na_{3-x}V_2(PO_4)_2F_{3-y}O_y$ ($0 \leq y \leq 0.5$) cycled at C/20 between 2.5 and 4.3 V – Right: associated derivative curves.

OTHER REFERENCES

[1] Gover, R.; Bryan, A.; Burns, P.; Barker, J., The electrochemical insertion properties of sodium vanadium fluorophosphate, $Na_3V_2(PO_4)_2F_3$. *Solid State Ionics* **177**, 1495-1500 (2006).

[2] Barker, J.; Gover, R.; Burns, P.; Bryan, A., Hybrid-ion a lithium-ion cell based on a sodium insertion material. *Electrochem. Solid St.* **9**, A190-A192 (2006).

[3] Liu, Z.; Hu, Y.-Y.; Dunstan, M. T.; Huo, H.; Hao, X.; Zou, H.; Zhong, G.; Yang, Y.; Grey, C. P., Local Structure and Dynamics in the Na Ion Battery Positive Electrode Material $Na_3V_2(PO_4)_2F_3$. *Chem. Mater.* **26**, 2513-2521 (2014).

[4] Bianchini, M.; Brisset, N.; Fauth, F.; Weill, F.; Elkaim, E.; Suard, E.; Masquelier, C.; Croguennec, L., $Na_3V_2(PO_4)_2F_3$ revisited: a high-resolution diffraction study. *Chem. Mater.* **26**, 4238-4247 (2014).

[5] Bianchini, M.; Fauth, F.; Brisset, N.; Weill, F.; Suard, E.; Masquelier, C.; Croguennec, L., Comprehensive Investigation of the $Na_3V_2(PO_4)_2F_3$ – $NaV_2(PO_4)_2F_3$ System by Operando High Resolution Synchrotron X-ray Diffraction. *Chem. Mater.* **27**, 3009-3020 (2015).

ACKNOWLEDGEMENTS

The authors thank Philippe Dagault, Cathy Denage and Laetitia Etienne at ICMCB for technical assistance, Rénald David at LRCS for the preparation of the electrolyte, as well as ALBA (Barcelona, Spain) for Synchrotron X-ray diffraction and absorption experiments on MSPD and CLÆSS beamlines. The authors also acknowledge RS2E for the funding of TB's postdoctoral fellowship. This project has received funding from Région Aquitaine, the French National Research Agency (STORE-EX Labex Project ANR-10-LABX-76-01 and SODIUM Descartes project ANR-13-RESC-0001-02), and the European Union's Horizon 2020 research and innovation programme under grant agreement No 646433-NAIADES. The Mésocentre de Calcul Intensif Aquitain (MCIA) and the modelling center of ISM are acknowledged for computing facilities.

AFFILIATION:

1. CNRS, Univ. Bordeaux, Bordeaux INP, ICMCB UPR 9048, F-33600 Pessac, France.
2. Laboratoire de Réactivité et Chimie des Solides, CNRS-UMR#7314, Université de Picardie Jules Verne, F-80039 Amiens Cedex 1, France
3. ALBA Synchrotron, E-08290 Cerdanyola del Vallès, Barcelona, Spain
4. Faculty of Physics, University of Bialystok, 1L K. Ciolkowskiego Str., 15-245 Bia lystok, Poland
5. RS2E, RéseauFrançais sur le StockageElectrochimique de l'Energie, FR CNRS 3459, F-80039 Amiens Cedex 1, France
6. ALISTORE-ERI EuropeanResearchInstitute, FR CNRS 3104, F-80039 Amiens Cedex 1, France

First direct observation of the development of tailored mesoporosity within zeolites

In situ Time Resolved Observation of the Development of Intracrystalline Mesoporosity in USY Zeolite. _Chemistry of Materials_, 28 (24):8971 – 8979, (2016) doi: 10.1021/acs.chemmater.6b03688

Noemi Linares[1], Alexander Sachse[1], Elena Serrano[1], Aida Grau-Atienza[1], Erika Oliveira Jardim[1], Joaquín Silvestre-Albero[2], Marco Aurelio Liutheviciene Cordeiro[3], François Fauth[4], Garikoitz Beobide[5], Oscar Castillo[5], Javier García-Martínez[1,6,*]

Zeolites are a class of microporous crystalline materials widely applied in industrial processes. Yet, the sole presence of microporosity causes important diffusion limitations, hampering some of their applications [1]. One of the most exciting techniques to minimize the diffusion limitations in zeolites is the reconstruction of the zeolite crystals to accommodate new surfactant-templated mesoporosity [2,3].

Up to date, the use of in situ X-ray strategies has been limited to study the development of ordered mesoporosity in the X-ray small angle region, or to follow the zeolite crystallization processes in the wide angle range [4,5]. In this work, authors study the formation of surfactant-templated zeolites, presenting the first real time *in situ* observation of the development of tailored mesoporosity within zeolites through the use of XRD synchrotron radiation covering the entire diffraction range (small and wide angle regions).

Synchrotron experiments were performed on the powder diffraction station of the BL04-MSPD beamline of the ALBA synchrotron located in the Barcelona area, Spain [6]. Data were collected in transmission mode using the position sensitive detector MYTHEN allowing to collect in a single shot a 40 deg. angular range in 0.006 deg. steps. In order to properly define the lowest angle peak, patterns were recorded at the relatively long wavelength, $\lambda = 0.9539$ Å, and with the sample filled in a 1.0-mm-diameter borosilicate capillary. Data were registered at room temperature and on heating at 353 K and 373 K. High temperatures were achieved using a Cyberstar hot air blower (and/or a liquid nitrogen cryostream, Oxford Cryosystems Series700Plus). Sample preparation for *in situ* synchrotron experiments was carried out as follows [7,8]: CTAB (0.5 g) was dissolved in 6.3 mL of a 0.38 M NaOH aqueous solution. To this solution was added 1 g of USY zeolite and the obtained mixture was stirred at RT for 20 min. An aliquot of the mixture was introduced in a sealed 1.0 mm-diameter borosilicate capillary, as shown in Fig. *13* and the synthesis was carried out for the indicated time at 353 K and 373K. The homogeneity of sample distribution inside the capillary, of the reactants, and the temperature during the process was ensured through constant rotation of the capillary. The diffractograms were recorded from 0 - 40º 2θ with time intervals of 5 min (Fig. 14) allowing for the concurrent study of the kinetics of both the development of mesoporosity and the evolution of the crystallinity of the samples throughout the entire mesostructuring treatment.

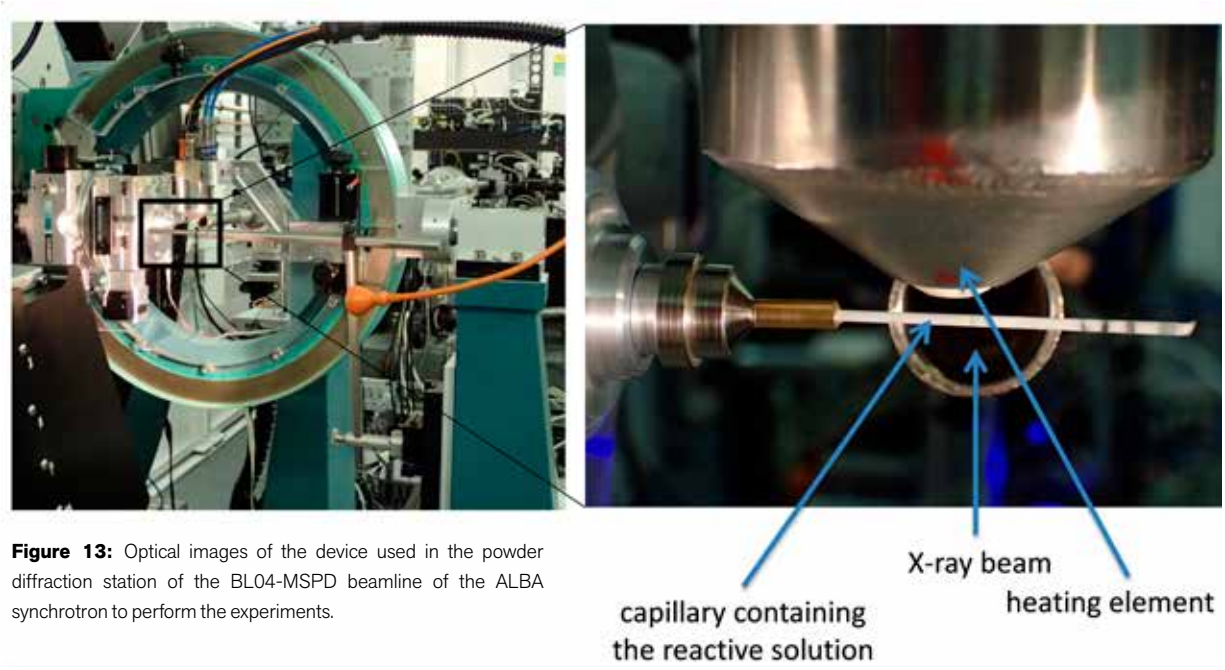

Figure 13: Optical images of the device used in the powder diffraction station of the BL04-MSPD beamline of the ALBA synchrotron to perform the experiments.

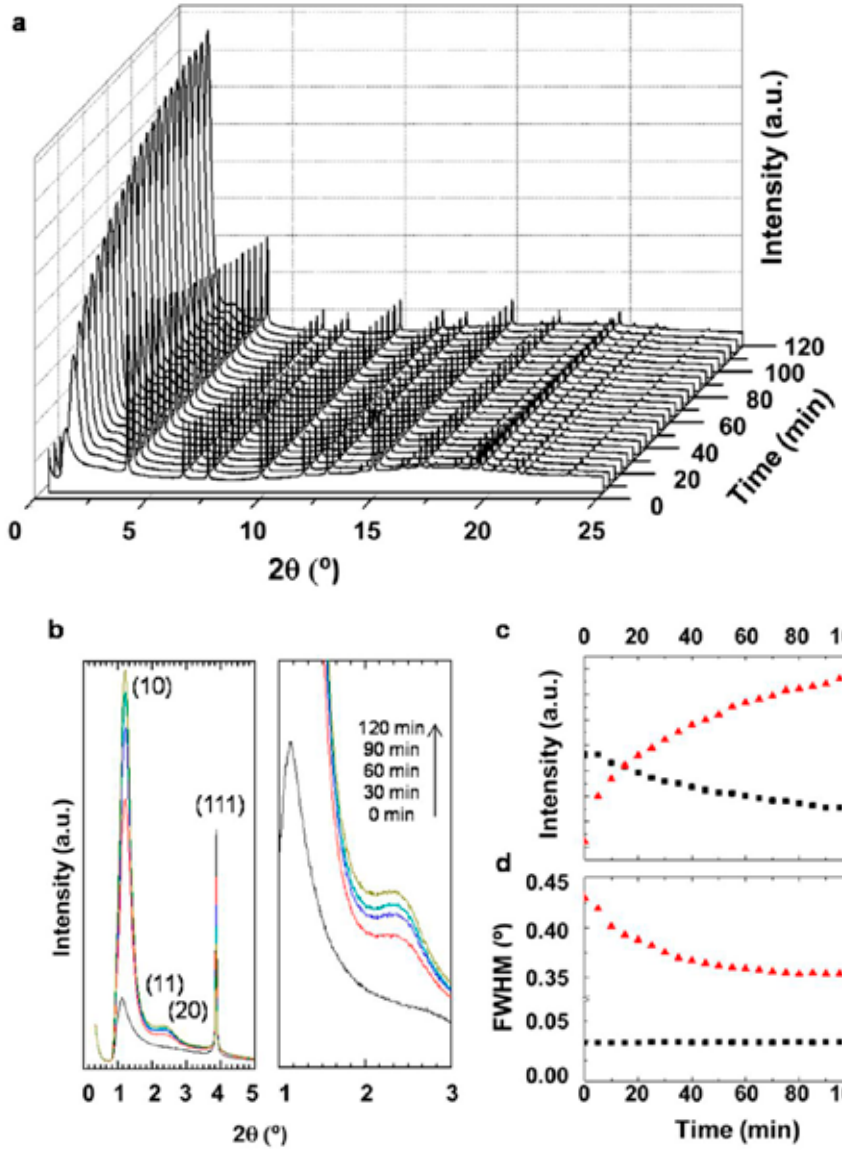

Figure 14: *In situ* time resolved synchrotron XRD study of USY zeolite surfactant-templating. (**a**) Time resolved synchrotron XRD patterns of USY zeolite during surfactant-templating at 373 K. (**b**) Selected XRD patterns at 0 min (black), 30 min (red), 60 min (blue), 90 min (turquoise) and 120 min (brown). (**c**) Intensities and (**d**) FWHM of the peaks at 1.24º (red triangles) and 3.84º (black squares) 2θ as a function of time.

Experiments where CTAB was replaced by the same amount per weight of TPABr were carried out by using the same procedure. Finally, solid samples prepared in *ex situ* conditions were also analyzed, by filling the 1.0 mm-diameter borosilicate capillaries with the samples.

The development of intracrystalline mesoporosity within zeolites has been a long standing goal in catalysis as it greatly contributes to alleviate the diffusion limitations of these widely used microporous materials. The combination of *in situ* synchrotron X-ray diffraction and Liquid Cell Transmission Electron Microscopy (Liq-TEM) allowed for the first in situ observation of the development of intracrystalline mesoporosity in zeolites and to gain structural and kinetic information on the changes produced in zeolites to accommodate the mesoporosity. The interpretation of the time resolved diffractograms together with computational simulations evidenced the formation of short-range hexagonally ordered mesoporosity within the zeolite framework and the *in situ* electron microscopy studies allowed for the direct observation of structural changes in the zeolite during the process. The evidences on the templating and protective role of the surfactant and the rearrangement of the zeolite crystal to accommodate intracrystalline mesoporosity open new and exciting opportunities for the production of tailored hierarchical zeolites.

Combining the experimental diffractograms with theoretical calculations confirmed the presence of local hexagonal order in the zeolite. Moreover, through the observation of individual zeolite crystals in Liq-TEM, the authors were able to provide the first time-resolved visualization of the crystal reconstruction during surfactant templating. All of these new insights that have been obtained by combining, for the first time, multiple time-resolved techniques are an excellent example of the importance and enormous potential of current in situ characterization methods and contribute toward the rational design of hierarchical zeolites with superior properties and optimal catalytic performance.

ACKNOWLEDGEMENTS

Authors acknowledge the ALBA synchrotron for beamtime availability (Project ID: 2015021271) and the Center for Functional Nanomaterials at the Brookhaven National Laboratory for the Liq-TEM availability. The authors further acknowledge the CAPITA Project WAVES (EP7-NMP- 266543) for financial support.

OTHER REFERENCES

[1] García Martínez, J.; Li, K. *Mesoporous Zeolites: Preparation, Characterization and Application*, Wiley (2015).

[2] Prasomsri, T.; Jiao, W.; Weng, S. Z.; García-Martínez, J. Mesostructured Zeolites: Bridging the Gap between Zeolites and MCM-41, *Chem. Commun.* **51**, 8900-8911 (2015).

[3] Li, K.; Valla, J.; García-Martínez, J. Realizing the Commercial Potential of Hierarchical Zeolites: New Opportunities in Catalytic Cracking, *ChemCatChem.* **6**, 46-66 (2014).

[4] Norby, P. In-Situ XRD as a Tool to Understanding Zeolite Crystallization, *Curr. Opinion Coll. & Interface Sci.* **11**, 118-125 (2006).

[5] Flodström, K.; Wennerström, H.; Teixeira, C. V.; Amenitsch, H.; Linden, M.; Alfredsson, V. Time-Resolved in Situ Studies of the Formation of Cubic Mesoporous Silica Formed with Triblock Copolymers, *Langmuir* **20**, 10311-10316 (2004).

[6] Fauth, F.; Peral, I.; Popescu, C.; Knapp, M. The new Material Science Powder Diffraction beamline at ALBA Synchrotron, *Powder Diffraction* **28**, S360-S370 (2013).

[7] García-Martínez, J.; Xiao, C.; Cychosz, K. A.; Li, K.; Wan, W.; Zou, X.; Thommes, M. Evidence of Intracrystalline Mesostructured Porosity in Zeolites by Advanced Gas Sorption, Electron Tomography and Rotation Electron Diffraction, *ChemCatChem* **6**, 3110-3115 (2014).

[8] García-Martínez, J.; Johnson, M.; Valla, J.; Li, K.; Ying, J. Y. Mesostructured Zeolite.Y - High Hydrothermal Stability and Superior FCC Catalytic Performance, *Catal. Sci. Technol.* **2**, 987-994 (2012).

AFFILIATION:

1. Laboratorio de Nanotecnología Molecular, Departamento de Química Inorgánica, Universidad de Alicante, Ctra. San Vicente-Alicante s/n, E-03690 San Vicente del Raspeig, Spain.
2. Laboratorio de Materiales Avanzados, Departamento de Química Inorgánica-Instituto Universitario de Materiales, Universidad de Alicante, Ctra. San Vicente-Alicante s/n, E-03690 San Vicente del Raspeig, Spain.
3. Center for Functional Nanomaterials, Brookhaven National Laboratory, Upton, NY 11973, USA.
4. ALBA Synchrotron, 08290 Cerdanyola del Vallés, Barcelona, Spain.
5. Departamento de Química Inorgánica, Facultad de Ciencia y Tecnología, Universidad del País Vasco UPV/EHU, Apartado 644, E-48080 Bilbao, Spain.
6. Rive Technology, Inc., 1 Deer Park Drive, Monmouth Junction, NJ 08852, USA.

MAGNETISM

Emerging diluted ferromagnetism in high-T_c superconductors driven by point defect clusters

Advanced Science **3**, 1500295 (2016) doi: 10.1002/advs.201500295

J. Gazquez[1,*], R. Guzman[1], R. Mishra[2,3,4], E. Bartolomé[5], J. Salafranca[6,3], C. Magén[7], M. Varela[6,3], M. Coll[1], A. Palau[1], S. M. Valvidares[8], P. Gargiani[8], E. Pellegrin[8], J. Herrero-Martin[8], S. J. Pennycook[9], S.T. Pantelides[2,3], T. Puig1, X. Obradors[1]

Although $YBa_2Cu_3O_{7-\delta}$ (YBCO) is one of the most studied compounds in materials science's history since its discovery in the 80's, it is still capable of bringing exciting surprises. A good example is what J. Gazquez and co-authors have unveiled, a previously unforeseen point defects buried in YBCO thin films that lead to the formation of ferromagnetic clusters embedded within the superconductor. Superconductivity and ferromagnetism are considered to be naturally exclusive phenomena; however, their results reveal the coexistence of ferromagnetic interactions much closer to high Tc superconductivity than previously suspected, which presents fundamental new physical insights. The combination of the advanced techniques used in this work constitutes a step forward to underscore new phenomena probing nanoscale functionalities such as magnetism at the atomic-scale and its influence to macroscopic phenomena such as diluted ferromagnetism and superconductivity.

The high-temperature superconductor (HTS) YBCO is one of the most impressive and yet challenging materials, from both a fundamental viewpoint for understanding HTS theory and for its technological applications, as the capacity to design nanoscale defects to strongly pin magnetic vortices has made it the preferred superconducting material for ultrahigh magnetic field applications. Amongst the various nano-scale defects reported in YBCO, the Cu-O double chain is the most common one, regardless of the growth technique of the thin films. This is the so-called $Y_2Ba_4Cu_{8-Y}O_{16-\delta}$ (Y124) intergrowth, which is essentially an extra Cu-O atomic plane within the YBCO. The authors work unveiled the complex nature of this defect. First, using aberration-corrected scanning transmission electron microscopy (STEM) imaging and spectroscopy, they showed how the system solves the local off-stoichiometry induced by the extra Cu-O chain: these common intergrowths should be pictured as double chains with quasi-1D arrays of defect clusters including two Cu vacancies decorated by three O vacancies embedded in particular chains. Secondly, by combining the STEM results with density functional theory (DFT) calculations, the authors predicted these defect clusters within the superconducting material to have robust magnetic moments with ferromagnetic ordering. Finally, they used X-ray magnetic circular dichroism (XMCD) spectroscopy, which provides evidence of Cu magnetic moments and the presence of a dilute network of magnetic defects within the high T_c superconducting state (Fig. 15). From the XMCD experiments performed in the ALBA Synchrotron, a model was proposed in which the magnetism of Cu atoms in superconducting YBCO films is explained in terms of a superparamagnetic behavior of isolated ferromagnetic clusters, even below the superconducting transition temperature.

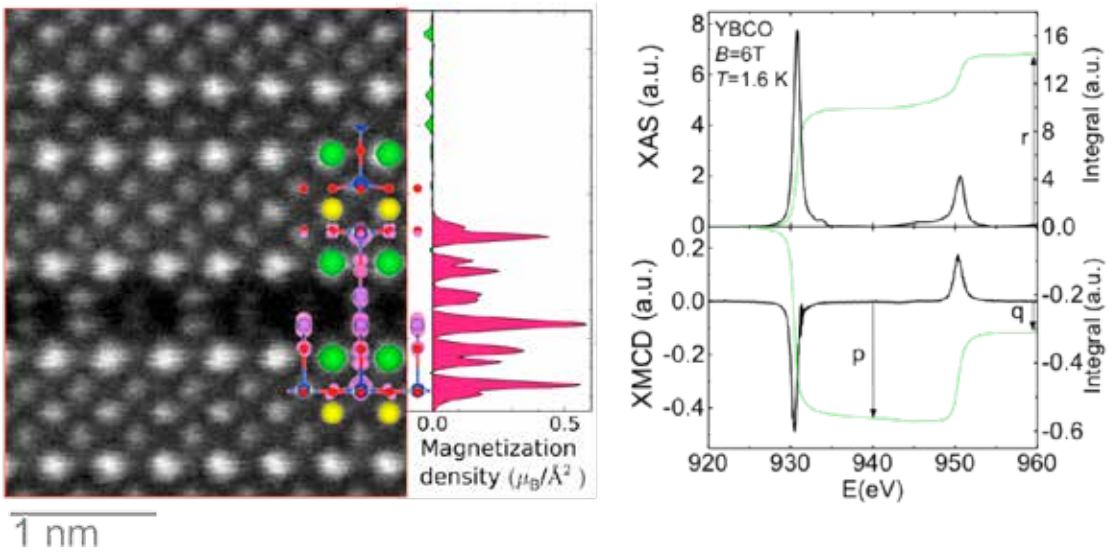

Figure 15: Left panel, Z-contrast atomic resolution image of the YBCO lattice with an Y124 intergrowth imaged along the [010] direction. The dimmer contrast in the double Cu ($2V_{Cu}$) chain is due to the presence of Cu vacancies ($2V_{Cu}$). The inset shows the isosurface plot showing the spin density associated with a $2V_{Cu}+3V_O$ defect along with an integrated magnetization/area profile along the *z*-axis. Right panel, Cu $L_{2,3}$ edge (top) background-subtracted XAS and (bottom) XMCD spectra measured at 6 T, 1.6 K in normal incidence (θ=0°) for a YBCO thin-film.

ACKNOWLEDGEMENTS

Authors acknowledge the MICIN (NANOSELECT, CSD2007-00041 and MAT2014-51778-C2-1-R), Generalitat de Catalunya (2014SGR 753 and Xarmae) and the EU (EU-FP7 NMP-LA-2012-280432 EUROTAPES project and Cost Action MP1201). They also acknowledge MINECO for the Center of Excellence award Severo Ochoa (SEV-2015-0496). Work at ORNL was supported by the US DOE Office of Basic Energy Sciences, Materials Sciences and Engineering Division (M.V., S.J.P.) and by the Scientific User Facilities Division. Some of the electron microscopy work has also been conducted in the Laboratorio de Microscopias Avanzadas (LMA) at Instituto de Nanociencia de Aragon (INA) at the University of Zaragoza. Work at INA-LMA was supported by NanoAraCat. Research at UCM (J.S.) was supported by the ERC starting Investigator Award, grant no. 239739 STEMOX and Juan de la Cierva Program JCI-2011-09428 (MICINN-Spain). The XMCD experiments were performed at the BOREAS beamline of the ALBA Synchrotron with the collaboration of ALBA staff. M.V., E.P. and P.G. acknowledge funding by MINECO through programa Retos de la Sociedad (FIS2013-45469-C4-3-R). Research at Vanderbilt was supported by the U.S. DOE grant DE-FG02-09ER46554 and the McMinn Endowment. Computations were supported by the NERSC (U.S. DOE, DE-AC02-05CH11231). J.G. and M.C. also acknowledge the Ramon y Cajal program (RYC-2012-11709 and RYC-2013-12448 respectively).

This work has demonstrated a novel dilute ferromagnetic-superconducting multifunctionality, as the ferromagnetic order of those Cu belonging to the CuO2 planes and surrounding the O-decorated Cu vacancies does not vanish when superconductivity sets in at Tc. Instead, their ferromagnetic state concurs/coexists with the superconducting state of the rest of Cu of the superconducting planes. The presence of these two phases, and the shortness of the superconducting coherence length of YBCO, may lift the degeneracy of the spin-up and spin-down of the Cooper pairs and cause a pair breaking. As a result, one may wonder if this novel ferromagnetic behavior could play a role in pinning vortices. The aim of the researchers is to continue exploring new defects landscapes designing nano-scale defects to strongly pin magnetic pinning and making these materials more efficient in the presence of high magnetic fields.

AFFILIATION:

1. Institut de Ciència de Materials de Barcelona (ICMAB-CSIC), Bellaterra, Spain
2. Department of Physics and Astronomy, Vanderbilt University, Nashville, TN 37235, USA
3. Materials Science and Technology Division, Oak Ridge National Laboratory, Oak Ridge, TN 37830, USA
4. Department of Mechanical Engineering and Materials Science, Washington University in St. Louis, St. Louis, MO 63130, USA
5. Escola Universitària Salesiana de Sarrià (EUSS), Barcelona, Spain
6. Universidad Complutense de Madrid. Madrid 28040, Spain
7. Laboratorio de Microscopías Avanzadas, Instituto de Nanociencia de Aragón – ARAID, Universidad de Zaragoza, Zaragoza 50018, Spain
8. ALBA Synchrotron, Barcelona, Spain
9. Department of Materials Science and Engineering, National University of Singapore, Singapore

Enhanced Curie temperature of a two-dimensional magnetic rare-earth noble-metal alloy

High Temperature Ferromagnetism in GdAg2 Monolayer, *Nano Letters* 16(7):4230-4235 (2016) doi: 10.1021/acs.nanolett.6b01197

M. Ormaza[1,2], L. Fernández[3,4], M. Ilyn[5], A. Magaña[5,1], B. Xu[6], M. J. Verstraete[6], M. Gastaldo[7], M. A. Valbuena[7], P. Gargiani[8], A. Mugarza[7,9], A. Ayuela[5,4], L. Vitali[5,10], M. Blanco-Rey[11,4], F. Schiller[5,3], and J. E. Ortega[1,5,4*]

Fundamental research on magnetism, as well as many potential nanotechnology applications on spintronics, relies on the ability to fabricate interfaces of magnetic materials with superconductors, topological insulators, and semiconductors. However, tailoring magnetic properties on structurally robust substrates is not easy, since the survival of the long-range magnetic order at the interface is mandatory. This is the reason why, besides structural stability and chemical inertness, substrate materials with strong ferromagnetism, i.e., high Curie temperatures T_C, are sought. High T_C's are readily found at the surface of some elementary ferromagnetic materials, but contacting them with other materials often results in intermixing, and finally, lack of structural and magnetic control.

The monolayer-thick $GdAg_2$ alloy combines the three optimal substrate properties, namely, structural stability, nanoscale modulation, and ferromagnetism. Authors used scanning tunneling microscopy (STM), X-ray magnetic circular dichroism (XMCD), and magneto-optic Kerr effect (MOKE) to probe the excellent crystal quality and the ferromagnetic order of the $GdAg_2$ monolayer grown on Ag(111), which exhibits a surprisingly high Curie temperature above 80 K (Fig. 16). First principle calculations and photoemission experiments reveal the particular electronic properties of the $GdAg_2$ monolayer, which in turn explain the high T_c value observed.

The ferromagnetic transition of the $GdAg_2$ surface alloy has been determined at the BOREAS beamline of the ALBA Synchrotron with XMCD (Figure 17a,b) and at the laboratory in San Sebastian with MOKE (Figure 17c,d), by analyzing in both cases temperature-dependent magnetization loops. In XMCD experiments the Gd $M_{4,5}$ absorption edge is measured with circularly polarized light. The absorption spectra for left and right helicities are shown in Figure 17a. They reveal a clear intensity difference (dichroism), which is maximum at the M_5 absorption edge ($h\nu$ = 1183.5 eV). The loops shown in the inset of Figure 17a represent the magnetization M measured as a function of the applied magnetic field $\mu_0 H$. The curves reveal that only a single magnetic phase is present in the sample, namely, a ferromagnetic phase with an in-plane easy magnetization axis. In the out-of-plane direction zero remanence is observed, while the magnetization increases linearly up to the saturation. This is expected in the Stoner–Wolfarth model for uniaxial systems magnetized perpendicular to the easy axis. Since the coercivity of the $GdAg_2$ ($H_c \approx 1$ mT) is much lower than the H-field accuracy in XMCD, one cannot observe the hysteresis loop opening expected in grazing incidence. The Arrott plot analysis of Figure 17b

represents M^2 versus $\mu_0 H/M$ determined from out-of-plane magnetization loops recorded at different substrate temperatures. The linear extrapolation of the data at higher fields intersects the origin $\mu_0 H/M = 0$ at M_0^2. A second order polynomial fit of $M_0^2(T)$ data yields the Curie temperature of 80 K.

With first principal calculations and photoemission experiments it was investigated the origin of the magnetism in this rare-earth noble-metal surface compound, which is based on a RKKY type interaction. There, the magnetic coupling is effectively mediated by the noble metal–Gd hybrid s,p–d bands. Direct comparison with the isostructural $GdAu_2$ monolayer indicates that the higher degree of surface confinement and electron occupation of such hybrid s,p–d bands and $GdAg_2$ promote its much higher Curie temperature.

In summary, the monolayer-thick ferromagnetic $GdAg_2$ alloy exhibits a surprisingly high Curie temperature of 85 K. A comprehensive experimental and theoretical investigation of the electronic structure has been carried out in parallel with the structurally identical $GdAu_2$. The analysis points to RKKY-like interaction mediated by s,p–d Ag(Au)–Gd hybrid bands, whose variable filling explains the increasing T_C from $GdAu_2$ to $GdAg_2$. The importance of this class of surface-confined alloys stems from its nanoscale, moiré modulation and stability upon interface formation. The $GdAg_2$/Ag(111) substrate appears as an ideal candidate to investigate new forms of magnetic coupling with nanoscale ferromagnets, as well as to study the exotic physics at the interface with semiconductor or superconductor materials. These results encourage systematic investigations of rare-earth/noble metal surface alloys and interfaces, in order to exploit them in magneto-electronic applications.

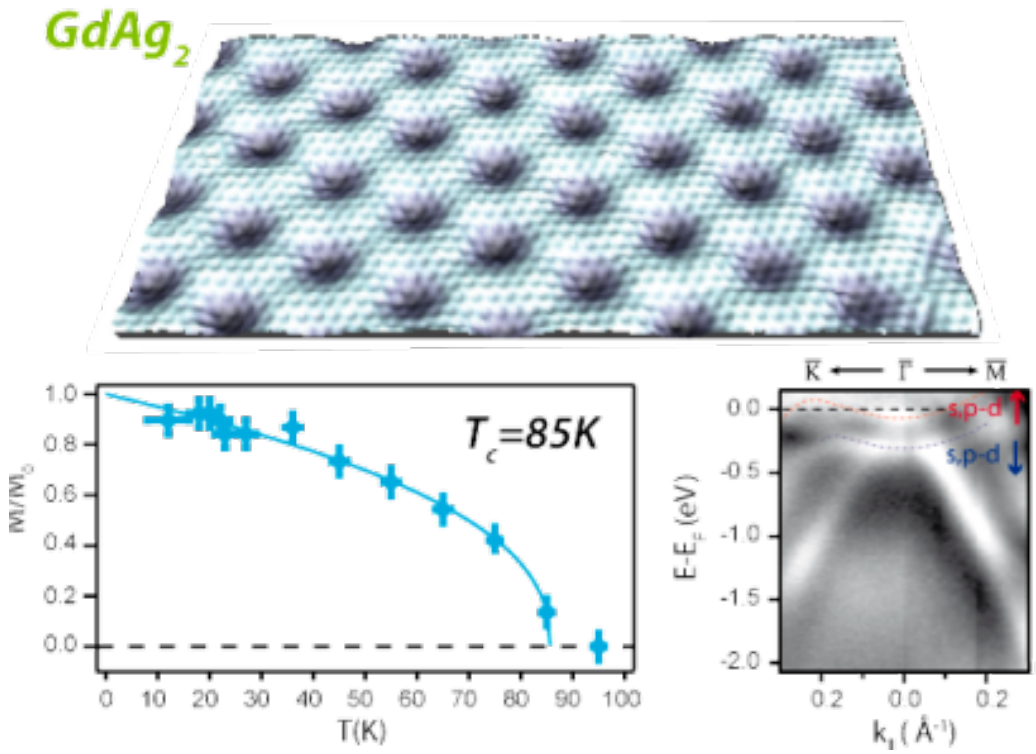

Figure 16: $GdAg_2$ surface alloy grown on Ag(111). The STM image reveals atomic resolution and the additional Moiré pattern of the surface. The Curie temperature was determined as T_c = 85 K by XMCD and MOKE (figure) measurements. This extraordinarily- high Curie temperature is explained by the peculiar surface confinement and filling of the s,p-d hybrid band, which was measured with angle-resolved photoemission.

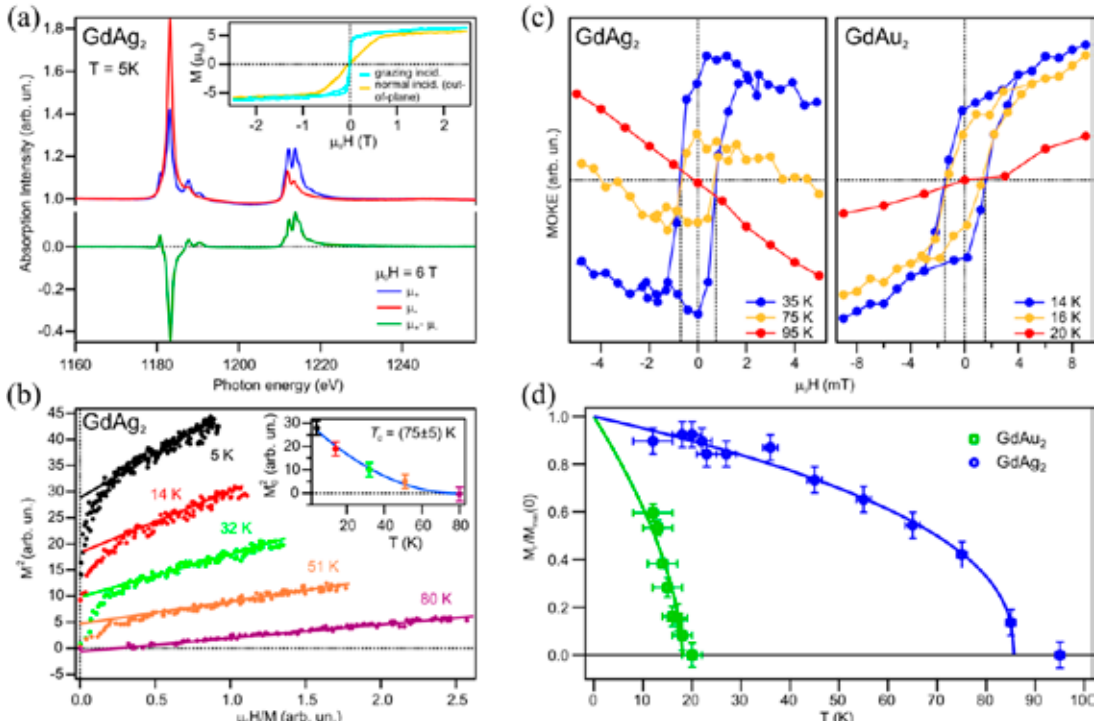

Figure 17: Ferromagnetic transition in $GdAg_2$ and $GdAu_2$: (a) X-ray absorption spectra (normal incidence) of a $GdAg_2$ monolayer taken at T = 5 K and $\mu_0 H$ = 6 T, at the Gd $M_{4,5}$ edge with light of different helicity (top), and the resulting X-ray magnetic circular dichroism (XMCD) difference spectrum (bottom). Inset: magnetization curve obtained from the M_5 absorption peak recorded as a function of the applied field. (b) Arrott plot analysis derived from the out-of-plane XMCD hysteresis loops at different temperatures. The linear fit to high magnetic field data intersects the vertical axis at different M_0^2 values, being zero at the Curie temperature (inset). (c) Magneto-optical Kerr effect (MOKE) loops for $GdAg_2$ and $GdAu_2$ recorded at several temperatures. (d) Remanent magnetization at zero applied field, as derived from the MOKE loops. The exponential fit of the data intersects the horizontal axis at the respective Curie temperatures $T_C^{GdAu_2} = 19 \pm 5$ K and $T_C^{GdAg_2} = 85 \pm 6$ K, respectively.

ACKNOWLEDGEMENTS

This work was supported by the Spanish Government (MAT2013-46593-C6-4-P, MAT2013-46593-C6-5-P, FIS2013-48286-C02-02-P, FIS2013-48286-C02-01-P), the Basque Government (IT621-13,IT627-13,IT756-13), the Diputación de Gipuzkoa (RF-0061/2015), and the Deutsche Forschungsgemeinschaft (SFB 1083 "Structure and Dynamics of Internal Interfaces"). A.Mu., M.A.V., and M.G. acknowledge the Severo Ochoa program SEV-2013-0295. B.X. and M.J.V. acknowledge two A.R.C. grants (TheMoTherm 10/15-03 and AIMED 15/19-09) from the Communauté Française de Belgique. Computer time was made available by PRACE-2IP and 3IP (EU FP7 Grant No. RI-283493 and RI-312763), CECI, SEGI-ULg, and the DIPC.

AFFILIATION:

1. Universidad del País Vasco, Dpto. Física Aplicada I, E-20018 San Sebastián, Spain
2. IPCMS, CNRS UMR 7504, Université de Strasbourg, 67034 Strasbourg, France
3. Fachbereich Physik und Zentrum für Materialwissenschaften, Philipps-Universität, 35032 Marburg, Germany
4. Donostia International Physics Center, E-20018 Donostia-San Sebastián, Spain
5. Centro de Física de Materiales CSIC/UPV-EHU-Materials Physics Center, E-20018 San Sebastián, Spain
6. Université de Liège, Institut de Physique and European Theoretical Spectroscopy Facility (ETSF), allée du 6 août, 17 Sart-Tilman, B-4000 Liège, Belgium
7. Catalan Institute of Nanoscience and Nanotechnology (ICN2), CSIC and The Barcelona Institute of Science and Technology, Campus UAB, Bellaterra, 08193 Barcelona, Spain
8. ALBA Synchrotron, E-08290 Cerdanyola del Vallès, Spain
9. ICREA, Institució Catalana de Recerca i Estudis Avançats, Lluis Companys 23, 08010 Barcelona, Spain
10. Ikerbasque, Basque Foundation for Science, 48013 Bilbao, Spain
11. Universidad del País Vasco, Dpto. Física Materiales, E-20018 San Sebastián, Spain

Spin configuration of cylindrical bamboo-like magnetic nanowires

Journal of Materials Chemistry C **4**, (5): 978-984 (2016) doi: 10.1039/C5TC04194E

C. Bran[1*], E. Berganza[1], E. M. Palmero[1], R. P. Del Real[1], L. Aballe[2], M. Foerster[2], A. Asenjo[1], A. Fraile Rodríguez[3] and M. Vazquez[1]

Cylindrical magnetic nanowires (NWs) are considered for applications in several technological areas such as information technology, microwave devices, functionalization for biomagnetics and, more recently, for thermo-magneto-electric devices [1-3]. All these technological applications require a full understanding and control of the magnetic configurations of the individual wires. These magnetic configurations are determined by the NWs composition and geometry through the balance between the shape, magnetocrystalline and magnetoelastic anisotropies.

The XMCD-PEEM experiments reveal the surface and inner magnetization distribution of individual modulated in diameter (bamboo-like) NWs. Two main configurations are shown: an axial magnetization with pinned vortices at certain modulations for CoFeCu NWs and a vortex-like magnetic domain structure with alternating chirality in the external shell surrounding an axial magnetization core for Co NWs.

Bamboo-like cylindrical NWs with diameters of 130 and 140 nm, and modulation periodicity of 400 nm were electrochemically growth into the pores of alumina template. The NWs crystallographic structure evolves from polycrystalline *bcc* for CoFeCu to monocrystalline *hcp* for Co and determines the magnetic response according to the magnetocrystalline anisotropy: from effective longitudinal to transverse anisotropy, respectively.

For CoFeCu NWs, a main longitudinal magnetization configuration is found consistent with the predominant shape anisotropy. In addition, a weaker modulated contrast along the wires axis is observed that matches the position of each diameter modulation: vortex-like structures are observed at the ends of the wires and at the surface around the modulations.

The surface of NW consists of a sequence of segments with opposite XMCD contrast suggesting the presence of a vortex-like structure with alternating chirality. Along the length of the wire, the contrast in each segment of the shadow region vanishes only in about half of its area while the remaining shadow area shows a uniform XMCD contrast. This suggests a domain structure consisting of uniformly magnetized core surrounded by a shell of curling spins of opposite chiralities around the wire axis.

The contrast observed in the Fig. 18(a) is interpreted by the sketch in Fig.18(b). The bright/dark contrast on the right is related with the surface magnetization of the NW. However, owing to the cylindrical geometry of the

nanowire and the grazing angle of the X-ray with respect to the sample surface only a certain region of the NW surface (the bright contrast region) is directly exposed to the X-rays while the rest is only sensitive to the transmitted beam (the dark contrast region).

The second type of contrast is found in the shadow area due to the transmitted X-rays through the nanowire. A complex contrast profile is observed due to geometry of the NW, transmission of the X-rays and circular configuration of the magnetization. The XMCD contrast sequence across the wire and shadow for one of the sections explained in the sketch of Fig. 18(b) is illustrated also in Fig. 18(c) by means of profiles of the direct and XMCD images. Notice that the grey contrast in the middle of the shadow (corresponding to the core of the wire) can be an indication of the magnetization pointing perpendicular to the beam, i.e. along the nanowire axis. While a precise determination of the core and shell sizes in the nanowires is hard to quantify, the comparable widths of the dark and bright contrast regions in the shadow indicate a much reduced diameter of the core. This is consistent with a strong perpendicular anisotropy of the Co NW.

The magnetic configuration of individual cylindrical NWs with designed bamboo-like geometry has been determined. The combination of direct photoemission and transmission information from XMCD-PEEM allows resolving the surface and the internal magnetic structure of cylindrical nanowires in a single experiment, revealing the magnetic configuration from both the shell and the core. Two types of nanowires with periodically modulated diameter have been investigated. In CoFeCu, the magnetic configuration is dominated by shape anisotropy. The remanent configuration consists of a main longitudinal domain with vortex structures at the ends as well as around the diameter modulations. The magnetization reversal is expected to take place through the propagation of a vortex domain wall which in this case can be pinned at the position of certain modulations. Interestingly, Co NWs with nearly perpendicular magnetocrystalline anisotropy show a radically different configuration, characterized by a series of vortices with alternating chirality which appears not to be connected with the position of the modulations. A circular magnetic configuration and a longitudinal core with vanishing diameter are thus concluded.

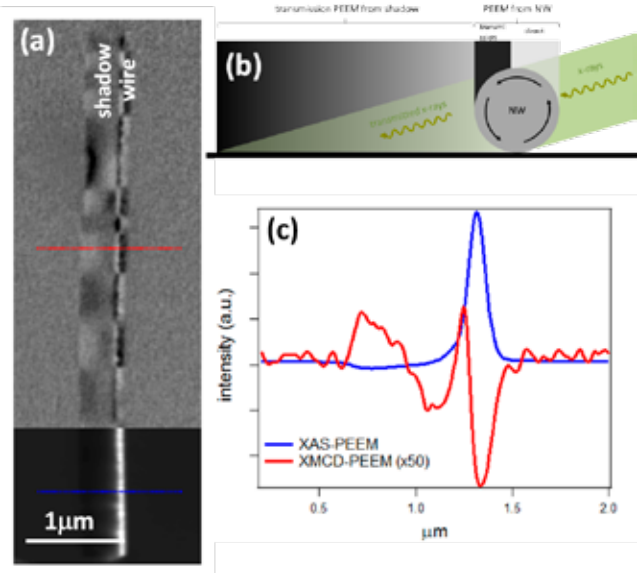

Figure 18: (a) Top: XMCD contrast of a representative individual Co nanowire measured at about 90° between the incident X-rays and the wire. Bottom: direct (XAS) image of a portion of the same wire. (b) Schematic view of the contrast observed for direct photoemission and transmission, dual in the case of a nanowire with circular spin configuration. (c) XAS and XMCD profiles of the nanowire presented in (a), at the positions marked by dashed horizontal lines.

OTHER REFERENCES

[1] Parkin S. S. P.; Hayashi M., and Thomas L. Magnetic Domain-Wall Racetrack Memory, *Science* **320:**190-194 (2008).

[2] Gao N.; Wang H.; and Yang E.-H. An Experimental Study on Ferromagnetic Nickel Nanowires Functionalized with Antibodies for Cell Separation *Nanotechnology* **21:**105107-105115 (2010).

[3] Lee D.J.; Kim E.; Kim D.; Park J. and Hong S. Nano-Storage Wires *ACS Nano* **7:**6906–6913 (2013).

AFFILIATION:

1. Institute of Materials Science of Madrid, CSIC, 28049 Madrid, Spain
2. ALBA Synchrotron, Barcelona, Spain
3. Departament de Física Fonamental and Institut de Nanociència i Nanotecnologia (IN2UB), Universitat de Barcelona, 08028 Barcelona, Spain

Molecular intercalation in FeSe affects the layer thickness to increase superconducting transition temperature

Temperature dependent local atomic displacements in ammonia intercalated iron selenide superconductor, *Scientific Reports* 6, 27646 (2016) doi: 10.1038/srep27646

E. Paris[1], L. Simonelli[2], T. Wakita[3], C. Marini[2], J.-H. Lee[3], W. Olszewski[2], K. Terashima[3], T. Kakuto[3], N. Nishimoto[3], T. Kimura[3], K. Kudo[3], T. Kambe[3], M. Nohara[3], T. Yokoya[3] and N. L. Saini[1*]

Iron-based superconductors are layered materials in which the structural architecture is known to have important role. Among these, the binary FeSe material is apparently the simplest system in which FeSe layers are stacked together without any spacer layer [1]. The superconducting transition temperature (T_c) of this binary FeSe is ~8 K, that can be raised up to ~15 K by anion substitution. The T_c of FeSe increases sharply to ~37 K under high pressure [2] that suggests possible manipulation of this simple structure to obtain much higher transition temperature. A promising way to increase the transition temperature is to introduce chemical pressure by intercalation between the stacked FeSe layers. Ammonia-thermal reaction was used for molecular intercalation in FeSe, resulting a new $Li_x(NH_3)_yFe_2Se_2$ superconductor with T_c~45 K [3]. With the aim to investigate the cause of such a high transition temperature in the new system it has been used X-ray absorption fine structure (EXAFS), an atomic specific site selective tool of the local structure. Purposefully, it has been used in-plane polarized synchrotron light to measure EXAFS signal on single crystal samples of $Li_x(NH_3)_yFe_2Se_2$ to determine local displacements as a function of temperature.

Single crystal samples of $Li_x(NH_3)_yFe_2Se_2$ were synthesized using liquid ammonia as a solvent. Several single crystals of FeSe and dopant metal in the appropriate ratio were placed in a glass tube filled with liquid NH_3 and sealed. After the intercalation reaction, the liquid NH_3 was removed by heating and dynamically pumping the glass tube, finally obtaining the single crystals of $Li_x(NH_3)_yFe_2Se_2$. Single crystals, well characterized for their structure and transport properties, were used to measure temperature dependent X-ray absorption spectra at the CLÆSS beamline. To avoid degradation, all the preparation procedures were performed in glove-box under Ar atmosphere before taking them to the measurement stage in He cryostat. Exfoliated crystals with desired thickness were used for Fe K-edge absorption experiments, carried out in the normal incidence geometry in which the polarization of the X-ray beam is parallel to the ab-plane of the single crystal samples.

The double peak structure between 1.5 and 3 Å, shown in Figure 19 (right), is due to Fe-Se bond distances (~2.4 Å) and Fe-Fe distances (~2.7 Å). The peaks appearing at longer distances are due to single scattering contributions of distant shells and multiple scatterings involving different bond distances. The FT magnitude shows clear evolution as a function of temperature with some apparent structural changes apart from the thermal damping.

The anion height (h_z) from the Fe-Fe layer and the associated bond angle (α) have been proposed to be the key parameters for superconductivity in iron-based materials [4]. Authors have determined these parameters from the measured Fe-Se and Fe-Fe distances from the EXAFS analysis assuming tetrahedral coordination of Se. Figure 20 (left) displays temperature dependence of h_z and α as a function of temperature. The h_z is found to be ~1.46 Å, that is lower than ~1.47 Å in FeSe (indicated in the Figure) [5,6]. Therefore, the intercalation of ammonia induces a compression of h_z. In addition, other local structure features suggest that the Fe-Fe layer in the intercalated system is flatter than the one in the binary FeSe.

The mean square relative displacements (MSRD) of the Fe-Se and Fe-Fe distances are shown in Fig. 20 (right). The temperature dependent MSRD can be described by the Einstein model with the model fits providing information on the Einstein temperatures of the related bond distances. The Einstein temperatures determined by this analysis, describing bond strength, are found to be ~313 K and ~248 K respectively for the Fe-Se and Fe-Fe distances. These values are similar to the known values for the two bonds in the binary FeSe [5,6], with Fe-Fe distance being relatively softer in the intercalated system. Therefore, local bond correlations in $Li_x(NH_3)yFe_2Se_2$ are very similar to those in binary FeSe while ammonia intercalation thins down and decouples the FeSe layers. Another important observation is the abrupt change in the MSRD across the transition temperature T_c. Such an anomalous change across T_c, known to occur also in other superconductors [7,8], suggests involvement of local lattice in the superconductivity of iron-based superconductors as well.

In conclusion, it has been studied the local structure of superconducting $Li_x(NH_3)yFe_2Se_2$ by means of in-plane polarized Fe K-edge EXAFS measurements on single crystal samples. It was found that the Se-height from the Fe-Fe layers suffers a clear shrinkage in the intercalated system with respect to the binary FeSe. On the other hand, the bond length characteristics hardly show any significant effect of intercalation except a small softening of Fe-Fe distance. It was also underlined local structure response of the superconductivity that is revealed by the anomalous change in the MSRD across the superconducting transition temperature. On the basis of these measurements authors have concluded that the high T_c of the ammonia intercalated system should be related with an effective compression of the FeSe-layers (with flatter Fe-Fe layer) and interlayer decoupling due to a thick spacer layer.

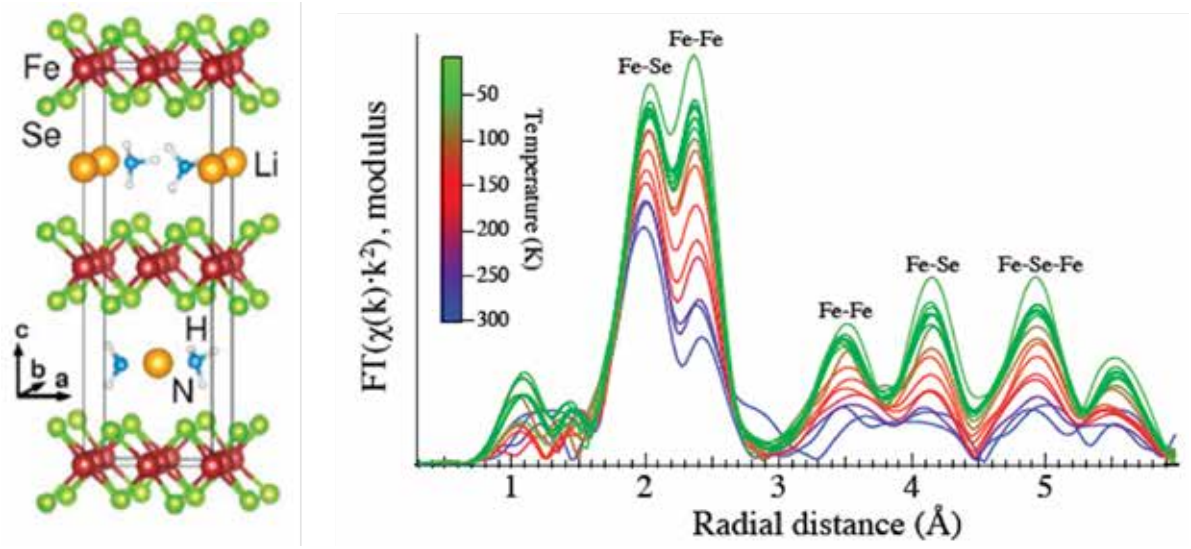

Figure 19: Unit cell of $Li_x(NH_3)yFe_2Se_2$ (left) and Fourier transforms (right) of Fe K-edge EXAFS oscillations measured at several temperatures.

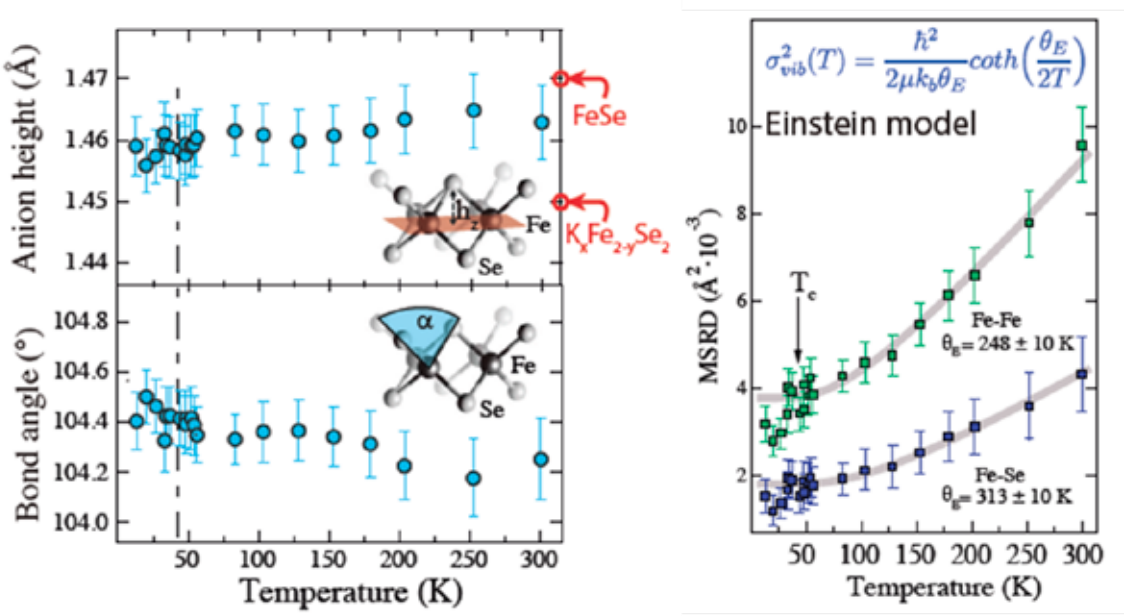

Figure 20: Anion height and bond angle (left) determined by EXAFS measurements on $Li_x(NH_3)yFe_2Se_2$ at several temperatures. Cartoons as insets define the two parameters. Mean square relative displacements (MSRD) for Fe-Se and Fe-Fe distances, measured by EXAFS analysis, are shown in the right panel.

OTHER REFERENCES

[1] Y. Mizuguchi and Y. Takano, *J. Phys. Soc. Jpn.* **79**, 102001 (2010).
[2] Y. Mizuguchi et al, *Appl. Phys. Lett.***93**, 152505 (2008).
[3] M. Burrard-Lucas et al, *Nat. Mat.***12**, 15 (2012).
[4] K. Kuroki et al, *Phys. Rev. B* **79**, 224511 (2009).
[5] B. Joseph et al, *Phys. Rev. B* **82**, 020502 (2010).
[6] A. Iadecola et al, *J. Phys.: Condens. Matter* **23**, 425701 (2011).
[7] N.L. Saini et al, *J. Phys. Soc. Jpn.***70**, 2092 (2001).
[8] N.L. Saini et al, *Phys. Rev. B* **68**, 104507 (2003).

ACKNOWLEDGEMENTS

This research was partially supported by the Program for Promoting the Enhancement of Research University from MEXT and the Program for Advancing Strategic International Networks to Accelerate the Circulation of Talented Researchers from JSPS. The work at Sapienza is partially supported by the PRIN2012 (grant number 2012X3YFZ2) of MIUR, Italy.

AFFILIATION:
1. Sapienza University of Rome, Rome, Italy;
2. ALBA Synchrotron, Cerdanyola del Vallès, Spain;
3. Okayama University, Okayama, Japan

SCIENTIFIC RESULTS

MATERIALS SCIENCE

Structural evolution on a new family of perovskites with double double cation order: $MnRMnSbO_6$

Double Double Cation Order in the High Pressure Perovskites $MnRMnSbO_6$.
***Angewandte Chemie - Inernational Edition* 55 (32), 9340–9344 (2016) doi: 10.1103/PhysRevB.93.054102**

E. Solana-Madruga[1], Á.M. Arévalo-López[2], A.J. Dos santos-García[3], R. Sáez-Puche[1], J.P. Attfield[2]

Among the compounds most studied in solid state chemistry are those crystallizing with the ABO_3 perovskite structure. It can be described as a 3D network of corner-sharing BO_6 octahedra where the A cation is enclosed by a cage formed by eight BO_6 octahedra. The interest in these compounds arises from the wide variety of properties exhibited and the easiness to accommodate the vast majority of the chemical elements of the periodic system. The insertion of different cations leads to $AA'B_2O_6$ and $A_2BB'O_6$ compositional derivatives commonly known as double perovskites (DPv), with A-site and B-site cation order respectively [1-3].

The use of high pressure and high temperature synthesis conditions (HPHT) allows access to metastable compounds. Among them, perovskites containing the small Mn^{2+} cation into the highly coordinated A site in combination with other transition metals into the B sites yields interesting magnetic properties, for instance the magnetoresistant Mn_2FeReO_6 [4], and exotic spin arrangements as the incommensurate helical magnetic structure of Mn_2FeSbO_6 [5].

Herein, authors report on a series of new perovskite derivative that combines a simultaneous ordering into both the A and B sites of an $AA'BB'O_6$ double double perovskite (DDPv). Mn^{2+} is hosted in both cationic sublattices and is ordered in a rock salt configuration with Sb^{5+} at the B sites but in a columnar fashion with R^{3+} (R = La-Sm) at A positions, giving the $MnRMnSbO_6$ stoichiometry. The columnar ordering is vanished for $R^{3+} \leq$ Eu, leaving place to conventional DPv. Thus, an "order to disorder" phase transition occurs through the lanthanide series governed by the size mismatch among R^{3+} and Mn^{2+} cations [6].

The structural characterization of the $MnRMnSbO_6$ family of oxides through the use of X-ray diffraction under synchrotron radiation was carried out at the MSPD beamline of ALBA Synchrotron using the high resolution endstation. SXRD patterns of the R = La - Gd containing samples were collected at room temperature conditions at $\lambda = 0.44214$ Å wavelength in the angular range $0.021^\circ < 2\theta < 44.001^\circ$ with a step width of 0.003°.

The obtained diffraction patterns for $MnEuMnSbO_6$ and $MnGdMnSbO_6$ oxides correspond to that observed for other DPv. The $(011)_{DPv}$ and $(101)_{DPv}$ reflections (d ~4.6 Å) evidence the rock-salt order of Mn^{2+} and Sb^{5+} at the B sites. Otherwise, Mn^{2+} and R^{3+} cations are disordered over the A site of the perovskite structure. The diffraction patterns of these compounds were nicely refined with $P2_1/n$ symmetry and $\sqrt{2}a_p * \sqrt{2}a_p * 2a_p$ cell parameters.

On the other hand, an additional superstructure peak was observed in the case of $MnRMnSbO_6$ oxides with R= La - Sm at d ~ 5.5 Å. The Rietveld refinement of these

patterns to a tetragonal symmetry in the $P4_2/n$ space group and cell parameters $2a_p * 2a_p * 2a_p$ revealed the combination of the rock-salt order of Mn^{2+} and Sb^{5+} at the B sites concomitantly with an unusual columnar arrangement of Mn^{2+} and R^{3+} cations at the A site. The columnar arrangement is confirmed by the presence of $(110)_{DDPv}$ peak in the diffraction patterns and $(111)_{DDPv}$ reflection stands for the rock-salt configuration of the B sites. Figure 21 shows the crystal structure of the DDPv compound.

The decrease of the lattice parameters and the structural details, as metal-oxygen distances and angles, show a progressive evolution in agreement with the lanthanide contraction. The evolution of the octahedral tilt angle of these DPv and DDPv structures has been considered as order parameter of the phase transition between both polymorphs. The double-double ordered modification has an $a^+a^+c^-$ tilt system that transforms to the $a^-a^-c^+$ for the double monoclinic polymorphs.

Two different perovskite derivatives have been determined for the $MnRMnSbO_6$ series as a function of the ionic radii of the rare earth. The compounds including the smallest R^{3+} cations used in this study crystallize with a conventional DPv structure, where the B-site cations (Mn^{2+} and Sb^{5+}) are ordered with a rock-salt motif. The introduction of larger rare earths induces an additional columnar order among Mn^{2+} and R^{3+} in the A sites, which combination with the rock-salt B-site order originates a new type of DDPv structure, never reported in the literature up to date. This new structure is notable for having five different cation sites (see Figure 21), three of them occupied by Mn^{2+} in different coordination environments: tetrahedral, square planar and octahedral. The phase transition from DDPv to DPv has been monitored by using the octahedral tilt angle as order parameter.

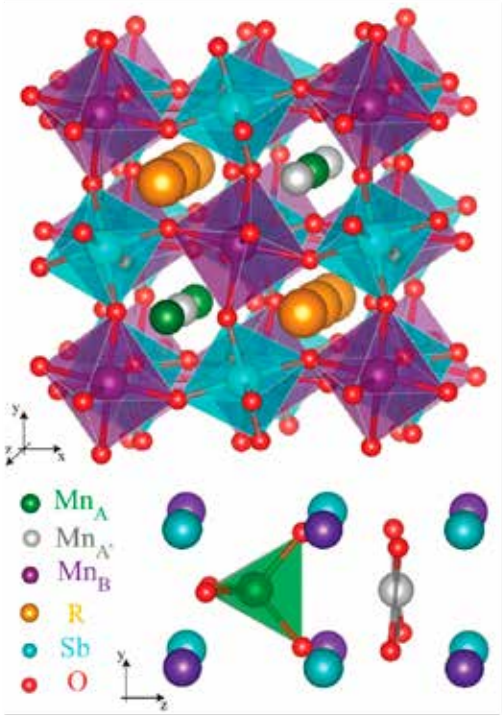

Figure 21: Structural model determined for the DDPv polymorph of $MnRMnSbO_6$ (R = La-Sm) compounds from the Rietveld refinement of their XRD patterns collected under synchrotron radiation.

ACKNOWLEDGEMENTS

Authors acknowledge Comunidad de Madrid and MINECO for funding through projects S-2013/MIT-2753 and MAT2013-44964-R respectively. They are also indebted to EPSRC and the Royal Society for support. ALBA Synchrotron is acknowledged for the beamtime and Dr. O. Vallcorba and Dr. C. Popescu for the assistance during the experiment.

OTHER REFERENCES

[1] M. Anderson, K. Greenwood, G. Taylor, and K. Poeppelmeier, "B-cation arrangements in double perovskites," *Prog. Solid State Chem.*, vol. **22**, no. 3, pp. 197–233, (1993).

[2] G. King and P. M. Woodward, "Cation ordering in perovskites," *J. Mater. Chem.*, vol. **20**, no. 28, p. 5785, (2010).

[3] S. Vasala and M. Karppinen, "$A_2B'B''O_6$ perovskites: A review," *Prog. Solid State Chem.*, vol. **43**, no. 1–2, pp. 1–36, (2015).

[4] A. M. Arévalo-López, G. M. McNally, and J. P. Attfield, "Large Magnetization and Frustration Switching of Magnetoresistance in the Double-Perovskite Ferrimagnet Mn_2FeReO_6," *Angew. Chemie Int. Ed.*, vol. **54**, no. 41, pp. 12074–12077, (2015).

[5] A. J. Dos santos-García, C. Ritter, E. Solana-Madruga, and R. Sáez-Puche, "Magnetic and crystal structure determination of Mn_2FeSbO_6 double perovskite," *J. Phys. Condens. Matter*, vol. **25**, no. 20, p. 206004, (2013).

[6] E. Solana-Madruga *et al.*, "Double Double Cation Order in the High-Pressure Perovskites $MnRMnSbO_6$," *Angew. Chemie - Int. Ed.*, vol. **55**, no. 32, pp. 9340–9344, (2016).

AFFILIATION:

1. Dpto. Química Inorgánica I, Facultad de Ciencias Químicas, Universidad Complutense de Madrid. Avda. Complutense sn. 28034, Madrid, Spain.
2. Centre for Science at Extreme Conditions (CSEC) and School of Chemistry, University of Edinburgh. Mayfield Road, Edinburgh. EH9 3JZ, U.K.
3. Dpto. Ingeniería mecánica, química y diseño industrial, ETSIDI, Universidad Politécnica de Madrid. C/ Ronda de Valencia, 3. 28012, Madrid, Spain.

First evidence of helium-based compound at low pressures

Ordered helium trapping and bonding in compressed arsenolite: Synthesis of As_4O_6·2He.
***Physical Review B* 93, 054102 (2016) doi: 10.1103/PhysRevB.93.054102**

Juan Ángel Sans,[1*] Francisco Javier Manjón,[1] Catalin Popescu,[2] Vanesa Paula Cuenca-Gotor,[1] Oscar Gomis,[3] Alfonso Muñoz,[4] Plácida Rodríguez-Hernández,[4] Julia Contreras-García,[5] Julio Pellicer-Porres,[6] Andre Luis de Jesus Pereira,[7] David Santamaría-Pérez,[6] and Alfredo Segura[6]

At ambient conditions, helium is considered one of the most inert elements in nature and its reaction is a challenge in the physical-chemical field [1]. The study of the new chemistry under extreme conditions of pressure offers an invaluable opportunity of exploring a route with the aim of synthesizing new compounds with outstanding properties [2]. In that sense, mixtures of helium with other noble gases at very high pressure have led to the formation of new solid van der Waals compounds with exotic stoichiometries ($He(N_2)_{11}$, $Ne(He)_2$) [3,4]. However, the reaction of helium with a solid compound remains unexplored. In this context, authors have proposed the study of the interaction of helium with molecular solids under compression. These solids are open framework structures composed of molecular units, exhibiting strong covalent interatomic forces, which are linked by weak intermolecular forces. The application of pressure allows tuning interatomic distances and consequently is a powerful tool to study atomic interactions; hence, the possibility of trapping small atoms or molecules in the empty cavities amongst the molecular solids which eventually could react with the host structure. In this work, it is provided experimental and theoretical proofs of the pressure-induced trapping of helium in a molecular solid (As_4O_6 also known by its mineral name, arsenolite) and the reactivity of helium with this compound at relatively low pressures.

As_4O_6 has been studied under compression using different pressure-transmitting media (PTM), like silicone oil, 4:1 methanol-ethanol mixture and He and also without any PTM. For this purpose, two experimental techniques have been combined (synchrotron-based angle dispersive X-ray diffraction (XRD) and Raman scattering) and *state-of-the-art ab-initio* calculations, which will provide information about the structural, elastic, electronic and lattice dynamical properties of As_4O_6 and As_4O_6·2He at different pressures.

XRD experiments were performed at MSPD beamline in the ALBA Synchrotron and allowed authors to study the evolution of the structural properties of As_4O_6 under compression. These measurements revealed an abrupt increase of the volume above 3 GPa when helium was used as PTM, which result was not observed when As_4O_6 is compressed with other PTM or without any PTM. These results could be explained if one assumes that helium enters into one or several of the three kinds of empty sites (8a, 16c and 16d sites) of As_4O_6 and is trapped in those voids. The *ab-initio* theoretical simulations showed a nice agreement with results obtained for non-penetrating PTM in pure As_4O_6; however, the theoretical simulations evidenced that the behavior of As_4O_6 compressed with helium could only be explained if helium was trapped specifically at the voids located at 16d Wyckoff crystallographic sites, and not on 8a or 16c sites which should remain empty. Raman scattering measurements of As_4O_6 under compression corroborated these findings [5]. It was found that most of the Raman-active modes underwent a slight shift in frequency above 3 GPa when As_4O_6 is compressed with helium, which was

not observed with other PTM or without any PTM. Again, authors obtained a good agreement between the experimental and theoretical evolution of the experimental Raman-active modes of As_4O_6 under compression in non-penetrating and helium environment, thus giving support to the entry and trapping of helium in arsenolite.

A pressure-induced amorphization occurs in pure As_4O_6 above 15 GPa; however, this behavior was not observed in the case of compression with helium even up to 30 GPa. This finding is in good agreement with the theoretical simulations that predicted a mechanical instability of pure As_4O_6 close to 15 GPa and no mechanical instability when helium is introduced at 16d Wyckoff sites of As_4O_6 even above 30 GPa. This result led authors to conclude that pressure-induced helium trapping could imply something much more important than a simple trapping of helium that was merely perturbing the compression of the host structure. Thus, they decided to explore how the theoretical charge density of both pure arsenolite and arsenolite with helium at 16d sites behave at different pressures. In particular, they paid special attention to the interactions between helium and surrounding atoms. For that purpose, they used the Non-Covalent Interaction (NCI) index which is better adapted for identifying weak non-covalent bonds than the electron localization function (ELF). Their study revealed that localized interactions appear between helium and six arsenic neighbors. These interactions are strong enough (similar in force to hydrogen-type bonding in water) to claim that helium plays a key role in the structure; i.e., these interactions evidence the reaction of helium and arsenolite at pressures above 3 GPa leading to a new compound with stoichiometry $As_4O_6{\cdot}2He$. This finding paves the way for searching new helium-based stable compounds, like in the recent work about the formation of a helium and sodium material [6] suggested at much higher pressures than the one reported in this work (113 GPa vs 3 GPa).

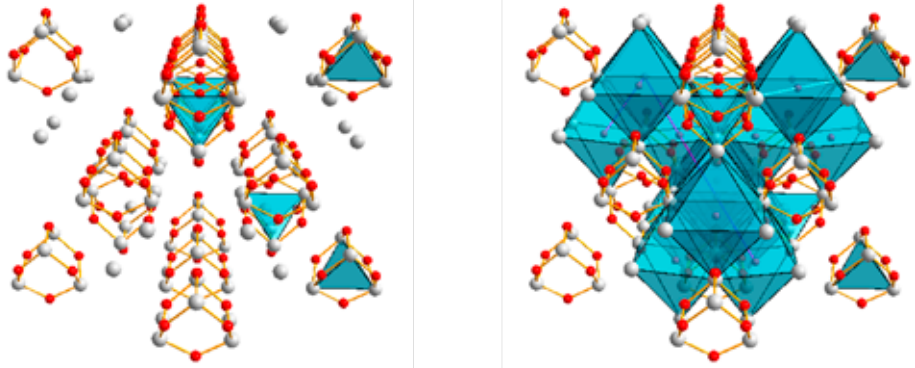

Figure 22: Representation of structure of pure As_4O_6 (left) and $As_4O_6{\cdot}2He$ (right).

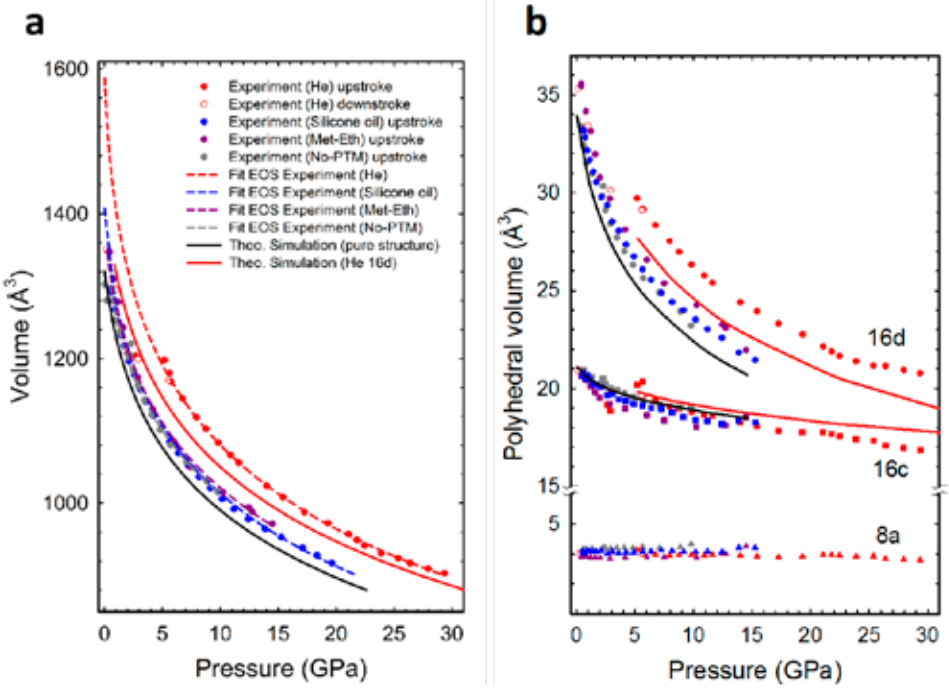

Figure 23: (a) Equation of state of compressed As_4O_6 under different pressure transmitting media. (b) Behavior of polyhedral unit volumes around original empty Wyckoff sites of As_4O_6 when compressed with different PTM. Symbols are used for experimental data and solid lines to theoretical calculations (black for pure As_4O_6 and red for $As_4O_6{\cdot}2He$).

In summary, authors have proved experimental and theoretically that helium incorporates above 3 GPa into the arsenolite lattice at ordered 16d positions. Calculations indicate that pressure-induced helium trapping in As_4O_6 modifies all the properties of arsenolite due to the new established kind of hydrogen-type bonds with arsenic atoms of As_4O_6 at relatively low pressures (3 GPa). The interaction of helium and arsenic atoms results in the formation of a new compound with As_4O_6·2He stoichiometry (only stable above 3 GPa since He exits the arsenolite structure below this pressure) with different properties from the host As_4O_6 compound. This discovery paves the way to explore the formation of new compounds by pressure-induced trapping and bonding of gases, small atomic and molecular species in molecular solids having open-framework structures, like those featuring active lone electron pairs. Moreover, these results suggest that compression of molecular solids with noble gases, like helium, must be performed with caution since they may result in unexpected results compared to other PTM due to entry (and possible reaction) of these gases with their hosts.

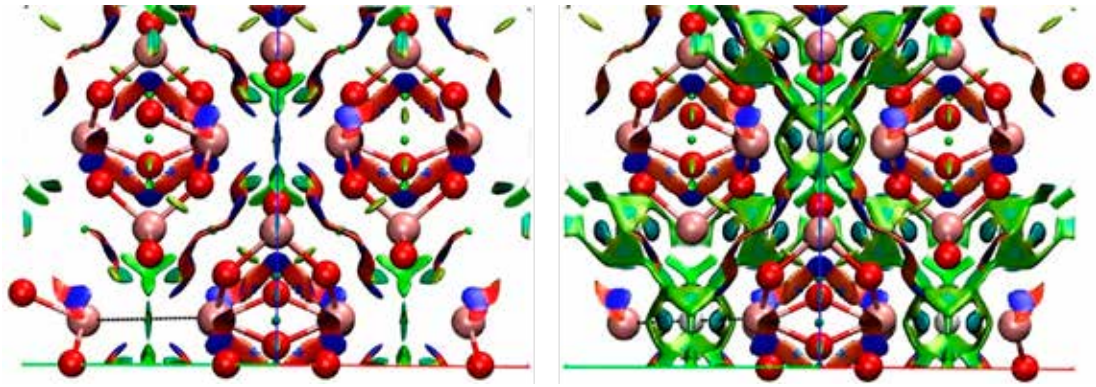

Figure 24: Isosurfaces of the reduced density gradient (revealed by NCI index) evidencing non-covalent interactions in As_4O_6 (left) and As_4O_6·2He (right) near 16 GPa. As expected for a noble gas, van der Waals (green) interactions around the He atoms are revealed. However, unexpectedly localized interactions (in turquoise blue) also make their appearance along the He-As interaction lines.

ACKNOWLEDGEMENTS

Authors thank financial support from the Spanish Consolider Ingenio 2010 Program (Project No. CSD2007-00045) and MAT2015-71070-REDC. The work was also supported by Spanish MICCIN under projects MAT2014-46649-C4-1/2/3-P and from Vicerrectorado de Investigación de la Universitat Politècnica de València under projects SP20140701 and SP20140871. Supercomputer time has been provided by the Red Española de Supercomputación (RES) and the MALTA cluster. J. A. S. acknowledges Juan de la Cierva and Ramón y Cajal fellowship program for his financial support. A. M. and P. R.-H. acknowledge S. Muñoz Rodríguez for providing us with a data parsing application. A.L.J.P. acknowledges financial support through Brazilian CNPq (Project Nº 201050/2012-9). D. S.-P acknowledges Ramón y Cajal fellowship program for his financial support.

OTHER REFERENCES

[1] W. E. Snyder, R. R. Bottoms. *Ind. Eng. Chem.*, **22**, 1189 (1930).

[2] P.F. McMillan. *Chem. Soc. Rev.* **35**, 855 (2006).

[3] W. L. Vos, L. W. Finger, R. J. Hemley, J. Z. Hu, H. K. Mao, J. A. Schouten. *Nature* **358**, 46 (1992).

[4] P. Loubeyre, M. Jean-Louis, R. LeToullec, L. Charon-Gerard. *Phys. Rev. Lett.* **70**, 178 (1993).

[5] V. P. Cuenca-Gotor, O. Gomis, J. A. Sans, F. J. Manjon, P. Rodriguez-Hernandez, A. Muñoz. *J. of Appl. Phys.* **120**, 155901 (2016).

[6] X. Dong, A. R. Oganov, A. F. Goncharov, E. Stavrou, S. Lobanov, G. Saleh, G.-R. Qian, Q. Zhu, C. Gatti, V. L. Deringer, R. Dronskowski, X.-F. Zhou, V. B. Prakapenka, Z. Konôpková, I. A. Popov, A. I. Boldyrev, H.-T. Wang. *Nature Chemistry* , (2017).

AFFILIATION:

1. Instituto de Diseño para la Fabricación y Producción Automatizada, Universitat Politècnica de València, 46022, Valencia, Spain.
2. ALBA Synchrotron, 08290, Cerdanyola, Spain.
3. Centro de Tecnologías Físicas, MALTA Consolider Team, Universitat Politècnica de València, 46022, València, Spain.
4. Departamento de Física, Instituto de Materiales y Nanotecnología, Universidad de La Laguna, 38205, La Laguna, Spain.
5. Laboratoire de Chimie Théorique, Université Pierre et Marie Curie, F-75005 Paris, France.
6. ICMUV-Departamento de Física Aplicada, Universitat de València, 46100, Burjassot, Spain.
7. Laboratòrio de Materiais Cerâmicos Avançados, Faculdade de Ciências Exatas e Tecnologia, Universidade Federal da Grande Dourados, Dourados, Brazil.

Combined SAXS/WAXS analysis of glucomannan-chitosan interpenetrating hydrocolloid networks (IHNs)

Development of glucomannan-chitosan interpenetrating hydrocolloid networks (IHNs) as a tool for creating satiating ingredients. *Food Hydrocolloids* 60 533-542 (2016) doi: 10.1016/j.foodhyd.2016.04.033

Amparo Lopez-Rubio[1], Paula Tarancón[1], Laura G. Gómez-Mascaraque[1], Marta Martínez-Sanz[1], Maria Jose Fabra[1], Juan Carlos Martínez[2], Susana Fiszman[1]

The development of the so-called satiating foods (those with an increased capacity to inhibit appetite in the period after consumption) has attracted a great interest from researchers and the food industry. Currently, the only food ingredient having a positive opinion from the European Food Safety Authority (EFSA) for weight management is konjac glucomannan (KGM) [1], the main polysaccharide from the tubers of the *Amorphophallus konjac* plant. However, the extraordinarily high water-holding capacity of this carbohydrate precludes its direct addition to food products. In this work, as a strategy for creating satiating ingredients, pH-sensitive glucomannan-chitosan formulations were developed. The swelling behavior of the different biopolymer blends was characterized by combined SAXS/WAXS experiments and correlated with the molecular interactions taking place and the corresponding behavior at neutral and acidic conditions.

KGM is a soluble polysaccharide consisting on β-(1→4)-linked D-mannose and D-glucose units in a ratio of 8:5 and having a small degree of branching. Its extraordinary water-holding capacity makes KGM to swell in the stomach, providing satiety sensation and being highly effective in obesity treatment [2]. However, its high viscosity precludes direct addition to most foods, remaining a technological problem for the food industry. Chitosan is a cationic polysaccharide composed of randomly distributed β-(1-4)-linked D-glucosamine (deacetylated unit) and N-acetyl-D-glucosamine (acetylated unit). It is a pH-sensitive biopolymer as in acidic aqueous conditions the polymer chains are positively charged, causing repulsions and swelling, while increasing the pH causes the functional groups to lose their charge and the material collapses back. Moreover, at basic conditions, the acetyl groups of KGM are cleaved, resulting in network formation through hydrogen bonding.

The aim of the present work was to understand the interactions taking place between KGM and chitosan, focusing on how chitosan molecular weight (Mw), hydrocolloid ratio and neutralization with a salt affected the formation of interpenetrating hydrocolloid networks (IHNs) and their subsequent swelling behavior in neutral and acid conditions.

SAXS and WAXS measurements were carried out to study the water sorption ability of various blend compositions. The intensity of the scattering curves varied as a function of composition and chitosan Mw (Figure 25). This variation could be explained on the basis of the SLD contrast originated between the different components (SAXS) and to the strongly bound water (WAXS).

In the case of SAXS, as water was sorbed, the SLD contrast would lower and, thus, the scattering intensity was expected to decrease to a greater extent for those samples with higher swelling capacity. While only strong KGM-chitosan interactions were established when blending low contents of KGM with low Mw chitosan, for the high Mw blends the intensity was hardly affected by the KGM concentration. This was explained by a stronger chitosan network in this case, held by intra-chain hydrogen bonds, which reduced the susceptibility

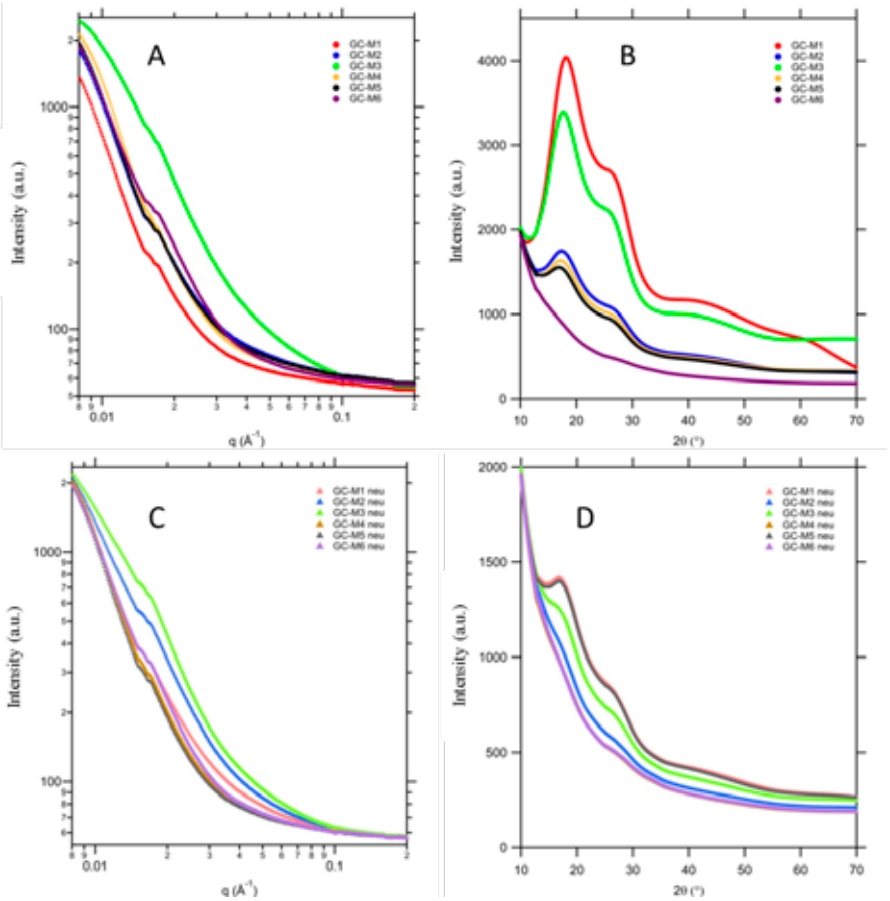

Figure 25: SAXS (A and C) and WAXS (B and D) measurements from KGM: Low Mw chitosan 90:10 (M1), 75:25 (M2) and 50:50 (M3) blends and KGM: High Mw chitosan 90:10 (M4), 75:25 (M5) and 50:50 (M6) blends soaked in water, non-neutralized (A, B) or neutralized (C, D). Wavelength (λ) = 1Å.

of the blends to swelling, regardless of the KGM content. Neutralization reduced the difference in the swelling degree of the different samples, explained by a strengthening of the chitosan network. The WAXS patterns of the water-soaked blends were dominated by the appearance of strong shoulders located at ca. 27.8° and 40.8°, which have been assigned to the arrangement of water molecules bound to the surface of biopolymers [3]. The intensity of these scattering features increased when increasing the KGM content in the blends and was greater for the low Mw chitosan samples. The neutralization process led to a significant decrease in the intensity of the water scattering shoulders, explained by the reduced capacity of deprotonated chitosan molecular chains to interact with water molecules.

Combined SAXS and WAXS studies showed that the water swelling capacity of KGM-chitosan blends was directly related to the amount of labile hydroxyl groups present, which was influenced by the chitosan Mw, blend composition and neutralization of the systems. While for low Mw chitosan, only the blends with lower KGM contents showed decreased water swelling capacity, strong interactions due to the formation of interpenetrating hydrocolloid networks (IHNs) were observed for the blends of KGM-high Mw chitosan. Neutralization with a salt promoted the strengthening of the chitosan network in the blends and, thus, was key for determining the pH dependent behavior of the blends.

ACKNOWLEDGEMENTS

Synchrotron experiments were performed at NCD beamline at ALBA Synchrotron with the collaboration of ALBA staff. Laura G. Gómez-Mascaraque is recipient of a predoctoral contract from the Spanish Ministry of Economy, Industry and Competitiveness, Call 2013. M. Martínez Sanz and M. J. Fabra are recipients of a Juan de la Cierva and Ramon y Cajal contracts from the Spanish Ministry of Economy, Industry and Competitiveness, respectively. Authors are also grateful to the Spanish Ministry of Economy, Industry and Competitiveness for financial support (AGL2015-63855-C2-1).

OTHER REFERENCES

[1] EFSA. Scientific Opinion on the substantiation of health claims related to konjac mannan (glucomannan) (ID 854, 1556, 3725, 1559, 835, 3724, 3217, 3100, 3217, 834, 1557, 3901, 1558) pursuant to Article 13(1) of Regulation (EC) No 1924/2006. *EFSA Journal*, **8**(10), 1798 (2010).

[2] Walsh, D. E., Yaghoubian, V., & Behforooz, A. Effect of glucomannan on obese patients: a clinical study. *International Journal of Obesity*, **8**, 289-293 (1984).

[3] Martínez-Sanz, M., Mikkelsen, D., Flanagan, B., Gidley, M. J., & Gilbert, E. P. Multi-scale model for the hierarchical architecture of native cellulose hydrogels. *Carbohydrate Polymers*, **147**, 542-555 (2016).

AFFILIATION:

1. Institute of Agrochemistry and Food Technology (IATA-CSIC), Avda. Agustin Escardino 7, 46980 Paterna, Valencia, Spain
2. ALBA Synchrotron, Carrer de la Llum 2-26, 08290, Cerdanyola del Vallès, Barcelona, Spain

Light-Responsive Self Assembled Materials by Supramolecular Post-Functionalization via Hydrogen Bonding of Amphiphilic Block Copolymers

Macromolecules **49,** 7825–7836 (2016) doi: 10.1021/acs.macromol.6b01112

Alberto Concellón[1], Eva Blasco[2], Alfonso Martínez-Felipe[3], Juan Carlos Martínez[4], Igor Šics[4], Tiberio A. Ezquerra[5*], Aurora Nogales[5], Milagros Piñol[1], and Luis Oriol[1]

The design of efficient drug delivery vehicles remains a true challenge in polymer and materials science. A variety of polymeric nanocarriers have been described in recent years based on the ability of amphiphilic block copolymers (BCs) to spontaneously generate assemblies in water, such as micelles or vesicles, whose size and morphology are highly dependent on the composition, molecular geometry, and relative block lengths of the BCs. The incorporation of pH-, temperature or light-responsive moieties into these amphiphilic BCs makes them potential candidates as systems for controlled release. The use of light as an external stimulus is particularly advantageous as provides with temporal and spatial control in the material response. A new class of light-responsive supramolecular amphiphilic block copolymers (BCs) based on the association through multiple H-bonding between 4-isobutyloxyazobenzene motifs and 2,6-diacylaminepyridine units is reported.

The structural and thermal characterization of these supramolecular azo-copolymers in bulk and solution is presented. The work emphasizes the self-assembly of these supramolecular polymers in water and the study of their UV-light responsive properties by UV–vis spectroscopy, dynamic light scattering (DLS), transmission electron microscopy (TEM), and synchrotron small-angle X-ray (SAXS), see Figure 26.

The supramolecular self-assemblies, micelles and vesicles, are distorted under UV-illumination which makes feasible their use as light triggered nanocarriers. Therefore, it can be concluded that hydrogen bonding is an effective and flexible strategy to obtain stimuli responsive assemblies by avoiding the time-consuming procedures associated with the preparation of covalent amphiphilic block copolymers.

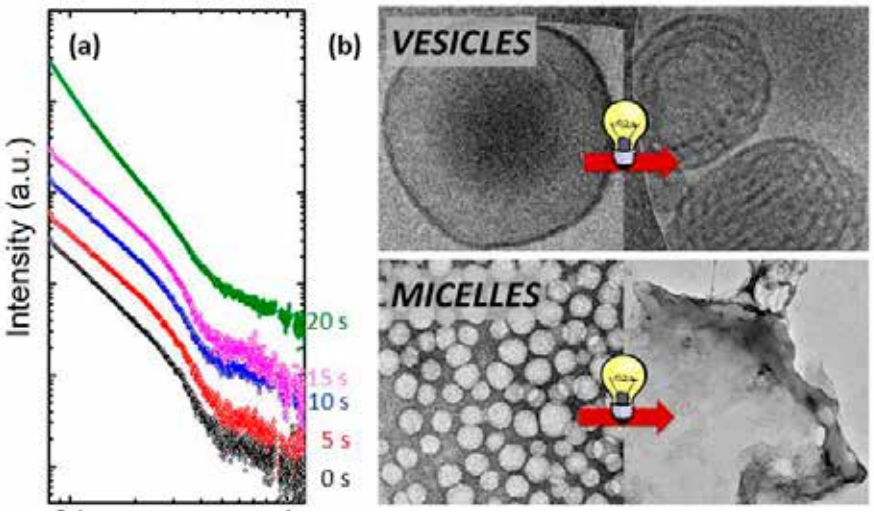

Figure 26: (a) SAXS evolution upon illumination of a photosensitive block copolymer. (b) Crio-TEM of different block copolymers before and after illumination.

ACKNOWLEDGEMENTS

This work was supported by the MINECO, Spain, (MAT2014-59187-R and MAT2014-55205-P, FEDER funding, and Aragon Government. A.C. acknowledges MINECO for his Ph.D. grant. A.M.-F. expresses thanks for the financial support of the Generalitat Valenciana for his APOSTD/2013/054 grant.

OTHER REFERENCES

[1] García-Juan H, Nogales A, Blasco E, Martínez JC, Šics I, Ezquerra TA, Piñol M, Oriol L. *European Polymer Journal* **81**, 621 (2016).

AFFILIATION:

1. Departamento de Química Orgánica, Instituto de Ciencia de Materiales de Aragón (ICMA)-Facultad de Ciencias, Universidad de Zaragoza-CSIC, 50009, Zaragoza, Spain
2. Preparative Macromolecular Chemistry, Institut für Technische Chemie und Polymerchemie, Karlsruhe Institute of Technology(KIT), Engesserstrasse 18, 76128 Karlsruhe, Germany
3. Chemical and Materials Engineering Group, School of Engineering, University of Aberdeen. King's College, Aberdeen AB24 3UE, UK.
4. ALBA Synchrotron, 08290 Cerdanyola del Valles, Barcelona, Spain
5. Instituto de Estructura de la Materia, IEM-CSIC, C/Serrano 121, 28006 Madrid, Spain

SCIENTIFIC RESULTS

ENERGY RELATED MATERIALS

Chemical and electrochemical characterization of Nafion containing silver nanoparticles in a stripe-like distribution

RSC Advances **6**:9923-9931(2016)

B. Domènech[1], V. Romero[2], M.I. Vázquez[2], M. Avila[3*], J. Benavente[2], M. Muñoz[4] and J. Macanás[5*]

The particular chemical structure of Nafion, with nanostructured and segregated hydrophilic and hydrophobic domains, enables its use as a model structure for the manufacture of polymer–metal nanocomposites thanks to its exceptional properties (i.e. high cation transport and chemical stability).

Among such nanocomposites, samples of Nafion-117 containing Ag-NPs of ca. 10 nm prepared by Intermatrix Synthesis exhibited a particular distribution in the form of stripes, a regular pattern that could reveal the real morphology of the polymer.

The aim of this work was to analyse the potential application of this material for example in electrochemical devices. For this purpose, several microscopic, chemical, electrochemical and mechanical techniques of characterization were used including some based in X-rays: X-Ray Powder Diffraction (XRD), X-Ray Photoelectron Spectroscopy (XPS and X-Ray Absorption Near Edge Spectroscopy (XANES) at the ALBA Synchrotron. Thanks to the combination of the information obtained by complimentary techniques, the characterization of this new material was assessed and, under such view, the morphological, physicochemical and electrochemical differences between Nafion-117 and Nafion-117/Ag-NP samples were evaluated.

XANES technique was particularly useful since it enabled to obtain a more specific analysis and ensured the chemical composition of nanoparticles inside Nafion-117 by comparing the spectra of samples with the spectra of pure standards, concretely, metallic silver foil (Ag^0) and solid inorganic salts such as Ag_2O and $AgNO_3$. XANES analyses, data treatment and curve deconvolution were carried out (Fig. 27). For all the cases, excepting for specimen labelled as N2, the most of the silver in the samples was found in the form of metallic zero-valent silver (Ag^0) although different proportions of oxidized silver were also detected. For the other nanocomposites (N2, N3, N4), the percentage of unreduced $AgNO_3$ was marginal compared to metallic silver, so it would not have been detected by XRD either due its low amount or because it was not crystalline.

The presence of silver was confirmed by the analysis of a digested sample by Inductively Coupled Plasma Mass Spectrometry (ICP-MS) that determined that the content of silver was ca. 5% weight of dry sample.

Regarding the crucial topic of the metal oxidation state, XRD was only able to ascertain the existence of Ag^0 nanocrystals whereas the combination of XPS

technique and XANES identified both Ag^0 and Ag^+ species, being the last species located on the very surface and easily removed when Ar etching was applied. Moreover, synchrotron experiments proved the existence of different types of oxidized silver, being the sample aged by sonication the one with a lower amount of zero-valent silver (Ag^0 ca. 68%), but also revealing that some Ag_2O (4–8%) was present even in samples only loaded with $AgNO_3$ and not chemically reduced. Taking into account both characterizations, it is expected that oxidized Ag-NPs were located only on the very surface due to the effect of atmospheric oxygen.

Overall, the results indicate that the developed material may be as suitable as Nafion to be used in electrochemical devices such Proton Exchange Membranes (PEMs) although the existence of Ag-NPs could be advantageous for other devices such as sensors, either electrochemical or based in surface enhanced Raman scattering (SERS), where the properties of Ag-NPs might increase the response signal or reduce the response time.

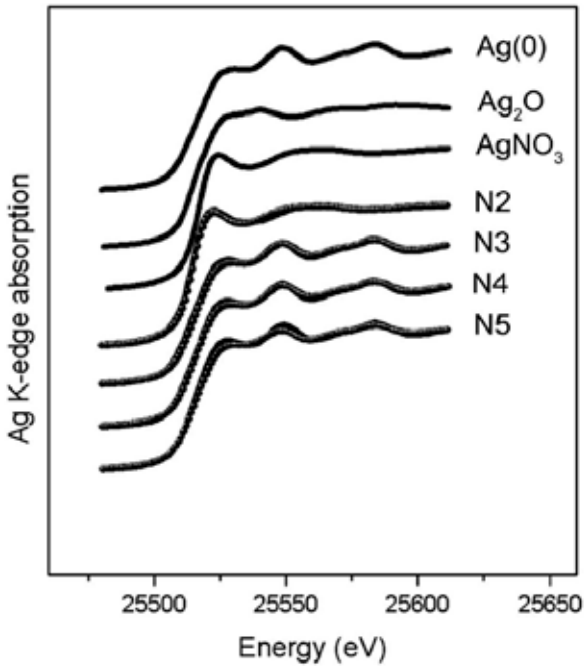

Figure 27: Normalized Ag K-edge XANES spectra for samples N2–N5 (straight line) and the corresponding fit (spheres). References used for the linear combination (Ag foil, Ag_2O and $AgNO_3$) are shown above.

ACKNOWLEDGEMENTS

Authors thank to the CICYT (MINECO, Spain, project CTQ/2011- 27770 FEDER funds) for financial support and Ing.M.V.Martinez de Yuso, Servicios Generales de Investigación de la Universidad de Málaga (XPS Laboratory). Many thanks are given to Servei de Microscòpia from Universitat Autònoma de Barcelona. Wojciech Olszewski and Carlo Marini are acknowledged for their help during the data acquisition at CLAESS beamline from ALBA synchrotron light source and in the XANES data treatment.

OTHER REFERENCES

[1] Hierro A, Gershlick DC, Rojas AL, Bonifacino JS. Formation of Tubulovesicular Carriers from Endosomes and Their Fusion to the trans-Golgi Network. *Int Rev Cell Mol Biol.* **318**:159-202 (2015).

AFFILIATION:

1. Institut de Ciència de Materials de Barcelona (ICMAB-CSIC), Campus UAB s/n, Bellaterra 08193, Barcelona, Spain
2. Universidad de Málaga, Departamento de Física Aplicada I, Facultad de Ciencias, Campus de Teatinos, Málaga, Spain
3. ALBA Synchrotron, Cerdanyola del Vallès, 08290, Barcelona, Spain
4. Universitat Autònoma de Barcelona, Departament de Química, Facultat de Ciències, Campus UAB s/n, Bellaterra 08193, Barcelona, Spain
5. Universitat Politècnica de Catalunya, Departament d'Enginyeria Química, Escola d'Enginyeria de Terrassa, C/Colom 1, Terrassa 08222, Barcelona, Spain

INDUSTRIAL

LIAISON OFFICE

Relations with the industry

Núria Valls, Marta Ávila and Alejandro Sánchez
Industrial Liaison Office

After four years of industrial activity, the Industrial Liaison Office is well stablished and the main activities have been consolidated. One of the principal tasks of the Industrial Liaison Office is managing, promoting and increasing the industrial access to the synchrotron techniques of ALBA. Other remarkable activities have been also implemented and encouraged as for example the access to specialized support laboratories and the intellectual property and technological transfer activities. All that is supported through outreach campaigns focused on industry that have been enhanced during 2016.

Synchrotron techniques for industry

During 2016, the industrial usage of ALBA synchrotron techniques has been maintained to very satisfactory levels although it has slightly decreased compared to 2015 (Figure 28). The beamlines with more industrial usage were NCD, followed by XALOC and MSPD. Additionally, also CLÆSS, BOREAS and CIRCE beamtime was consumed by industrial customers. The industrial experiments and measurements cover a wide range of industrial sectors being the pharmaceutical the main one (Figure 29). The fact that remote access can now be offered at XALOC beamline has been a clear advantage to extend ALBA services to international pharmaceutical companies, in particular for the macromolecular crystallography technique. In 2016, a total of 11 different companies, either national or international, took profit of the state of the art synchrotron techniques of ALBA and interestingly, most of them performed several experiments per year. Different types of relationships have been set up with the industry and have been adapted according to their needs: from punctual services and short measurements to longer collaborations where public funds may also be obtained. In some cases, it has been necessary to use more than one technique in order to offer a complete service to the industry. In that direction, the experience and knowledge of ALBA scientists is crucial for offering a good service to the private sector. Additionally, synergies between university, ALBA and private companies have also been set up in order to carry out industrial research projects for those companies, enhancing the potentiality of each party as well as promoting the public-private partnerships.

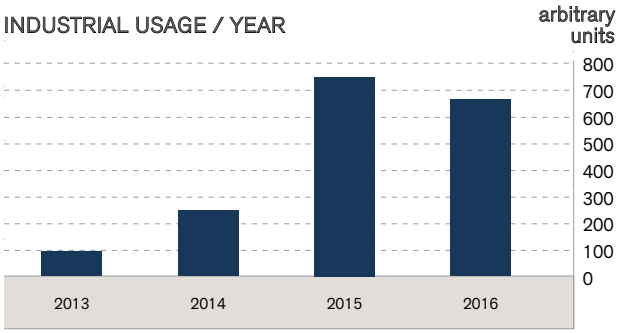

Figure 28. Evolution of proprietary access at synchrotron techniques per year.

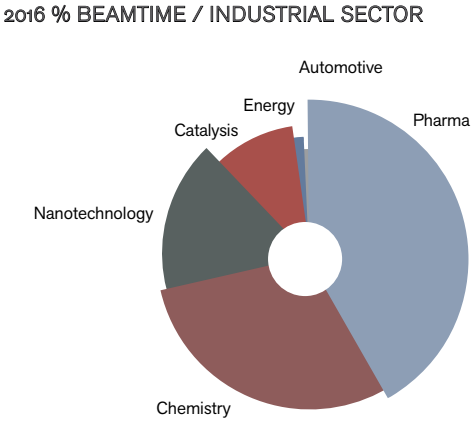

Figure 29. Access time per industrial sector for the period 2016.

Specialized laboratories with external usage

Another very relevant business activity of the ALBA Synchrotron is the proprietary access to the specialized laboratories such as the insertion devices-magnetic measurements (ID lab), the radiofrequency (RF lab) and the laboratory of optics and metrology. Those laboratories are supporting the synchrotron operations as well as open to proprietary access. In particular, the ID lab has been fully occupied all the year with magnetic measurements for external companies and institutions.

Intellectual property and technology transfer

Regarding the in-house developments, the ALBA Synchrotron is enlarging the patents portfolio and promoting their transfer to the private sector. During 2016, five new intellectual property registers have

been performed with the aim of being transferred through license agreements for their commercial exploitation. The inventions are being promoted with technological offers and have been published in the ALBA website: https://www.albasynchrotron.es/en/industry/technology-transfer

The current technology offers are as follows:

- New viewport design compatible with high vacuum
- A new bench concept for measuring magnetic fields of big closed structure
- Variable speed UHV chopper
- Two rotation mechanism for a beam stop in vacuum
- Angular orientable sample parking for a STM plates
- Motor device for actuating elements in ultra-high vacuum environments.

Industrial outreach

Although the industrial activity in ALBA has been increased in the last years, there is a long way to go in terms of outreach and promoting ALBA services to the industry. There are still a great number of companies that are not aware of the synchrotron-based techniques and developments and they may take profit of them. For that reason, during 2016, the Industrial Liaison team has increased the outreach activities addressed to the private sector.

On one hand, ALBA became member of the SECPhO cluster, whose mission is to bring together companies, technological centres and research groups in the photonics and optics sector with the purpose of putting together their needs and technical capabilities to build new projects or new collaborations. SECPhO is continuously organizing sectorial workshops in different fields. During 2016, the Industrial team has participated in several events with short presentations, such as the "Light applications for Cosmetics" together with the Beauty Cluster and ICFO or "Light Technologies & Advanced Materials" organized together with the cluster MAV (Advanced materials, ACCIÓ).

In May 2016, and for the four year in a row, the Industrial Liaison Office organized a sectorial workshop at ALBA. In this case, it was addressed to companies dedicated to cements, pigments, ceramics and glasses. It was a very important event for ALBA where private companies had the opportunity to learn about applications of synchrotron techniques. Almost 50 people from more than 30 different companies and institutions attended to the workshop and could enjoy the enthusiastic presentations from ALBA scientists, two talks from private companies with real case studies and it finished with a roundtable, networking

Talks and B2B meetings at the SECPhO workshops.

The industrial workshop was inaugurated by Jordi Baiget, Minister of the Catalan Government for Bussiness and Knowledge.

Pharmatech, Especial Cosmética 2016, no24

lunch and visit to the facilities. From this event, the first industrial user at the new beamline MIRAS emerged.

Following with outreach activities, the industrial office hosted one of the "Coffee with research" organized together with Fundació Catalana per la Recerca i la Innovació (FCRI) and Ibercaja. It was a three-hours meeting, focused on the pharma sector, where ALBA presented their capabilities to pharmaceutical companies. The Industrial Office has also participated in exhibitions, either national and international, contributions to specialized magazines: an industrial publication entitled "To study the skin with Synchrotron light" was published in the industrial journal "Pharmatech" in collaboration with the company Bicosome S.L. Finally, a great effort was made in order to compile the first brochure of ALBA focused on industrial applications. Download here the brochure: https://www.albasynchrotron.es/en/industry/industrial_applications_baja.pdf

TECHNOLOGY

ALBA is continuously improving and developing its instruments and technical capacities in order to maintain the facility in the forefront of research. In this respect, the year 2016 has not been an exception and, from the various ongoing developments, we are presenting in this section three projects which were completed last year.

The first one is related with a novel method to measure the electron beam transverse dimensions with micrometer precision (1 um= 10-6 m). This novel method permits the measurement of the full transverse beam profile using a rotating mask in an interferometry setup; and, for the first time in accelerators, the geometrical beam ellipse semi-axes and tilt has been inferred using synchrotron radiation interferometry. The method has been proposed as a way to improve the standard resolution, with the aim to measure the small beam sizes of the new generation of ultra-low emittance synchrotron light sources.

The second article presents the successful development of one of the world's most sensitive current detectors, able to measure down to 25 femto-amperes (1 fA = 10-15 A). In addition, it is fully flexible, allowing acquisitions under high voltage bias, synchronization of high speed data acquisitions in the so-called continuous scans, real-time feedback loops and online data processing. This ALBA development has been adopted as a standard for the experimental stations at MAXIV, the first 4th generation light source.

Thirdly, the development of an in-vacuum two rotation mechanism for a beam stopper for one of the ALBA beamlines is presented. At Small-angle X-ray Scattering beamlines (SAXS), beamstops are needed to block the intense primary beam that has not been scattered by the sample in order to protect the detector from any damage. This patented ALBA development, comparing with other alternatives, is more compact, allowing a better integration with the detector; and has better stability, improving the data acquisition quality of the experiments.

Full transverse beam profile reconstructions and ultra-small beam size measurements using synchrotron radiation interferometry

Laura Torino, Ubaldo Iriso

Contributions

Laura Torino was the main responsible of the project, under the supervision and guidance of Ubaldo Iriso. The results of this project were included in the PhD Thesis of Laura Torino.

Since the ALBA commissioning in 2011, the transverse beam size has been measured using an X-ray pinhole. In order to provide ALBA with an alternative transverse beam size monitor, it was decided to use the already existing diagnostics beamline "Xanadu" to perform beam size measurements using Synchrotron Radiation Interferometry (SRI).

This technique consists on a Young-like interferometry (see Fig. 30) that measures the light transverse spatial degree of coherence, from which the beam size is finally inferred.

After an important upgrade of the beamline hardware, the SRI is now providing reliable measurements of both horizontal and vertical beam sizes, as presented in Fig. 31.

However, SRI only provides a projected beam size. A novel method to obtain the full transverse beam profile using a rotating mask has been developed in the last year at ALBA. For the first time in accelerators, the geometrical beam ellipse semi-axes and tilt has been inferred using SRI. The same method can also be applied to improve the standard SRI resolution and measure ultra-small beam sizes.

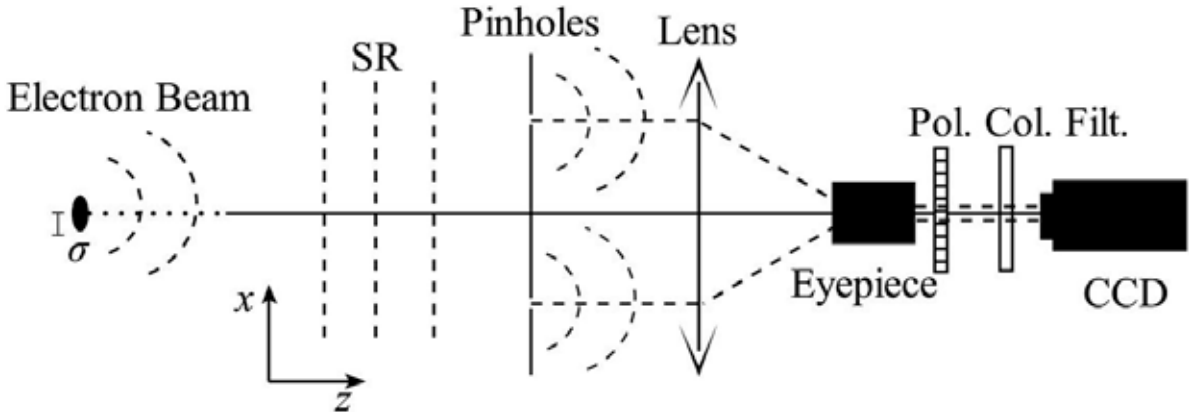

Figure 30: Sketch of the SRI experimental setup: the synchrotron radiation (SR) produced by the beam goes through the double pinhole system and is imaged through a lens and an eyepiece to the CCD. The radiation polarization and the wavelength are selected through a polarizer (Pol.) and a color filter (Col. Filt.).

Description of the project

New generation of synchrotron light sources are characterized by their low emittance and low coupling beams, with horizontal emittances in the nm range (or below). The beam coupling is usually controlled using skew quadrupoles and it typically ranges between ~[0.1, 2]%. Changing the beam coupling not only provides a change in the vertical beam emittance, it also produces a change in the beam tilt. Figure 32 shows the (modeled) behavior of the beam tilt angle, and the beam sizes along the first ALBA quadrant (where the SRI source point is located) for three different set of skew quadrupoles, providing three different beam couplings: note that in all dipoles, the beam tilt changes.

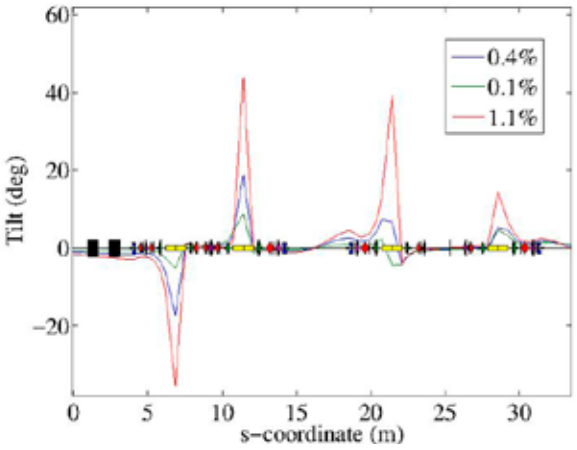

Figure 32: Beam tilt angle Φ for three different settings of the skew quads at ALBA in Sector 1. Bending magnets are represented by yellow rectangles. Xanadu beamline takes light from the first bending.

The standard SRI technique using a double-pinhole system only provides the projected beam size along the axes of the apertures and therefore information about the beam tilt change for different couplings is not available.

However a generic shape with a 2-axis symmetry, such as the beam ellipse, can be reconstructed by measuring its projections σ_p along different axis. This kind of measurements are performed rotating the double-pinholes mask by a given angle θ. When tilting the 2-pinholes axis by θ, the interference fringes obtained using the SRI setup appear tilted. Figure 33 presents interferograms obtained for pinholes axes rotated at 0°, 45°, 90° and 135° and the related fit, as measured at Xanadu beamline.

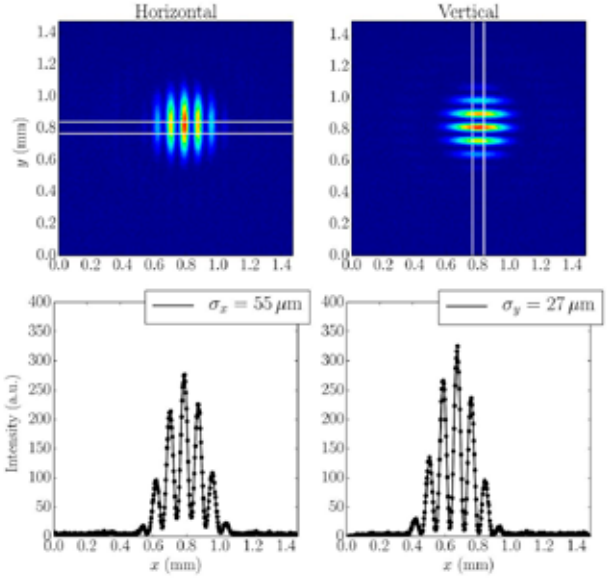

Figure 31: Horizontal and vertical SRI. Top images are raw interferograms, and the white lines indicates the slice used to obtain the beam size. The dots in the lower plots are the projections of the slices defined by the white lines. The black lines in the lowerplots are the results of the fitting process.

In Fig. 33, the projection σ_p is inferred by analyzing the fringes in the direction of the rotating angle θ. From each measurement at a given θ, two parallel lines tangents to the transverse beam shape are calculated. An example of beam reconstruction is presented in Fig. 34, top. Data were taken rotating the pinhole system every 5° in the range [0°, 200°]. This provides a "tomographic" reconstruction where the beam profile corresponds to the hollow shape enclosed by the black tangential lines. Obviously, the larger is the number of tangent lines, the more precise the beam shape can be reconstructed.

However, assuming that the beam is elliptic, only four lines are needed to obtain all the ellipse eigenvalues. The bottom ellipse of Fig. 34 has been obtained fitting four projections using the polar equation of the ellipse, and the result is compatible with the one obtained using 40 projections.

At ALBA the smallest vertical beam size achievable is 15 μm but other machines currently operate at beam sizes of 3.5 μm while future machines (like ESRF-II or Sirius) can reach σ_y = 2 μm, which cannot be measured with standard SRI technique due to practical limitations. The "rotating mask" technique can be applied to the measurement of this ultra-small beam sizes: Synchrotron Radiation Workshop (SRW) simulations were performed to prove this possibility. An elliptic beam with zero tilt and an horizontal beam

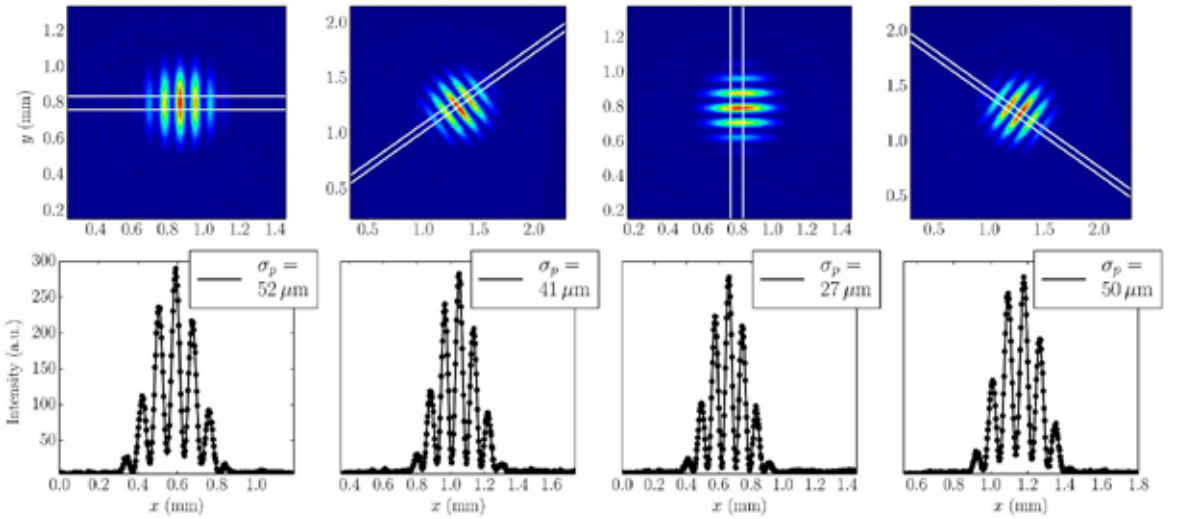

Figure 33: Interferograms rotated at 0°, 45°, 90°, and 135° to measure the size of the projection of the beam along the respective axis. White lines in the top plots are oriented in the direction of the pinholes axis, rotated by angle θ, and represent the slices selected for the fitting process.

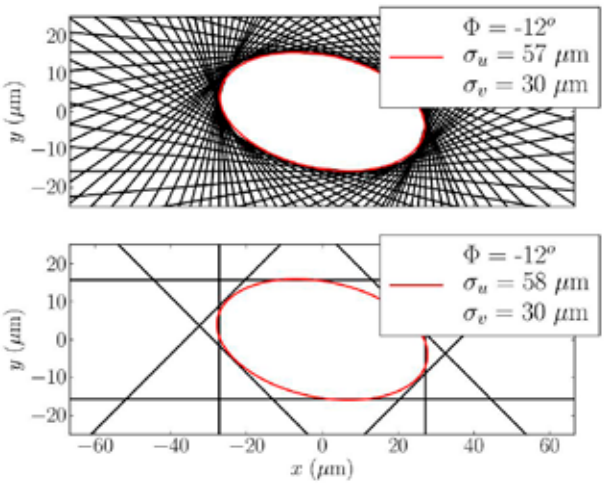

Figure 34: The top plot shows the full reconstruction of the transverse beam shape using tangents lines. In the bottom plot, only the lines obtained by the projections at 0°,45°, 90° and 135° are considered.

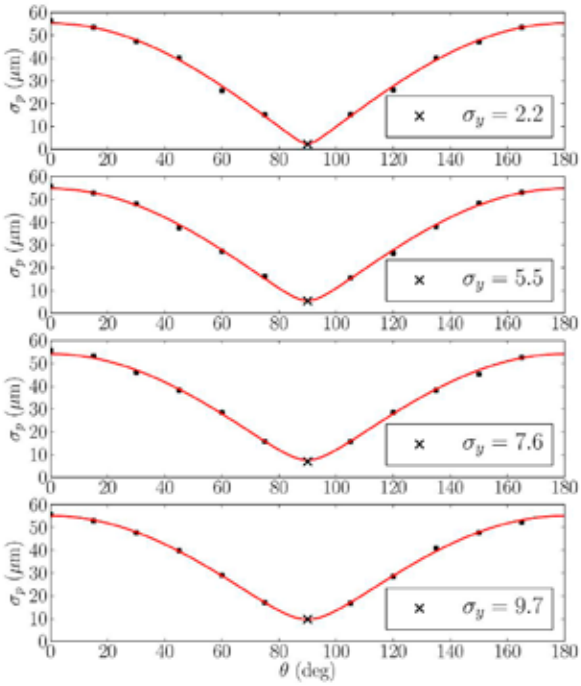

Figure 35: SRW simulated 2, 5, 7 and 10 μm vertical beam size reconstruction using the rotated SRI technique. Black dots are the SRW simulated data, the error bar is fixed to 1.5 μm and red line is the result of the fit using the ellipse polar equeation. Black × indicates the inferred vertical beam size, using the fit.

size of 55 μm was generated. The vertical beam size was changed from 2 to 10 μm and the tilt angle left at 0 for simplicity. To perform the beam reconstruction, projection measurements were simulated sampling the angle in steps of 15°, by skipping θ = 90°, which corresponds to the minimum beam size.

Final interferograms were analyzed and the projected beam sizes as a function of the angles were fitted using the polar equation for the ellipse to obtain the beam parameters. Figure 35 presents the results obtained when simulating a non-tilted beam with horizontal and vertical beam sizes of 55 μm and 2, 5, 7 and 10 μm respectively. The minimum beam size is inferred from the SRI measurements obtained at larger beam sizes using the ellipse equation. Note that the obtained results are compatible with the initial parameters.

Conclusions

A reliable set-up to measure the transverse beam size was developed using the Synchrotron Radiation Interferometry (SRI) in the ALBA diagnostic beamline Xanadu. Once the SRI technique was reliably implemented, further improvements were developed. In particular a method to fully reconstruct the transverse beam shape by rotating the double-pinhole mask was successfully developed and tested. The method allows to measure, using the SRI, all the geometrical beam ellipse parameters: horizontal and vertical beam size and the beam tilt angle. It was demonstrated, via SRW simulations, that the same technique can be used to perform ultra-low beam size measurements (down to 2 μm), which can be of great help for the future light sources like ESRF-EBS (France) or Sirius (Brazil).

OTHER REFERENCES

[1] L. Torino and U. Iriso. *Transverse beam profile reconstruction using synchrotron radiation interferometry. Phys. Rev. Accel. Beams*, **19**(12):122801, (2016).

For further information and details, complete thesis of Laura Torino here: https://etd.adm.unipi.it/theses/available/etd-01252017-183822/unrestricted/LauraTorino_PhDThesis.pdf

Em# electrometer comes to light

J. Ávila , M. Broseta, G. Cuní, O. Matilla, A. Ruz , M. Rodríguez, J. Salabert, X. Serra

Contributions

J.Ávila, X. Serra and O.Matilla have been in charge of the hardware design of the equipment, A. Ruz has been responsible of the mechanical design, J.Salabert and M.Rodríguez were in charge of the SBC specification and development of the embedded Linux distribution, M. Broseta and G.Cuní have developed the SBC software that controls the equipment and its integration to the Control System. It also has to be specially mentioned the contribution of all the people that worked in the previous version of ALBA Em: specially J.V. Gigante, J. Lidón-Simón and J.Jamroz. Our acknowledge to David Fernandez for his strong support for the project and continuous advises. And finally also to thank all the Electronics Section members that contributed with their work to produce the first Em# units.

This article reviews in detail the redesign of the four independent channel electrometer, designed by the ALBA Synchrotron. The new device, named Em#, is more versatile and competent than its predecessor.

High accuracy low current readout is an extensively demanded technique used in 3rd generation synchrotrons. They comprise a need both for diagnostics and data acquisition in today's photon labs. In order to tackle the problem of measuring from various sources of different nature and magnitude synchronously, while remaining flexible at the same time, ALBA developed years ago a four independent channel electrometer, the Em. It was based on transimpedance amplifiers with an Analog-to-Digital Converter (ADC) integrated and an Ethernet communication port. The project started in 2011 and more than forty units are currently working at the ALBA facility since then. Due to the constantly increasing requirements, mainly related to data acquisition of experimental data, a full redesign of the device was carried out: the result is the new ALBA Em#.

This new development takes advantage of the experience acquired with the previous current amplifier improving the ground architecture to achieve ultra-low current measurements capabilities and enabling current acquisitions under voltage biased conditions up to 1kV. The Em# includes a new ADC with higher resolution and sampling rates. Finally the whole digital processing architecture has been redesigned to have a more versatile instrument capable to implement real-time signal processing, feedback systems and easily integrate them into the accelerator Control System.

Acquisition

The ALBA Current Amplifier is the sensing element and the equipment's core with 8 available

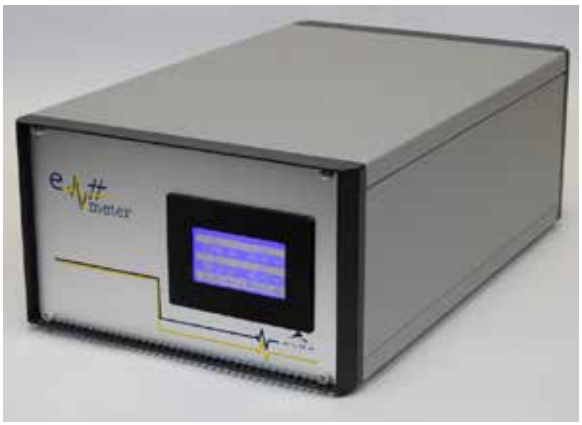

measurement ranges from 100pA to 1mA and different selectable second order filters. It has proved a very good performance in the previous version and it is the only element inherited from first ALBA Em. In Em# an improved thermal management and the addition of an internal temperature sensor have been implemented.

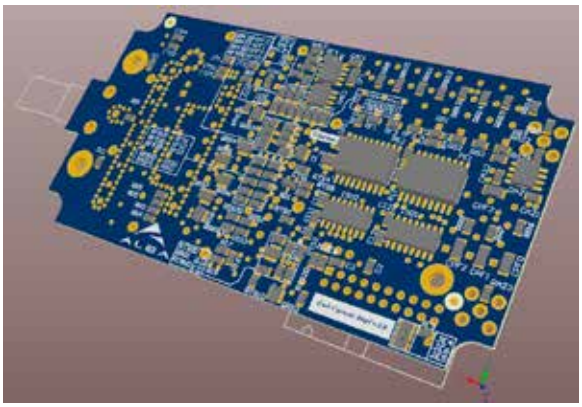

Figure 36: Detail of current amplifier PCB design.

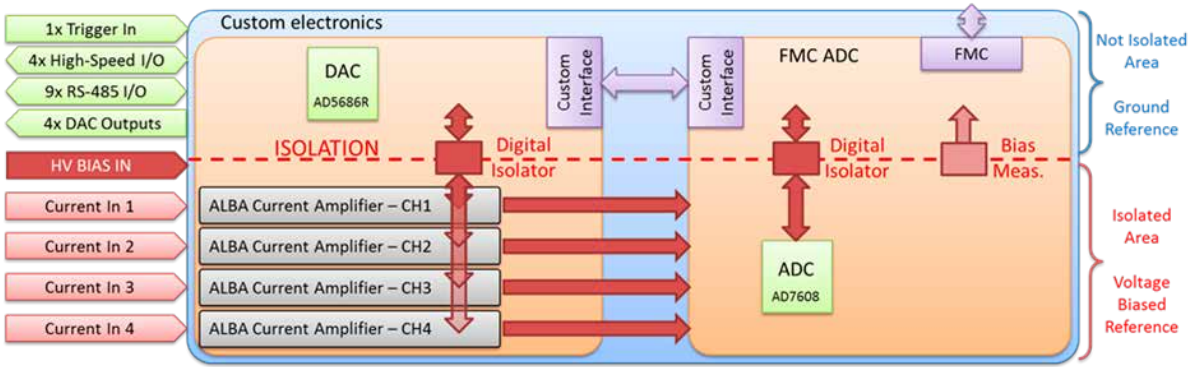

Figure 37: Comparison of the integrated position FFT spectrum (log scales).

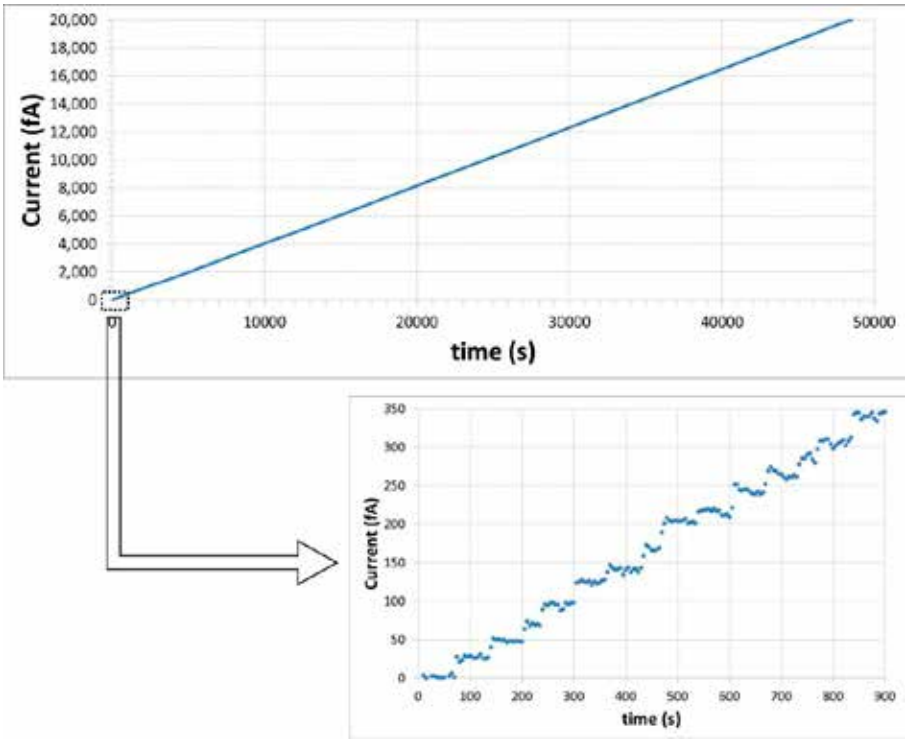

Figure 38: Acquisition of a 20 pico-amperes current ramp composed by 25 femto-amperes steps using 1 nano-ampere range. The fact of being able to identify the steps involves a dynamic range in the measurement in the order of 10^5.

Processing & Feedback

The instrument implements new ground configurations: the measurement ground is completely isolated from the reference ground and able to withstand up to 1kV voltage difference. A new 18bits ADC, with increased sampling rate up to 400kS/s to reduce noise, has been added using this measurement ground. In practice, this involves the current being transmitted internally using parallel digital isolators. The objective is to increase the signal-to-noise ratio as much as possible reducing the pick-up noise to a minimum level.

The first measurements acquired with the equipment have confirmed all these assumptions showing almost undetectable current leaks, a very good Signal to Noise level (S/N) that lead to very high dynamic ranges.

One of the main objectives of Em# project is to endow the equipment with the capability of real-time processing of the acquired data, to be able to implement a wide range of feedback regulated systems. The core of the acquisition engine of the Em# is commanded using a Field-Programmable Gate Array (FPGA) that synchronizes all input and output triggers, drives the acquisition ADC, processes all acquired data and produces arbitrary outputs via the four analog signals via a Digital-to-Analog Converter (DAC). All these processes are completely independent of the higher level control layers.

The objective is that the equipment will have the inherent capability of acquiring/providing in parallel timestamped data and analog outputs in the order of micro-second range. That would allow complex

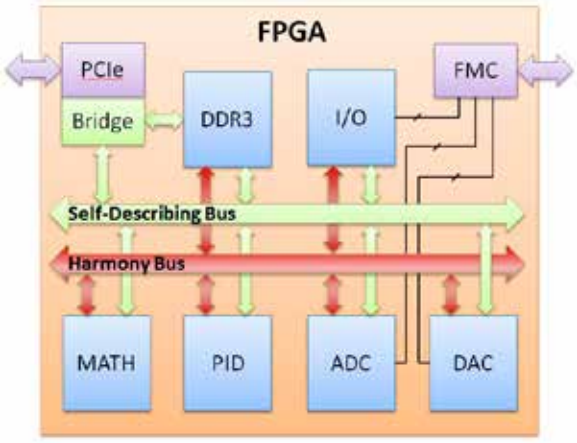

Figure 39: Internal FPGA dual bus block diagram.

setups involving readings of motor encoders, strain gauges, actuating piezos or arbitrary triggers very common in experimental stations in the beamlines. Moreover a generic architecture inside the FPGA has been implemented using an innovative dual bus strategy with the objective to ease multiple implementations from higher layer controls without the need of a complete low-level redesign.

The first bus is an already existing generic solution: the Self-Describing Bus (SDB) developed by CERN and GSI under General Public License (GPL) [1]. It enumerates and defines the different independent modules (Logic Cores) synthetized in the FPGA, as well as the registers accessible from PCIe. A drawback of this bus is a certain non-determinism given by its variable latency. To solve this, a secondary data bus is used for the cores interconnection at high speed data rates: the Harmony Bus.

All Logic Cores are configured via the SDB including a unique identifier used in Harmony Bus transmission. This identification allows other cores to share the data among them. This general configuration scheme leads to a flexible and capable of implementing complex processing strategies where data is captured, stored, processed and transmitted between each sub-module deterministically.

Integrated Control System

The new Em# includes a Single Board Computer (SBC) running an Embedded Linux OS specially customized for it. It runs the high-level software layer with the control routines. This approach packages the communication protocol and high level functions into a software layer running in the SBC, and the low level fast data acquisition firmware, integrated in the FPGA. This two layers architecture reduces the load of the FPGA and makes easier to implement new functionalities without the need of a complete redesign.

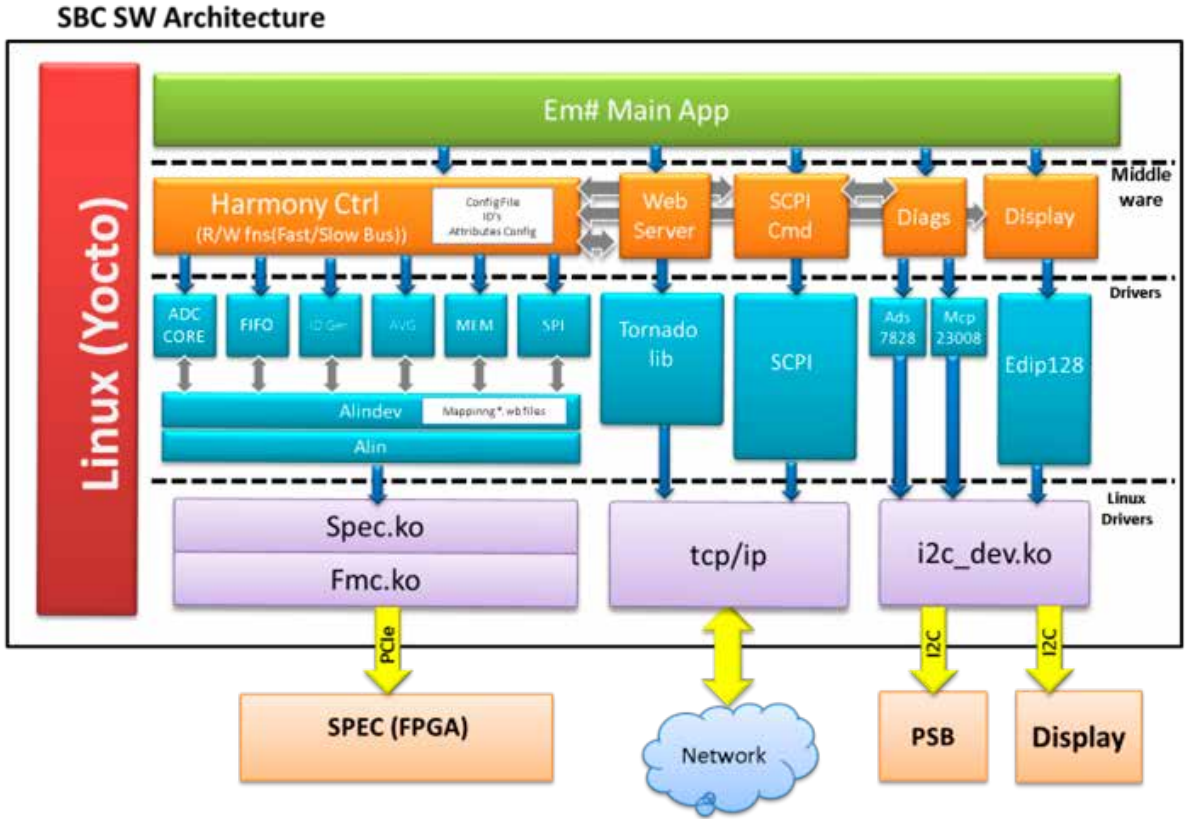

Figure 40: Internal high level software diagram divided in different layers.

Figure 41: Em# web Interface accessible by the users.

Apart from a built-in web interface, which provides a full supervision of the instrument and offers a complete configuration graphical interface to the user, it also implements an ASCII protocol that complies with the Standard Commands for Programmable Instruments (SCPI) for a straight-forward integration into any control system.

Conclusions

Commercial Off-The-Shelf (COTS) solutions are available in the market to measure very low currents with high precision. These options are expensive and do not completely fulfil some specific requirements common at synchrotrons; such as acquisitions under a high voltage bias, synchronization of high speed data acquisitions with other detectors and motions in the so-called continuous scans, real-time feedback loops and online data processing. The Em# project aims to solve most of the identified needs so that one instrument can be used for multiple purposes across the whole facility.

The project, initially developed at ALBA, became a collaboration after MAXIV and ALBA signed a collaboration agreement for the Em# development in June 2015. After two years of intense design process, first units of Em# have come to light: twelve units have been produced at ALBA and forty more are being produced at MAXIV.

The first measurements demonstrate an excellent accuracy in the acquisitions. The following steps of this project will tackle a number of applications in particle accelerators, which Em# has been conceived for, pushing the limits of the current state-of-the-art instrumentation.

OTHER REFERENCES

[1] A.Rubini, W. Terpstra, M. Vange, "Self-Describing Bus (SDB) – Specification for Logic cores – Version 1.1", April 2013

[2] *X.Serra-Gallifa, et al., "Harmony: A Generic FPGA Based Solution for Flexible FeedBack Systems"*, ALBA-CELLS Synchrotron, FRFMPLCO06, PCaPAC 2016

[3] M.Broseta, et al., "Embedded Control System for Programmable Multi-Purpose Instruments", ALBA-CELLS Synchrotron, THDAPLCO01, PCaPAC 2016

[4] O.Matilla, et al., "Em# Platform: Towards a Hardware Interface Standardization Scheme", ALBA-CELLS Synchrotron, WEPGF081, ICALEPCS 2015

[5] X.Serra-Gallifa, et al., "Em# Project. Improvement of Low Current Measurements at ALBA", ALBA-CELLS Synchrotron, TUPPC094, ICALEPCS 2013

[6] J. Lidón-Simon *et al.*, "Low Current Measurements at ALBA", Proceedings of ICALEPCS'11. WEPMS025

[7] *Open Hardware Repository, Wishbone Slave Generator*, http://www.ohwr.org/projects/wishbone-gen

Two-rotation mechanism for an in vacuum beamstop

J.B. González, C. Colldelram

Contributions

J.B. González, L. Nikitina and C. Colldelram were responsible for the engineering mechanics design and implementation. José Ferrer, Jordi Navarro, Manuel Murcia and Oscar Borrego were responsible for the assembly and installation. G. Jover was in charge of the development of the control system software. A. Fontsere and B. Saló were responsible for the electronics. M. Llonch and J. Ladrera were in charge of survey and alignment measurements. D. Calderón and L. Ginés were responsible of vacuum conditioning and tests. This was carried out with important contributions from transversal engineering in the engineering division and the electronics technicians and computing engineers.

At Small-angle X-ray Scattering beamlines (SAXS), beamstops are needed to block the intense primary beam that has not been scattered by the sample in order to protect the detector from any damage. Beamstops are usually confined inside a vacuum tube minimizing air space between the sample and the detector. For certain experiments, a motorized beamstop is required to achieve a precise positioning in different regions of the detector active area. ALBA has developed a new motorized beamstop consisting of a two-rotation mechanism inside vacuum that composes a movement able to cover all range of the active area of the detector. The presented solution involves a main rotation reached by a gear and a worm drive actuated by a stepper motor and a second rotation relative to the main one produced by a piezo rotation stage. For each position, two different solutions appear. This characteristic permits to take two equivalent images in the detector with the same beamstop position but different orientation in the beamstop support; thus allowing the compensation of the support shadow on the active area of the detector.

Description

ALBA has developed a new motorized beamstop consisting of a two-rotation mechanism inside vacuum that composes a movement able to cover all range of the active area of the detector (Fig. 42), permitting for each position two different solutions.

The complete mechanism is confined in a vacuum chamber that belongs to the vacuum flight tube between the sample and the detector. The mechanism involves a main rotation reached by a gear and a worm drive actuated by a stepper motor and a second rotation relative to the main one produced by a piezo rotation stage (Fig. 43). The vacuum chamber contains fixed supports for appropriate bearings which permit the main rotation of the axis. The relative rotation holds the beamstop support that consists of a rod usually made of a material partially transparent to the beam. Finally, the beamstop itself is mounted in the extreme of this support and consists of a cylindrical block of an opaque material to the beam.

This motorized beamstop is more compact and shows a better stability than other conventional alternatives such as linear stages due to a shorter and stiffer beamstop rod and a more packed mechanism.

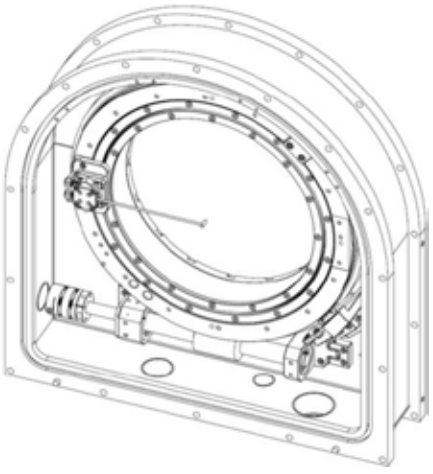

Figure 42: Beamstop main view.

Description of movements

The beamstop is moved with the relative rotation and in turn, the latter is driven by the main rotation (Fig. 44). Moving each rotation a certain angle, the mechanism covers the full active area of the detector and permits the positioning of the beamstop at any point.

For a position of the beamstop given by the coordinates (a,b), the solutions of a system of polynomial equations of two circumferences, one with the centre in the main rotation (0,0) and the other with the centre in the beamstop position (a,b), are the two points of intersection between them. With these two intersection points it is possible to resolve the two angles for each of the two solutions (Fig. 45).

At the same time, these two solutions allow to take two identical images in the detector with the same beamstop position but different orientation in the beamstop support (see example in Fig. 46).

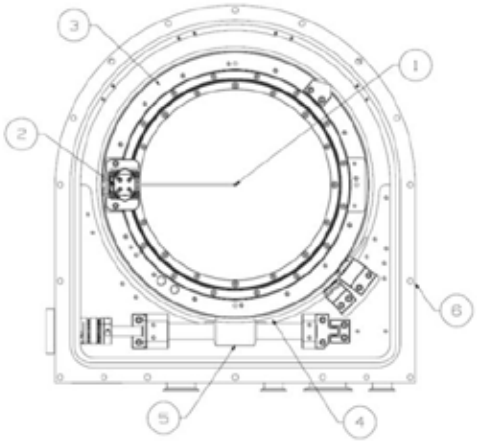

Figure 43: Parts breakdown. (1) Beamstop, (2) second rotation, (3) main rotation, (4) gear, (5) worm drive, (6) vacuum chamber.

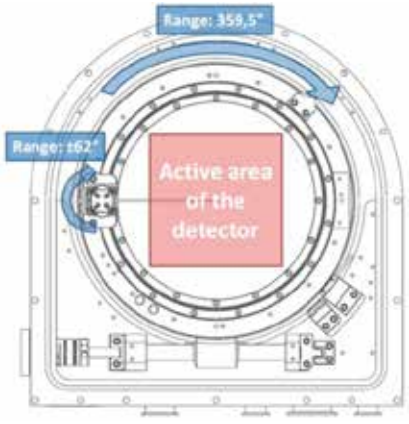

Figure 44: Movements description.

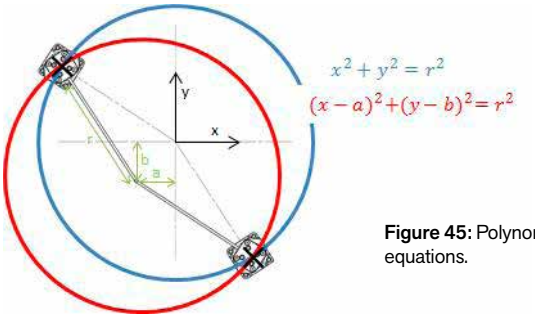

Figure 45: Polynomial equations.

Assembly, tests and installation

The manufacturing of the parts and their assembly have been performed following high vacuum cleaning procedures (Fig.47).

In order to test the pseudo motors (x-y movements based in the two rotation movements), a laser tracker and a prism attached to a beamstop dummy has been used. The laser tracker provided several positions of the beamstop dummy and these measurements were correlated with the theoretical position given by the equations in order to validate the control system.

Finally, the beamstop was installed in the Flight Tube section in the End Station of NCD beamline.

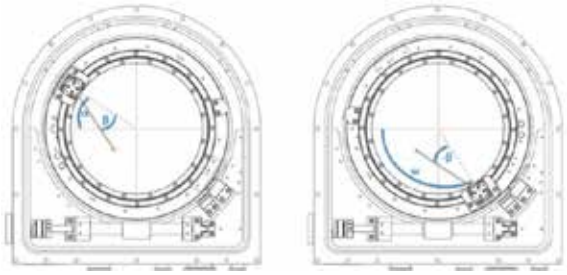

Figure 46: Two solutions for the same position.

Figure 47: Vacuum cleaning procedures during assembly.

Conclusions

ALBA has developed a design of an in-vacuum motorized beamstop based in a two-rotation mechanism that composes a movement able to cover all range of the active area of the detector and allows two solutions for each position. This last characteristic permits the compensation of the support shadow on the active area of the detector, likewise the mechanism is more compact and shows a better stability than other alternatives. For all these reasons, the two-rotation mechanism for an in vacuum beamstop is an advantage for certain experiments in Small-angle X-ray Scattering beamlines. This design has been patented under the Spanish Patent and Trademark Office with No. P201631058 [1].

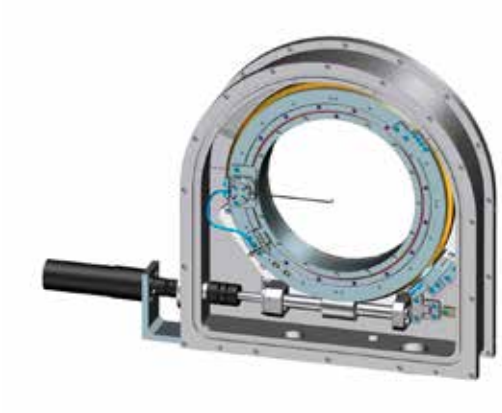

OTHER REFERENCES

[1] J.B. González & C. Colldelram, "Dispositivo de tope para haces de radiación", Spanish Patent and Trademark Office and No. P201631058, Aug. 1, 2016.

2016 IN ALBA

JANUARY

Ramon Pascual honoured and awarded by Catalan and Spanish governments

Two different events were organised during the year by the national and regional administrations for paying tribute to Ramon Pascual, president of the Executive Commission of the ALBA Synchrotron from 2003 to 2016 and promoter of the project. In January, he received from the Spanish government the "Alfonso X El Sabio" award, which recognises persons and institutions with merits in education, science and culture. In September an event was held at the Palau de la Generalitat de Catalunya with the presence of several authorities.

FEBRUARY

Green light for the construction of the 10th beamline: XAIRA

The ALBA Synchrotron initiated 2016 with the construction of its new microfocus beamline for macromolecular crystallography. The 10th ALBA beamline will contribute to a better understanding of complex biological system and is planned to be ready for first experiments in 2020.

MARCH

Five years of synchrotron light in ALBA

On the 16th of March 2011, the electron accelerator emitted synchrotron light for the first time. That moment was the starting point of the ALBA Synchrotron that, one year later, began the first experiments. Five years later, ALBA organised an event to celebrate this anniversary with all the staff, counting with the presence of the former responsible of the Accelerators division, Dieter Einfeld.

APRIL

MIRAS starts commissioning

The 8th ALBA beamline - devoted to infrared microspectroscopy - started its commissioning in April getting the first synchrotron light outside the accelerators' tunnel aligning in-tunnel transport mirrors. This was an important milestone in the construction of the beamline, which was initiated in 2014.

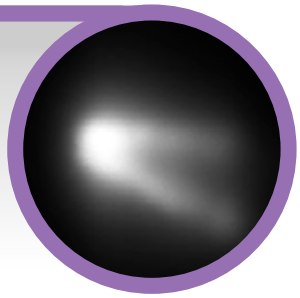

MAY

Synchrotron light for improving industrial products and processes

Around 50 people from more than 30 different companies and institutions attended the industrial seminar organized by ALBA. There, they were able to find out the main advantages of using synchrotron light for analysing materials such as cements, pigments or ceramics (faster experiments, more flexibility in the experimental conditions, lower detection levels and higher resolution, among others). The event was officially opened by the Minister of Business and Knowledge of the Catalan Government, Jordi Baiget.

JUNE

Opening doors to more than 2,000 people in the successful ALBA Open Day

Excitement, interest and enthusiasm were present among the participants of the 5th ALBA Open Day. The event welcomed 2,130 people that came to the facility to see their equipment and talk to their scientists and technicians – 82 volunteers – through an itinerary composed of different areas of exhibition and demonstration. Like in previous editions, the tickets for the ALBA Open Day ran out two weeks before the event.

JULY

New Computing developments

During the whole year, several developments have been gradually making process. A new Service Desk, based on Jira solutions, has been released, making easier the management and tracking of internal developments in-house.

AUGUST

Shutdown for implementing new upgrades in the beamlines

Apart from the ordinary tasks, during the summer shutdown several upgrades were developed at the beamlines. For instance, MARES endstation of BOREAS beamline, composed by an UHV reflectometer for scattering and reflection, was commissioned. Besides, a new redesign of the SAXS/WAX endstations at the NCD beamlines was performed.

SEPTEMBER

ALBA Synchrotron welcomed more than 500 experts on particle accelerators

From 11 to 16 September ALBA hosted IBIC (International Beam Instrumentation Conference) and MEDSI (Mechanical Engineering Design of Synchrotron Radiation Equipment and Instrumentation) conferences. 531 researchers and engineers came from all over the world to participate in both events, organised by the ALBA Synchrotron. A common guided tour around the facility was also held.

OCTOBER

Inauguration and first official users at MIRAS, the infrared beamline

The 8th beamline MIRAS was inaugurated in a ceremony with the participation of authorities from the Catalan and the Spanish governments. Synchrotron infrared microspectroscopy is a very powerful tool for detecting and quantifying molecules and its spatial distribution. Also in October the beamline hosted its first official users: researchers from the Institute of Advanced Chemistry of Catalonia (IQAC-CSIC) who analysed how lipid systems penetrate into the different layers of the skin.

NOVEMBER

2017-2020 Strategy Plan

In 2016, the process of defining the 2017-2020 Strategy Plan of the facility has been initiated. This document, which will be completed in 2017, will be useful to focus on selected scientific priorities, aiming at targeting the national and international communities, design the next future and provide an outlook to what the facility will be in one decade from now.

DECEMBER

A new portal for making more accessible information to citizenship

The Transparency Portal has the aim of enabling citizens to have fast and easy access to information about institutional, organizational and economical aspects of CELLS, the public consortium that managed the ALBA Synchrotron. The website also includes a direct communication channel allowing citizens to ask for additional information through an on-line form.

MIRAS: The Infrared Synchrotron Radiation Beamline at ALBA

A brief report is presented here to highlight the main activities performed in 2016 that made possible to start fully operation of MIRAS in 2016, including also some examples of applications.

After the construction and installation phases of the beamline during 2015 and the first months of 2016, the commissioning with synchrotron light started on April 2016. The beam transport mirrors were aligned until the first focus of synchrotron light was obtained outside the tunnel. During May 2016, all the transport mirrors of the beamline were aligned until the coupling of the synchrotron light with the beamline endstation. The first infrared spectrum was obtained which was followed by the full commissioning and performance testing. MIRAS started operation with friendly users in July 2016; three different groups (working on Material Science, Archaeology and Biomedicine) performed successful measurements. The beamline is currently running with official users since October 2016, two months earlier than originally foreseen.

Upon coupling the infrared microscope station with the synchrotron beam, several tests were carried out in order to scale the beamline performances with other internationally competitive. Figure 48 displays the single beam intensity, recorded with small aperture of 10 microns, with the synchrotron source and with the Globar (thermal) source, under the exact same conditions.

The measurement was performed in the confocal reflection mode of operation of the FTIR microscope using a gold substrate as a reference sample.

Figure 49, shows the 100% line calculated in the transmission mode using an aperture size of 10x10μm^2, in confocal geometry with 16 seconds scans and 4cm^{-1} spectral resolution. The 100% line is normally used to compare and calculate the noise level of the spectra which can be generated by several factors. It is usually calculated by subtracting the sample spectrum from the background spectrum.

The spectra format is shown in the transmittance unit (T%) as represented in the figure 49. The figure shows, the noise level of the Globar source and the synchrotron beam. The synchrotron beam is about two times less noisy on average.

We used the resolution test sample (USAF metal (Cr) on glass) to measure the spatial resolution of the microscope with the synchrotron source. USAF resolution test target made of a metal coating on glass; into the metal layer the resolution test structures are patterned. Therefore the metal is a high reflectivity sample whereas the glass within the test structures is more absorbing in the infrared. The reflectivity of the glass in the mid-IR is only 15% that of the metal coating. The first measurement shown in Figure 50 was done with the synchrotron light source in confocal reflection mode using the 36x objective of the microscope and with an aperture size of 5x5 microns and 2.5 microns Step Size.

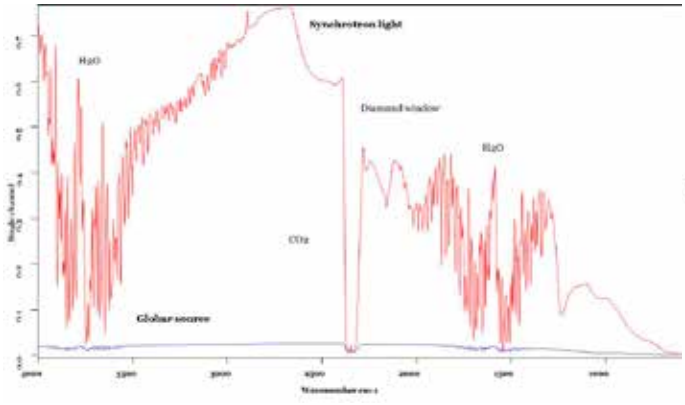

Figure 48: First Synchrotron FTIR single beam spectrum recorded at the MIRAS Beamline.

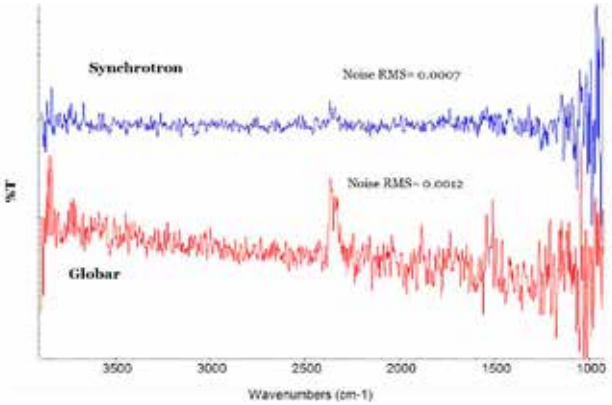

Figure 49: shows the noise level of the Globar source and the synchrotron beam. The synchrotron beam is about two times less noisy on average.

Capabilities and Application (some examples)

The applications of this beamline will cover a wide range of research fields, including surface and material science, biochemistry, microanalysis, archaeology, geology, cell biology, biomedical diagnostics, environmental science, etc. The discipline of life sciences will represent the main body of research, with direct impact in the study of different disease states. This technique will also be helpful in surface science applications, in particular, the analysis and chemical imaging of thin films and protection layers. In addition, high-pressure studies using Diamond Anvil Cell like those performed in geological, environmental sciences and astrophysics will also benefit from MIRAS.

From the biomedical applications performed at MIRAS, one project, involving collaborators from Universitat Autònoma de Barcelona (UAB, Spain), Centre National de la Recherche Scientifique (CNRS, France) and Keele University (UK), consisted in getting new insights into the radio-sensitization effects of nanoparticles and radiotherapy. The promising results on the enhanced effectiveness of tumour cell killing in several radiobiological experiments have brought the combination radiotherapy-nanoparticles an increasing area of investigation. However, the mechanisms of action are not clear yet. In addition to the damage due to a possible local dose enhancement, the interaction of nanoparticles with essential biological macromolecules could lead to changes in the cells contributing to an amplified effect of the radiation. Within this context, Fourier Transform Infrared Microspectroscopy (FTIRM) has been employed at MIRAS to investigate the biochemical features of tumour cells induced by several types of nanoparticles and clinical radiotherapy beams. Multivariate analysis of the recorded spectra using principal component analysis reveals (Figure 51) clear differences in the DNA, protein and lipid regions in the presence of nanoparticles and/or radiation. Biochemical changes related to the hallmark characteristics of cell death are detected, including a shift towards low wavenumbers in the amide I and II bands, relative amplitude changes in the CH_2 and CH_3 stretching modes, along with DNA chromatin condensation indications. Nanoparticle-induced biochemical alterations are amplified in the presence of radiation.

In this work, we have assessed the infrared spectral modifications induced by X-ray irradiations combined with Gd nanoparticles on F98 cells, at 0 and 24 hours post-irradiation. PCA analysis indicates clear differences between the treated groups nanoparticles and/or radiation). We observe changes at a biochemical level in the presence of nanoparticles, indicating changes in the cellular function; these alterations are then amplified with the subsequent irradiation.

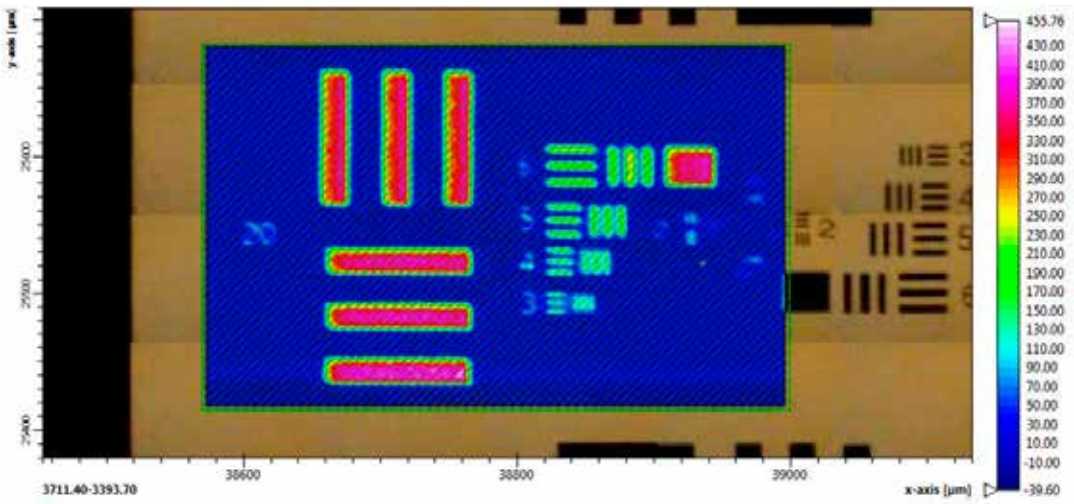

Figure 50: Image of a resolution test target (USAF (metal (Cr) on glass), shows clearly resolved 3 µm lines and spaces. The image quality is dramatically better than the image taken with the Globar light source.

Immediately after irradiation, slight changes in the intensity and in the position of the PO2– symmetric and asymmetric modes were observed. This could be related to the initial radiation damage in the DNA, which is increased in nanoparticle treated cells. At 24 hour post-irradiation, biochemical changes are better manifested and they are related to the hallmark characteristics of cell death. Changes include a shift toward the low wave numbers in the amide I and II bands, relative amplitude changes in the CH2 and CH3 stretching modes, along with DNA chromatin condensation indications arising from variations in the phosphodiester DNA modes.

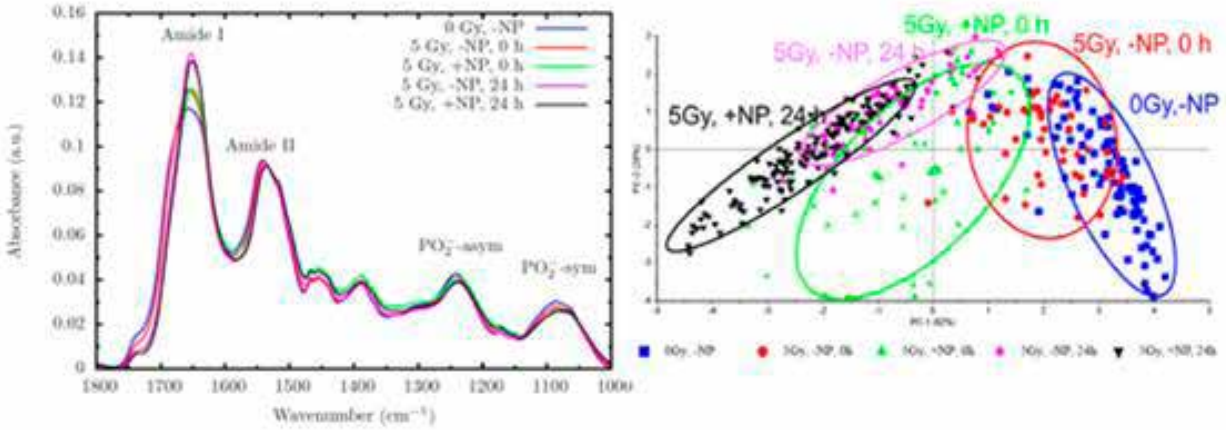

Figure 51: An example showing the results of FTIR study of the biochemical effects in F98 glioma cells induced by radiotherapy irradiations in conjunction with Gd nanoparticles exposure.

HEALTH AND SAFETY

Safety is a genuinely transversal activity, which involves all divisions and offices of ALBA. The Health and Safety office, reporting directly to the ALBA director, leads and follows-up all efforts therein, with the ultimate goal of having safety *integrated* into all ALBA activities. The ALBA director also has the support of the Health and Safety Council (CSS), a consultive organism which includes workers' representatives and member appointed by the director. The CSS had five plenary meetings along 2016, in which many different aspects were discussed, with particular emphasis on following-up the existing program of preventive activities for 2016. In this section some health and safety aspects relevant during 2016 are highlighted.

During this year the 8th ALBA beamline, MIRAS, started regular operation, as reported elsewhere. Previous to the achievement to the major milestone number of steps had to be taken, particularly in terms of radiation protection safety. An inspection with the Nuclear Safety Council (CSN) was conducted and the areas adjacent to the beamline were carefully surveyed during the commissioning period, confirming the results previously anticipated by the detailed simulations. The license for operation with external users was granted as planned. Regular survey of radiation safety aspects at ALBA was developed as usual, without any relevant news. By the end of the year a new technician joined that Health and Safety office, with the objective of reinforcing precisely the area of radiation protection.

In the area of occupational safety one of the main efforts done during 2016 was to update the ALBA emergency plan (formally denominated *Self-protection plan*), which takes care of establishing the basic rules to be applied in case of an emergency. The plan contemplates three different teams which may be activated depending on the circumstances, devoted to: first-aid intervention, staff evacuation and first intervention (for example in case of fire). These teams involve a substantial fraction of the total number of ALBA workers. Team members undergo specific training and participate in ad-hoc organization meetings and drills.

Preventive activities at ALBA are the object of a number of tools and actions, complementary to one another, which are systematized and coordinated in a document called the Prevention plan. During 2016 the effort started to revise the current plan in order to have a new version, more adapted to the intense operation activities and simultaneous process of beamline construction. The new plan was not yet finished at the end of 2016, having the objective of completing this work in 2017.

Risk assessments are an essential preventive tool, which allows anticipating the type and severity of risks inherent to the different activity done or planned at ALBA and plan preventive actions therein. During 2016 a systematic review of previous risk assessments proceeded and gained momentum, so as to continuously update this central preventive tool and have an incremental improvement of health and safety conditions. Risk assessment and evaluation is done by a specialized external company and coordinated and implemented by the Health and Safety office, in close interaction with the ALBA controllers, workers and health and safety representatives.

Follow-up of experiments done at ALBA by external users is also one of the main preventive efforts, done jointly by the beamline scientific and technical staff, the users themselves, Health and Safety office and User office, among others. Preventive actions start early-on, with the revision of the proposed experiments, wherein scientific staff and Health and Safety office closely collaborate, continued shortly before the experiment takes place and completed during the days the experiment is executed at ALBA. The previously established rules have been applied systematically and improved wherever possible. One very relevant improvement, implemented by the end of the year, was the incorporation of the floor coordinators, staff ascribed to the Experiments division who work in shifts and closely collaborate with the Health and Safety office in the follow-up and supervision of safety aspects on the ground. This new system shall be further consolidated during 2017.

Last but not least, a word must be said about health and safety training activities. Based on the principle of *integration* set forward above, it is absolutely essential that the different actors involved receive proper training, so that they can effectively discharge their corresponding responsibilities. During 2016 a total of no less than 20 training actions (courses, practical sessions) specifically addressing safety have been carried out (excluding the ad-hoc safety training sessions conducted with each new ALBA worker, student, collaborator or user group). Continuous education and training is seen by ALBA as a key ingredient to have safety improved.

By the end of the year a detailed planning of the activities to be carried out in relation to health and safety during 2017 was elaborated, exposed to the CSS and approved by the director.

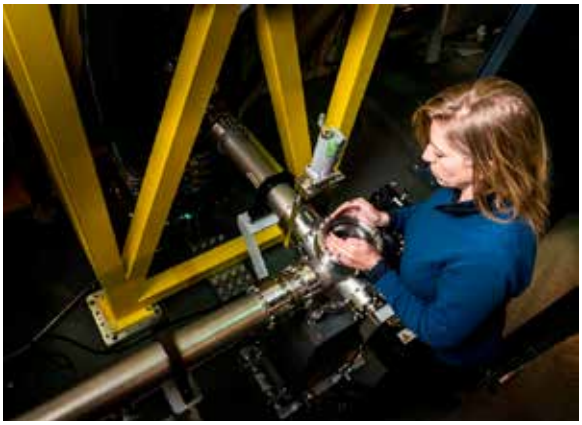

External shielding of the MIRAS beamline.

One training session organized by the Health and Safety office.

COLLABORATIONS, CONFERENCES AND SEMINARS

International and national collaborations with other facilities and research centres have been a continuous effort in 2016, with great results such as the first international associate partner of ALBA. Part of this collaboration has been translated in several seminars organized by the ALBA Synchrotron.

ONGOING COLLABORATIONS

Institute for Research in Fundamental Sciences (IPM)

The Institute for Research in Fundamental Sciences (IPM, Iran) is the first international associated partner of the ALBA Synchrotron.

During the construction of the Iranian Light Source Facility (ILSF), ALBA will host scientists from Iran to receive trainings and perform experiments with the aim of exchanging knowledge in the area of particle accelerators and synchrotron light applications.

OPEN SESAME

Project for transferring knowledge to the scientific community emerging around SESAME, the synchrotron facility which aims at promoting science for peace at the Middle East. The project includes training activities (courses, schools, etc.) and staff exchanges in a wide varied of synchrotron-based topics: accelerators, instrumentation, safety, beamlines, users, outreach, etc.

CLIC-CERN

The Compact Linear Collider (CLIC) study is an international collaboration working on a concept for a machine to collide electrons and positrons (antielectrons) head-on at energies up to several Teraelectronvolts (TeV). ALBA is involved in damping ring technologies, design and prototyping and test of the final equipment.

EuroCirCol

This H2020 project is a conceptual design study for a post-LHC research infrastructure based on an energy-frontier 100 TeV circular hadron collider. ALBA's role is to contribute in managing accelerator developments, organising international events and in the vacuum design.

Other collaborations

Also during 2016, ALBA has continued other collaborations established in previous years: Elettra Sincrotrone, CIEMAT- IFMIF, INFN - ELI-NP Romania, the Spanish Pulsed Lasers Centre, etc.

CONFERENCES AND SEMINARS

In 2016, ALBA has been involved in the organisation of 51 events (including two big congresses like IBIC and MEDSI, briefly detailed in the Outreach pages).

ALBA hosted 26 invited speakers from other synchrotron facilities and research centres. 14 workshops, conferences or congresses were organized in the area of accelerators, experiments, outreach or industrial applications. 7 internal events were addressed to the ALBA staff. Also, some events (4) were held outside ALBA facilities.

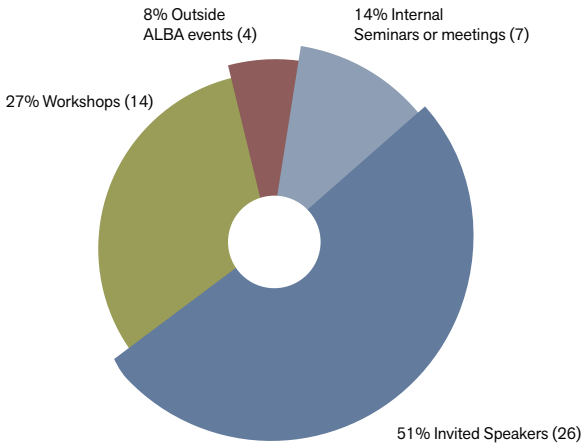

Group photo of HTCondor and ARC CE workshops, held in the ALBA Synchrotron from 29 February till 4 March 2016.

List of workshops, conferences or congresses organised or hosted by ALBA

29/02/16 – 04/03/2016	HTCondor / ARC CE Workshop
6/05/2016	Industrial workshop on cements, pigments, ceramics and glass
24-26/05/2016	5th Workshop on Power Converters for Particle Accelerators
30-31/05/2016	ICALEPCS ISAC Meeting
12-15/06/2016	Synchrotron Radiation to study Atomic Layer Deposition
18/06/2016	Conference on accelerators – ALBA Open Day
18/06/2016	Conference on cultural heritage with synchrotron light – ALBA Open Day
18/06/2016	Conference on biomedicine – ALBA Open Day
18/06/2016	Conference on accelerators – ALBA Open Day
11-15/09/2016	IBIC
11-16/09/2016	MEDSI
22-23/09/2016	Umbrella Meeting
7-9/11/2016	EuroCircol Collaboration Meeting
1/12/2016	FCRi Coffee with Research (Industry and science at the ALBA Synchrotron)

Group photo of the attendees at the 5th Workshop on Power Converters for Particle Accelerators (POCPA), held at the end of May 2016.

Check the complete list of events in http://www.albasynchrotron.es/en/media/events

STUDENTS AT ALBA

The ALBA Synchrotron has been developing and structuring its teaching and coaching activities to students, ranging from undergraduate or vocational training up to PhD students.

The Students' Program launched by the ALBA Synchrotron in 2015 has given the opportunity to develop their studies and getting in contact with a real work environment to more than 70 students so far. The internships can last up to 11 months and can be applied to different activities undertaken at ALBA, from Engineering, Experiments or Accelerators to Administration or Communication.

Undergraduate internships

A total of 15 university undergraduate students had the opportunity to do internships in ALBA during 2016. They were trained in different disciplines: accelerators' technologies, scientific applications of synchrotron light, health & safety, engineering, computing and control and science communication and outreach.

Vocational training

11 Students from eleven technical schools of the neighbouring area were trained in ALBA in 2016 sharing the time between the classroom and hands-on activities in the facility.

PhD students

Eight students have been performing their PhD at ALBA during 2016. Four of them are working inside the Experiments division in radiation damage in X-ray crystallography, molecular and structural biology of Auxine Response Factors, RF plasma sources for optical surface cleaning and graphene/nanosystem thin film deposition and surface properties of metal nanoparticles under reaction conditions in the NAPP endstation.

Three students in Accelerators, developing new diagnostics techniques using interferometry, performing beam dynamics studies with turn by turn data acquisition and developing a Solid State Amplifier for the 3rd Harmonic Cavity of the ALBA Storage Ring. One student in Engineering is analysing the beam induced vacuum effects in the cryogenic beam vacuum chamber of the Future Circular Collider (FCC).

Teaching activities

Members of the ALBA staff also carry out university teaching activities related to accelerators' physics and scientific applications of synchrotron light: Physics degree at the Universitat Autònoma de Barcelona (UAB), master on Nanoscience and Nanotechnology also from UAB and tutoring final grade projects at Universitat Politècnica de Catalunya (UPC).

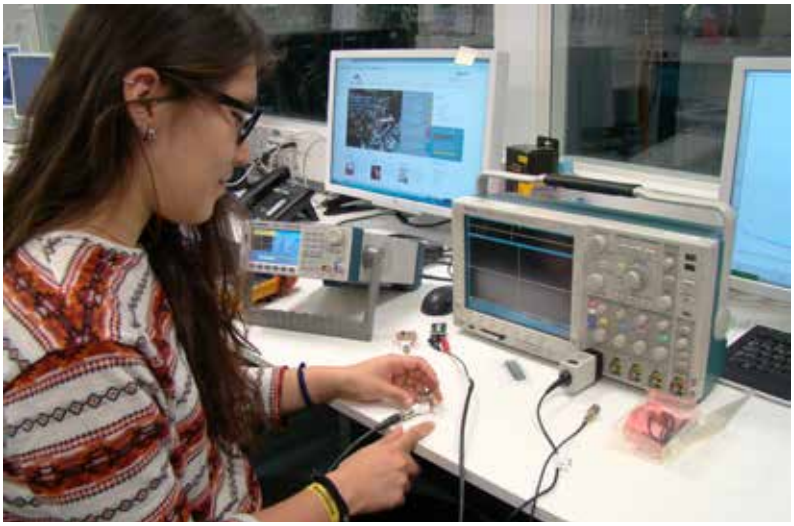

Meritxell Cabrejo Ponce, student of Physics Engineering, testing one of the circuits that she designed for the CIRCE beamline in 2016 as part of her internship.

OUTREACH

In 2016, the ALBA Synchrotron has continued developing a Communications and Outreach work plan in order to increase the visibility and knowledge about ALBA's activities among different target groups. Here, there are highlighted the most prominent activities carried out during the year.

Engaging the public for effective communications

The main event addressed to the general public, the ALBA Open Day, reached its maximum number of visitors in 2016, gathering 2,130 people in just one day. As in previous editions, scientists and attendees could share their passion for science and enjoy an activity where fun and learning were together. The participants were able to see the devices where the electrons pass through or those used for manipulating the synchrotron light, as well as to observe the interior of the accelerator's tunnel which was opened on that occasion and to attend demonstrations and conferences about concepts like vacuum or pressure, diffraction or spectroscopy and even enjoy the music show from the ALBA music band "The CatEyes" who covers popular songs for explaining what a synchrotron is.

During the whole year, the ALBA Synchrotron welcomed more than 5,000 visitors (half of them, students) that came to discover our facility, accelerators and main applications of our beamlines.

For people who do not have the possibility to come to visit us, the ALBA Synchrotron developed a series of five outreach videos, addressed to the general public, with the aim of explaining different types of experiments performed at ALBA. Environment, biomedicine, food, cultural heritage ... ALBA users explained how they took advantage of using synchrotron light and how beneficial for their research were the experiments performed in the facility. These videos are available in ALBA's YouTube channel.

Considering the scientific community, 2016 has been a special year as ALBA hosted two of the most renowned scientific congresses of the particle accelerators' field. From 11 to 16 September, the International Beam Instrumentation Conference (IBIC) and the Mechanical Engineering Design of Synchrotron Radiation Equipment (MEDSI) gathered more than 500 scientists and engineers from worldwide research facilities. The outstanding venue location of Barcelona as well as an efficient organization made both congresses a good experience for attendees to discover and share the latest ideas.

The ALBA Open Day 2016 was held on 18th June 2016. The event followed an itinerary composed by different areas of exhibition and demonstration, where visitors could stop at their will.

Snapshots from the video series developed in 2016 to explain the applications of synchrotron light in current societal challenges.

Group photos of MEDSI and IBIC delegates during the celebration of both congresses, hosted by ALBA, in Barcelona.

	2012	2013	2014	2015	2016
Scheduled hours for BLs	3112.0 h	3539.5 h	3740.0 h	4320.0 h	4368.0 h
Delivered hours for BLs	2387.3 h	2971.5 h	3621.2 h	4201.5 h	4261.0 h
Beam availability	76.7%	84.0%	96.8 %	97.3 %	97.6 %
Hours for machine development	1144.0 h	1368.0 h	1352.0 h	1408.0 h	1392.0 h
Mean time between failures	21.0 h	25.0 h	33.7 h	51.0 h	58.2 h
Mean time to be back	1.0 h	0.8 h	1.1 h	1.4 h	1.4 h

MACHINE PERFORMANCE

The ALBA storage ring has run more than 4300 h for users in 2016 with a beam availability of 97.6%. The storage ring runs on a 24 h a day, 7 days a week basis, for periods that usually are 4 to 5 weeks long. About 1400 h have been dedicated to the optimization of the accelerators for the users as well as to test new developments. Figure 52 shows the progression of the beam availability since the start of users operation.

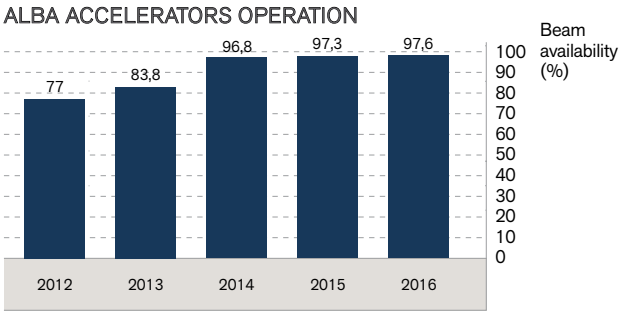

Figure 52: Progression of the beam availability since the start of users operation.

In 2016, the current in the storage ring has been increased from 130 mA up to 150 mA, following the RF upgrade program that started in 2015 and will be completed in 2018, when the nominal current of 250 mA is expected to be reached.

In January 2016 the mirror for the new IR beamline was commissioned with beam. The mirror, which has a slot through which the high energy radiation passes and only the IR light is reflected onto the beamline, needs a very precise alignment with respect to the photon beam to avoid any damage into it. The operation of the new infrared beamline has required an adjustment of the nominal electron orbit at the MIRAS location, while keeping the orbit unchanged at the rest of beamlines.

The ALBA storage ring with a circumference of 268.8 m has 448 buckets, where electrons can be injected in bunches. The different filling of the buckets will create different filling patterns. While

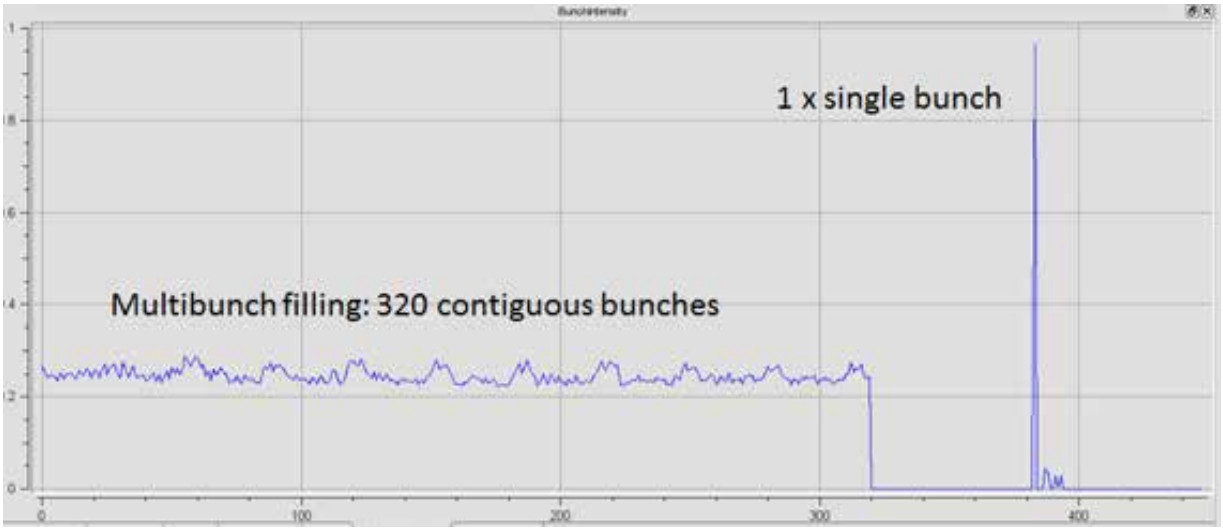

Figure 53: Filling Pattern in the Storage Ring showing 320 contiguous buckets filled and a single bunch in the gap.

the usual pattern is one in which 320 bunches are injected all with the same current, an algorithm has now been implemented, [1] which allows the storage ring to be filled with any filling pattern and to keep that filling pattern uniform during the run, as seen in Figure 53. This will make possible to offer different filling patterns for the users.

The Mean Time Between Failures of the RF system of ALBA has been increased by implementing a so called active RF trip compensation. In the ALBA Storage Ring there are 6 normal conducting cavities capable of providing up to 3.6 MV RF voltage. There is a redundancy or over-voltage that makes the RF system reliable enough to keep accelerating the stored beam even if one of the six cavities has an interlock and has stopped. When this interlock happens, some longitudinal and transversal oscillations are created in the beam orbit that last around 3 ms (damping time). Depending on the available RF voltage and stored current, these oscillations may cause a beam dump. In order to add more reliability to the accelerator operation, these oscillations were measured and characterized using the post-mortem analysis tools of the Low-Level RF System (LLRF). Then, a Feed-Forward algorithm was implemented in order to minimize the beam oscillations due to RF interlocks and to prevent beam losses [2].

REFERENCES

[1] R.Muñoz-Horta et al, Proceedings of the LINAC2016 Conference, East Lansing (USA), 2016

[2] A.Salom et al, Proceedings of the IPAC'2015 Conference, Richmond (USA), 2015

USERS

In 2016 the ALBA Synchrotron has included two allocations periods per year covering experiments to be performed the first and second semester. 2016-I call was launched from 30th June till 7th September 2015 and covered the period from January to June 2016 (with the exception of BL13-XALOC which covered the full year). 2016-II call was opened from 1st till 29th February 2016 and covered the period July to December 2016.

The number of proposals and shifts has slightly increased again this year. A total of 382 proposals were submitted (14% more than in 2015) and 5055 shifts were requested (2% more than in 2015). All the proposals for experiments are peer reviewed. They are evaluated by a panel, composed of international experts from different research areas. As a result of a ranking based on scientific excellence criteria, 216 proposals (16% more than in 2015) and 2325 shifts (8% more than in 2015) were awarded, representing an oversubscription factor larger than 2.

In 2016, according to the number of proposals and shifts requested, the most demanded beamline was BL24-CIRCE, the Photoemission Spectroscopy and Microscopy beamline. The largest number of granted proposals was for BL04-MSPD, the Materials Science and Powder Diffraction beamline. However, the largest number of awarded shifts was for BL29-BOREAS, the soft X-ray beamline for polarization-dependent spectroscopic research.

COMPARISON OF SUBMITTED AND GRANTED PROPOSALS AND SHIFTS

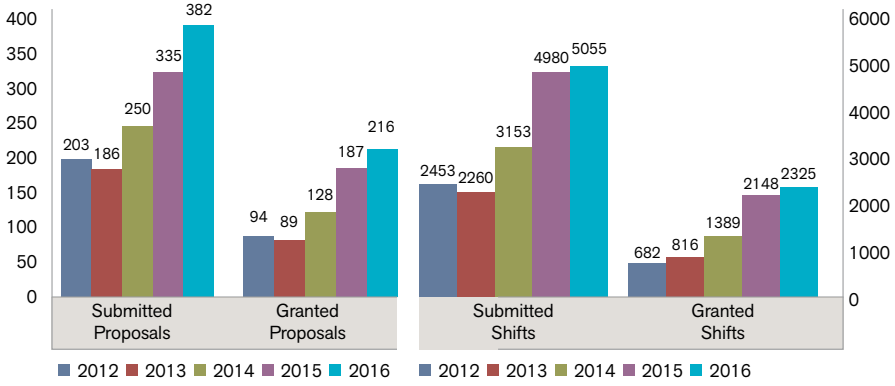

COUNTRY OF ORIGIN OF 2016 PROPOSALS

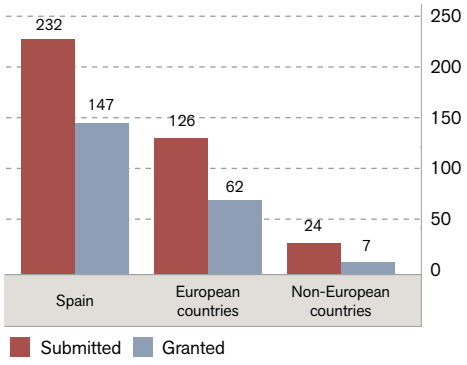

2016 CALL FOR PROPOSALS

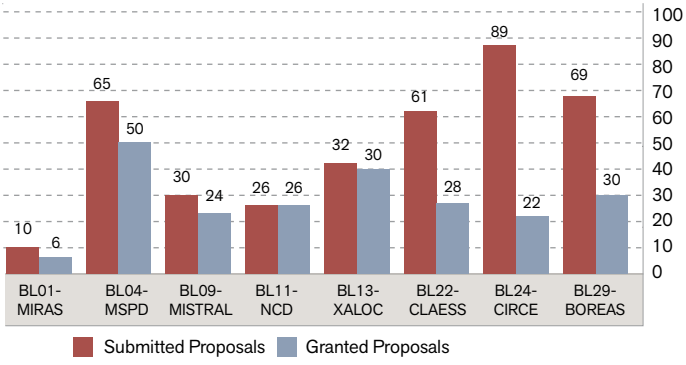

COUNTRY OF ORIGIN OF 2016 SHIFTS

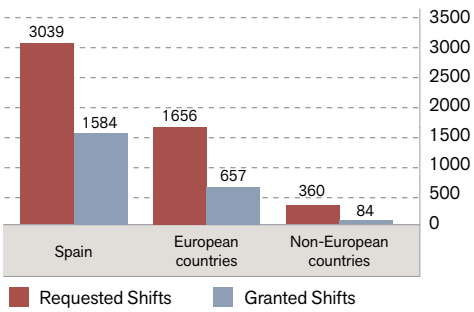

2016 SHIFTS

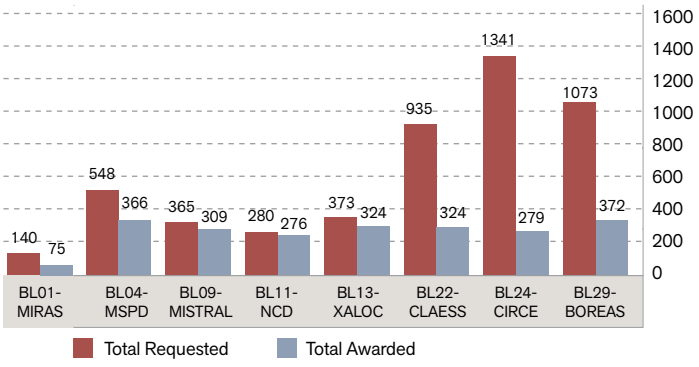

EVOLUTION OF INTERNATIONAL USERS %

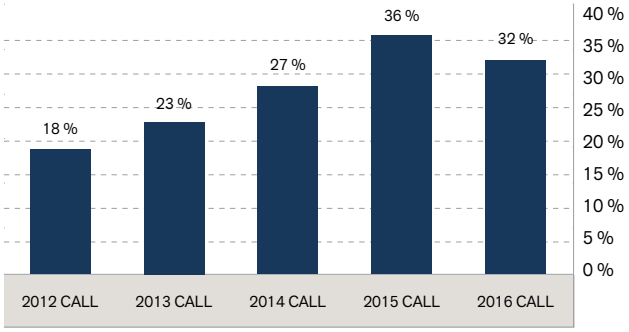

2016 RESEARCH AREAS OF ALL GRANTED SHIFTS

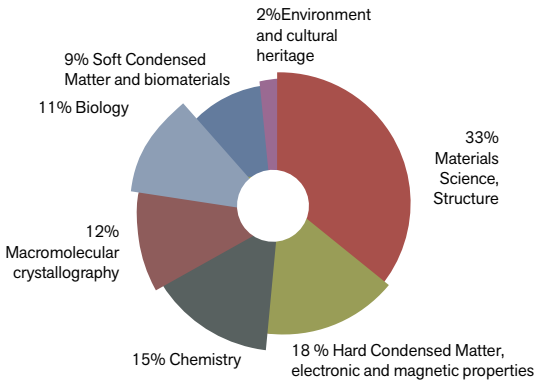

2016 SPANISH GRANTED SHIFTS BY REGION

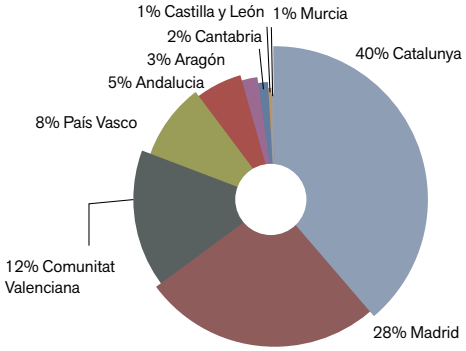

Most of the granted proposals correspond to Spanish institutions (68%). European institutions represent 29% and non-European countries 3%. The evolution of international users is stationary around 32%, instead of continuing its increasing tendency.

The Spanish granted proposals are distributed as follows: 40% Catalonia, 28% Madrid, 12% Comunitat Valenciana, 8%Basque Country, 5% Andalusia and other regions from Spain (7%).

Regarding the research areas of the granted shifts, experiments from Materials Science and Structure have been the most granted (33%), followed by Hard Condensed Matter and Electronic and Magnetic properties (18%), Chemistry (15%), Macromolecular Crystallography (12%), Biology (11%), Soft Condensed Matter and Biomaterials (9%) and Environment and Cultural Heritage (2%).

The number of visits (taking into account experimental visits, not single experiments) in 2016 has continued growing, achieving a total of 443 visits in a year.

EVOLUTION OF NUMBER OF VISITS / EXPERIMENTS

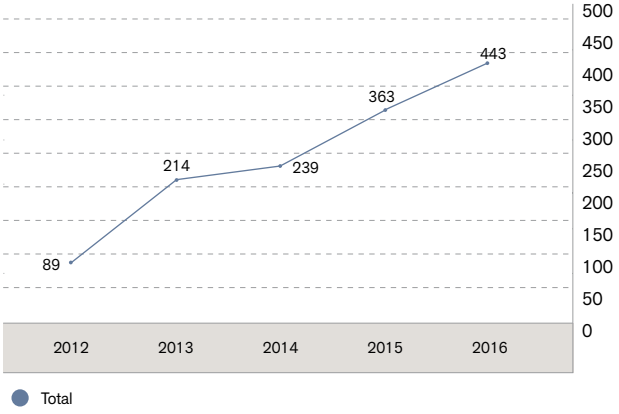

Accordingly, the number of registered home institutions and users in ALBA's database has also increased up to 2812 in 2016.

REGISTERED USERS

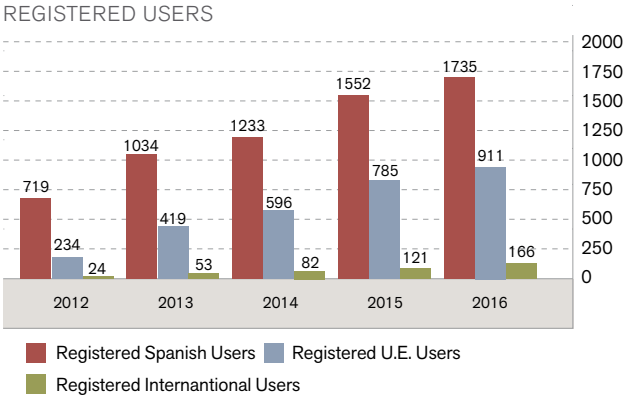

PUBLICATIONS

ALBA contributed to 219 publications in 2016. From these publications, 169 papers were published in peer-reviews journals. Some of the publications did not come from beamtime collected at ALBA. Therefore, a final statistics is provided concerning the publications from beamtime (including academic, industrial, in-house and friendly users research):148 (see figure next for its yearly evolution).

YEARLY EVOLUTION OF PUBLICATIONS

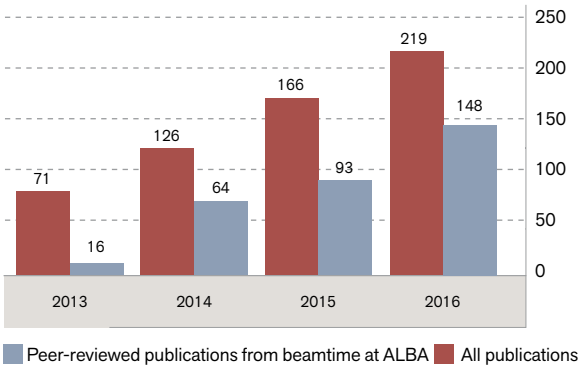

NUMBER OF PUBLICATIONS WITH HIGH IMPACT FACTOR (I.F. > 7.0)

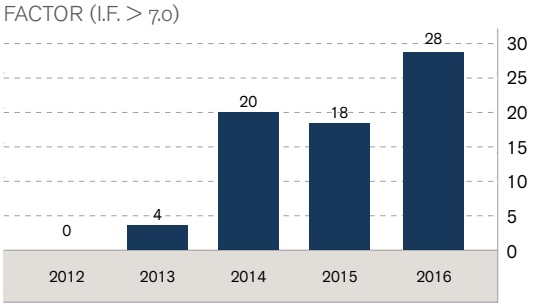

HUMAN RESOURCES

As of 31st December 2016, the staff of the ALBA Synchrotron is composed of 207 members, organized in five different divisions: Accelerators (16%), Administration (8%), Computing & Control (24%), Experiments (28%), and Engineering (17%). In addition, there is a Director's Office (7%), including the following offices: Health & Safety, Industrial, Projects and Knowledge Transfer Office and Communications and Outreach.

31% of ALBA staff are scientists, 30% technologists, 21% technicians, 15% administrative & management staff and 3% health and safety staff.

Although some minor improvements have been achieved in this area, still today gender distribution is not proportional in the ALBA Synchrotron. Women represent 26% of ALBA staff. As in previous years, areas like administration or the director's office have more women, while, in technical and scientific divisions, they are underrepresented.

Regarding the nationality of the staff, the international representation has slightly increased. 79% is Spanish, 18% are from European countries and 3% from foreign countries, with people from Asian, African and American countries.

ALBA STAFF - DISTRIBUTION OF DIVISIONS

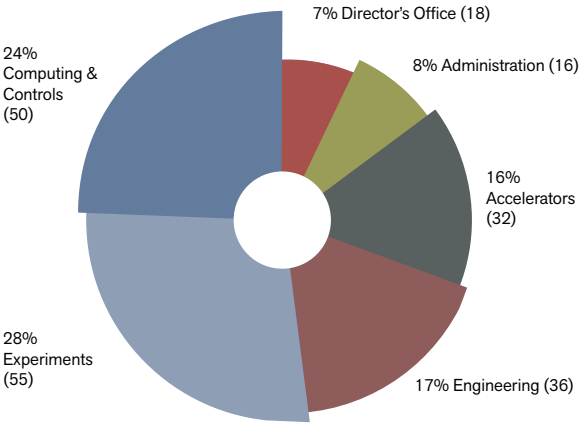

ALBA STAFF - DISTRIBUTION OF CATEGORIES

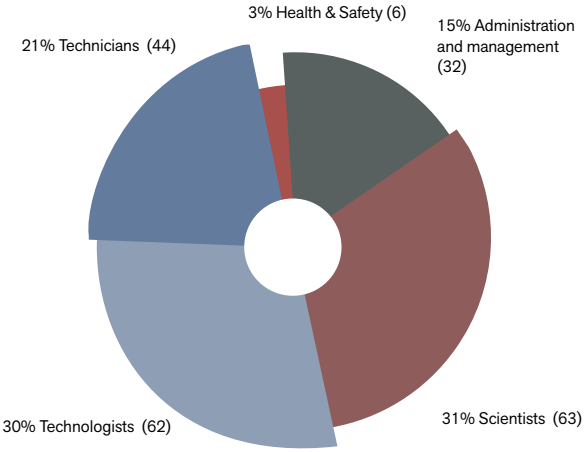

ALBA STAFF - DISTRIBUTION OF NATIONALITIES

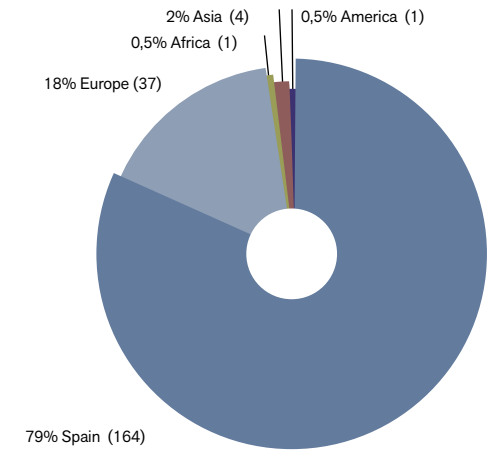

FINANCIAL INFORMATION

INCOME		
Capital funding	18,581,611 €	78.91%
Services revenue	315,678 €	1.34%
Agreements	380,577 €	1.62%
National grants	336,611 €	1.43%
European grants	66,452 €	0.28%
Other	3,866,689 €	16.42%
TOTAL	23,547,618 €	100.00%
EXPENDITURE		
Staff	8,109,718 €	38.70%
Social costs	2,164,503 €	10.33%
Equipment and maintenance	995,055 €	4.75%
Facilities	4,021,856 €	19.19%
Taxes	45,198 €	0.22%
Financial costs	68,127 €	0.33%
Users' support	462,037 €	2.20%
Students grants	24,517 €	0.12%
Expenses	255,208 €	1.22%
Other operational expenses	4,526,980 €	21.60%
Investments	283,874 €	1.35%
TOTAL	20,957,073 €	100.00%

New investments	2,590,545 €	100.00%

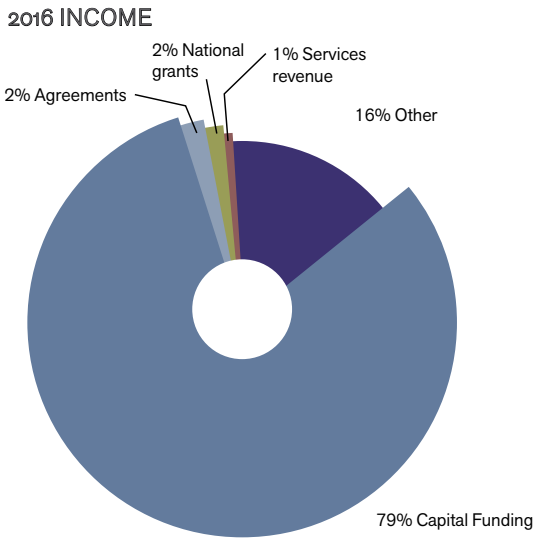

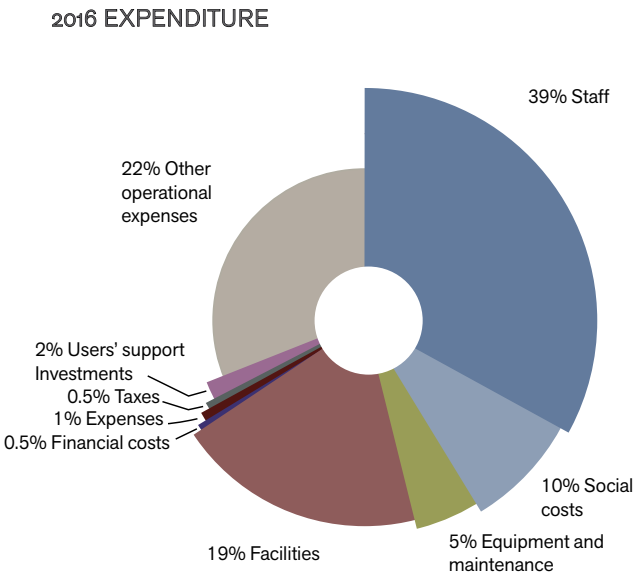

ALBA

Generalitat de Catalunya
Departament d'Empresa
i Coneixement

GOBIERNO DE ESPAÑA
MINISTERIO DE ECONOMÍA, INDUSTRIA Y COMPETITIVIDAD

ALBA Synchrotron - Carrer de la Llum 2-26
08290 Cerdanyola del Vallès, Barcelona, Spain - Tel: +34 93 592 43 00 - www.albasynchrotron.es